Technische Universität München

Max-Planck-Institut für Plasmaphysik

On the Origin, Properties, and Implications of Asymmetries in the Tungsten Impurity Density in Tokamak Plasmas

Tomáš Odstrčil

Vollständiger Abdruck der von der Fakultät für Physik der Technischen Universität München zur Erlangung der akademischen Grades eines

Doktors der Naturwissenschaften

genehmigten Dissertation.

Vorsitzender: Prof. Dr. Andreas Weiler

Prüfer der Dissertation:

1. Prof. Dr. Ulrich Stroth
2. Prof. Dr. Franz Pfeiffer

Die Dissertation wurde am 12.05.2017 bei der Technischen Universität München eingereicht und durch die Fakultät für Physik am 03.07.2017 angenommen.

DEPARTMENT OF PHYSICS
TECHNISCHE UNIVERSITÄT MÜNCHEN

On the Origin, Properties, and Implications of Asymmetries in the Tungsten Impurity Density in Tokamak Plasmas

Tomáš Odstrčil

DEPARTMENT OF PHYSICS
TECHNISCHE UNIVERSITÄT MÜNCHEN

On the Origin, Properties, and Implications of Asymmetries in the Tungsten Impurity Density in Tokamak Plasmas

Author:	Tomáš Odstrčil
Supervisor:	Univ.-Prof. Dr. U. Stroth
Advisors:	Priv.-Doz. Dr. T. Pütterich
Submission Date:	6 th April 2016

Abstract

In this thesis, the transport of tungsten ions is studied in the plasma of ASDEX Upgrade tokamak. The plasma facing components of the fusion reactors are expected to be built from high-Z materials such as W, Mo or Fe. These materials provide advantages like a high melting point, small erosion rates, and low tritium retention. However, due to the interaction of the plasma with the wall, ions of this material will be inevitably present also in the main plasma. These ions are not entirely stripped even at fusion plasma temperatures, and therefore emit strong line radiation, which can significantly degrade the performance of the fusion plasma. Thus the understanding and control of impurity transport are of critical importance to the success of fusion.

The high mass and charge of the heavy impurities make them susceptible to some of the forces acting upon the plasma, resulting in a poloidal variation of their density. The most prominent are the centrifugal force arising from the plasma rotation and the electric force caused by magnetically trapped non-thermal ions. Furthermore, the poloidal asymmetries should have a significant impact on the radial transport of heavy ions, which was widely ignored up to date.

In the present work, the poloidal asymmetries in the heavy impurity density were inferred from the soft X-ray radiation using a newly developed tomographic method. The high accuracy of the tomography and of the model for the centrifugal force allowed to identify for the first time in an experiment the effect of the fast ion distribution produced by neutral beam injection on the poloidal asymmetry of the tungsten density. The measured asymmetry was compared to several fast ion models, and the best match was found with the Monte Carlo code in the TRANSP code suite that includes finite orbits effects of the fast ions.

Similarly, fast ions accelerated by ion cyclotron heating and localized mainly in the outboard side of the plasma due to a magnetic trapping and produce a poloidal electric field pushing the high-Z impurities towards the inboard side. The structure of the poloidal asymmetry reveals details of the fast ion distribution function, which can hardly be accessed by other diagnostics. Along these lines, the asymmetries provide a stringent test of models for ion cyclotron heating. The analysis of a database of discharges with emphasis to density variation and was compared with the results of TORIC-FFPMOD code. The comparism revealed that for moderate densities the modeled asymmetries exceed the measured ones by roughly a factor of two. This discrepancy is not understood and should be investigated further. Additionally, a new application of the poloidal asymmetries was demonstrated investigating the fast particle transport by sawtooth crashes.

For the first time, the effect of the poloidal asymmetries on the magnitude of the diffusive and convective radial transport was experimentally demonstrated. The variation in the poloidal asymmetry produced by switching between two neutral beam sources, from tangential to more radial injection geometry, reduced the tungsten diffusion coefficient from about 0.2 to $0.04\,\mathrm{m}^2/\mathrm{s}$. At the same time, the ratio of convective and diffusive transport stayed nearly unchanged. Both observations are in agreement with neoclassical theory.

The improved understanding of the poloidal asymmetries will have a direct impact on the strategies to avoid tungsten accumulation in tokamak plasmas. The gained knowledge is valuable for influencing the impurity transport in other, present or future devices.

Zusammenfassung

Diese Arbeit befasst sich mit dem Transport von Wolframionen im Tokamak ASDEX Upgrade, der sich am Max-Planck-Institut für Plasmaphysik in Garching befindet. Es is zu erwarten, dass die erste Wand von zukünftigen Fusionsreaktoren aus einem hoch-Z Material, wie W, Mo, Fe besteht. Diese Materialien bieten mehrere Vorteile, wie zum Beispiel einen hohen Schmelzpunkt, einen niedrige Erosionsausbeute und ein geringes Rückhaltevermögen von Tritium. Aufgrund von Wechselwirkungen zwischen Plasma und Wand ist es jedoch unvermeidlich das Atome dieser Materialien auch in das Plasma gelangen. Da Ionen dieser Elemente auch bei fusionsrelevanten Temperaturen nicht vollständig ionisiert werden, emittieren sie starke Linienstrahlung. Diese kann das Plasma abkühlen und dadurch die Wirtschaftlichkeit eines Reaktors reduzieren. Daher sind das Verständnis und die Kontrolle des Verunreinigungstransports für den Erfolg der Fusion als Energiequelle von entscheidender Bedeutung.

Die hohe Masse und Ladung der schweren Ionen resultieren in Kräften die zu einer poloidalen Variation ihrer Dichte führt. Die Bekannteste dieser Kräfte ist die Zentrifugalkraft, welche von der toroidalen Plasmarotation erzeugt wird . Außerdem kommt es auch zu Störungen im elektrostatischen Potential, die durch im Magnetfeld gefangene, nicht-thermische (schnelle) Ionen erzeugt werden. Des Weiteren, sollten poloidale Asymmetrien einen signifikanten Einfluss auf den radialen Transport der schweren Ionen haben, was in der Vergangenheit weitgehend ignoriert wurde.

In dieser Arbeit, werden die poloidalen Asymmetrien in der Verunreinigungsdichte aus der weichen Röntgenstrahlung (SXR) mit Hilfe eines neu-entwickelten tomographischen Rekonstruktionsprogramms abgeleitet. Die hohe Genauigkeit der Tomographie und ein detailliertes Modell für die Zentrifugalkraft ermöglichen es, zum ersten Mal, den Einfluss von schnellen Ionen, die durch Neutralteilcheninjektion (NBI) erzeugt werden, auf die poloidale Asymmetrie von Wolfram zu identifizieren. Die gemessene Asymmetrie wurde mit mehreren Modellen für schnelle Ionen verglichen. Die beste Übereinstimmung liefert der Monte Carlo Code aus dem TRANSP Code Paket, der am genauesten die Trajektorien der schnellen Ionen berücksichtigt.

Ähnlich erzeugen magnetisch gefangene schnelle Ionen, die durch Ionen-zyklotronheizung beschleunigt werden und sich vorwiegend auf der Außerseite des Torus befinden, ein poloidal variierendes elektrostatisches Potential, das die schweren Verunreinigungen auf die Innenseite des Torus drückt. Daher kann die Struktur der Asymmetrien Aufschlüsse über die Verteilungsfunktion der schnellen Ionen liefern, die für keine andere Messtechnik zugänglich sind. Darüber hinaus ermöglichen die Asymmetrien einen Test der Modelle für die Ionen-zyklotron-heizung. Eine Analyse einer Datenbank von Entladungen, mit Schwerpunkt auf Variation der Elektronendichte, zeigte, dass bei mittlerer Dichte die von dem Code TORIC modellierte Asymmetrie die gemessene um den Faktor zwei übersteigt. Für diese Diskrepanz konnte keine Erklärung gefunden werden weswegen sie weiter untersucht werden sollte. Zusätzlich und als neue Anwendung wird gezeigt, dass die poloidalen Asymmetrien für die Untersuchung des Transports von schnellen Teilchen durch Sägezahninstabilitäten verwendet werden können.

Zuletzt wurde zum ersten Mal die direkte Auswirkung der poloidalen Asymmetrien auf die Größe des radialen Transports experimentell nachgewiesen. Die Veränderung der poloidalen Asymmetrie, die durch das Wechseln zwischen zwei, nah nebeneinander gelegenen NBI Strahlen, erzeugt wurde, führte zu einer Vergrößerung des Diffusionskoeffizienten für Wolfram von etwa $0.04\,\mathrm{m}^2/\mathrm{s}$ auf $0.2\,\mathrm{m}^2/\mathrm{s}$, was in Übereinstimmung mit der Transportvorhersage durch die neoklassische Theorie ist. Das verbesserte Verständnis der poloidalen Asymmetrien wird einen direkten Einfluss auf die Strategien haben, die verwendet werden, um die Konzentration von Wolfram in den Plasmen von ASDEX Upgrade zu kontrollieren. Die Ergebnisse dieser Arbeit sind zeudem wertvoll um den Verunreinigungstransport in heutigen und zukünftigen Fusionsmaschinen zu beeinflussen.

Contents

1. Introduction

1.1. Challenge of World Energy Supply

Currently, one of the largest challenges for mankind is how to provide a secure and sustainable energy supply despite growing energy demands and shrinking of the fossil fuel reserves. The increase in consumption of energy has two main causes. First of all, the world population is growing almost exponentially; the human population has reached 7 billion in 2012, and social models predict that it could reach 9 billion in 2050 [1]. The second, even more important reason for the rapid grow of the energy consumption, is increasing prosperity of the developing countries like India and China which have now about one billion inhabitants each. Mere consumption of primary energy in China is expected to grow by 50% in the next 20 years [2]. Potential and a will for energy saving in the developed countries is limited and cannot significantly reduce this trend in the global energy needs.

Since we cannot rely on the discovery of entirely new energy sources in the next decades, our effort needs to focus on the sources available now or in the near future. Today, most of the energy is produced from fossil fuels like coal, gas, and oil. However, these resources are scarce and not equally geologically distributed. Most of the oil reserves are situated in the countries with unpredictable political systems. Additionally, burning fossil fuels causes significant air pollution and the release of sulfur and nitrogen oxides participating in the production of acid rain. Finally, it is believed that CO_2 produced by the burning of fossil fuels could be responsible for changes in the climate observed in the last decades. The consequent temperature increase caused by the so-called greenhouse effect can have negative impact on the life of the human population.

Currently, only two other options seem feasible; the renewable power sources and nuclear power. The renewable sources, like wind, water, solar and geothermal power plants are virtually unlimited sources of energy. However, due to the high costs, low power density and restrictions given by geographical opportunities these sources are not suitable for energy production on the massive scale necessary for the replacement of the fossil fuels. Additionally, fluctuations caused by weather, the day cycle and the seasons put enormous demands on backup power sources and storage capacities, which must be able to respond within minutes and replace a substantial fraction of the installed power to maintain stability of the national power grids. Despite this caveat, these sources provide a considerable potential, and they will play an irreplaceable role in the future energy production.

The second option is nuclear power. Most of the present day fission power plants are still using $^{235}_{92}\mathrm{U}$ as fuel. However, the world reserves of this element are limited. When the fossil fuels were completely replaced by fission, the uranium reserves would be exhausted by the end of this century [3]. Further extension of this energy source is possible only by the development of fast breeder reactors which use more common $^{238}_{92}\mathrm{U}$ and $^{232}_{90}\mathrm{Th}$ as fuel. Additionally, development and building of new fission reactors have been interrupted due to the negative public opinion influenced by serious nuclear accidents in Chernobyl, Three Mile Island and also recently at Fukushima. A restart of this research topic currently does not have the necessary support among people and politicians.

However, nuclear power can also be produced by fusion power plants. Compared to the other options, it is the most technically challenging solution and commercial fusion power-plants will be hopefully available at large scale before the end of this century. The key advantage of fusion plants will be safety, almost unlimited sources of fuel and emission-free production of energy. The principle of fusion reactors makes an uncontrolled chain reaction impossible, in contrast to the fission power plants. Any instability leads to the immediate interruption of the fusion reaction. Moreover, raw material for the fuel production, deuterium and lithium are equally distributed over the world. Their supplies are sufficient for millions of years of energy production, given today's consumption.

1.2. Nuclear Fusion

The main idea of nuclear fusion is merging two lighter nuclei into a heavier one. Due to a change in the binding energy the difference may be released as kinetic energy or radiation. The binding energy of the nucleus exhibits a maximum for iron, which represents the most stable configuration of neutrons and protons. Any lighter element could be theoretically used for energy production by fusion, but most of them are unusable for commercial power plants. An overview of the most promising fusion reactions with their cross-section is shown in Fig. 1.1. Obviously, a reaction between deuterium (D) and tritium (T) nuclei protrude, because for the DT reaction the highest reactivity and cross section are reached at the lowest temperature. Since obtaining the optimal conditions for this reaction is already very difficult, application of the other fusion reactions is not expected in the near future.

Merging of the deuterium and tritium nuclei produces one helium nucleus, a neutron

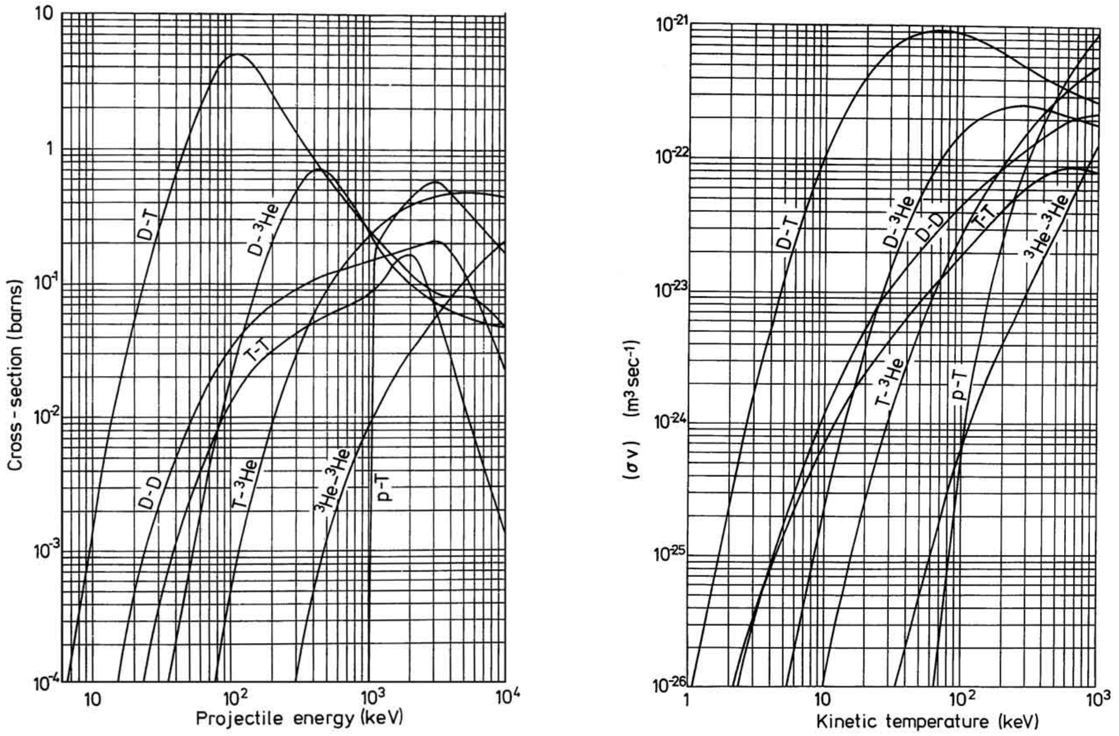

Figure 1.1.: (left) The cross-section for a basic fusion reactions measured in barms ($10^{-28}\mathrm{m}^2$) as the function of the injected particle energy. (right) A reactivity $\langle \sigma v \rangle$ averaged over the Maxwellian distribution. The figure was adapted from [4].

and releases a significant amount of energy

$$\mathrm{D} + \mathrm{T} \rightarrow \, {}^{4}_{2}\mathrm{He}\,(3.5\,\mathrm{MeV}) + \mathrm{n}\,(14.1\,\mathrm{MeV}). \tag{1.1}$$

One fifth of the released energy $E_f = 17.6\,\mathrm{MeV}$ is carried by an alpha particle, while the neutron has the rest. The produced He nuclei, commonly called ash, transfers their energy via Coulomb collisions to the surrounding particles and heat the plasma, while the fast neutrons escape the plasma without any interaction. Outside of the plasma are neutrons stopped in the absorbers and heat the material, enabling the energy production. The neutrons play also an essential role in tritium production. Tritium is a very rare hydrogen isotope with a half-life of 12.32 year, and the global inventory of this element (roughly 10 kg) have been produced artificially in the fission power plants. Therefore, we have to use the fast fusion neutrons for tritium breeding reaction. First of all, a beryllium multiplier is applied to increase the number of neutrons; then the fast neutrons are slowed down in a lithium target to thermal speed, and finally the following reaction takes place

$$\mathrm{n} + {}^{7}_{3}\mathrm{Li} \rightarrow \ \mathrm{T} + {}^{4}_{2}\mathrm{He} + \mathrm{n} - 2.47\,\mathrm{MeV}. \tag{1.2}$$

Therefore, tritium breeding provides a sustainable source of fuel for future power plants. Nevertheless, the main challenge remains; how to maintain the high plasma temperatures at low external heating power in order to reach stable burning conditions.

1.3. Magnetic Confinement Fusion

Different methods of plasma confinement at densities and temperatures necessary for fusion have been investigated for over a century. Two fundamentally different approaches have been developed: the *inertial confinement fusion* (ICF) based on fast compression of the fuel pellet by an extremely intense laser pulse and *magnetic confinement fusion* (MCF), where plasma particles are confined in magnetic traps. The most advanced method for the development of the power plant is magnetic confinement in a tokamak. Tokamaks are axially symmetric toroidal devices, as illustrated in Fig. 1.2, originally invented by a group of Soviet scientists led by Lev Artsimovich. The Lorentz force acting on plasma particles results in their gyro-motion around magnetic field lines and a free motion along them. However, the curvature of the magnetic field lines creates gradients in the magnetic field intensity. The gyroradius of a particle with charge q and mass m is then periodically changing, causing a drift perpendicular to the magnetic field described by

$$\mathbf{v}_D = \frac{\frac{1}{2}mv_\perp^2 + mv_{||}^2}{qB^3}(\mathbf{B} \times \nabla\mathbf{B}), \tag{1.3}$$

where $v_\perp$ and $v_{||}$ is the particle velocity perpendicular and parallel to the magnetic field $\mathbf{B}$. Since the drift direction is charge dependent, the particle movement would lead to a charge separation of ions and electrons. The separated charges produce a vertical electric field and an outward particle flow. However, when a toroidal current is induced in the plasma, the superposition of the poloidal B_p and toroidal B_t component of the tokamak's magnetic field will result in a helical structure wrapping around the torus (see Fig. 1.2). In such a magnetic configuration, the particle gyro-centers will drift radially inward and outward on their orbits, canceling the net radial drift.

The poloidal magnetic flux, pressure and current in the tokamak are coupled via the Grad-Shafranov equation [5], derived from the equilibrium equation in ideal magnetohydrodynamics (MHD) under the assumption of toroidal symmetry. From the Grad-Shafranov equation follows that, the pressure is constant on the surfaces of the equal poloidal flux (flux-surface). Also other parameters like the bulk ions density and temperature are assumed to by constant on each flux-surface due to high parallel transport along the magnetic field lines. Therefore, these parameters are often represented by one-dimensional profiles, labeled by a normalized flux coordinate

$$\rho_\Psi = \sqrt{\frac{\Psi - \Psi_{axis}}{\Psi_{LCFS} - \Psi_{axis}}}. \tag{1.4}$$

This coordinate is defined such that $\rho = 0$ corresponds to the magnetic axis and $\rho = 1$ is at the last closed flux surface (LCFS), also called separatrix. The flux Ψ corresponds to the poloidal or the toroidal flux, but alternatively also the plasma volume enclosed by the given surface is often used (for instance Eq. (5.5)). The distance of the magnetic axis from the axis of the torus is called major radius R_0 and the radius of the plasma column is called minor radius a.

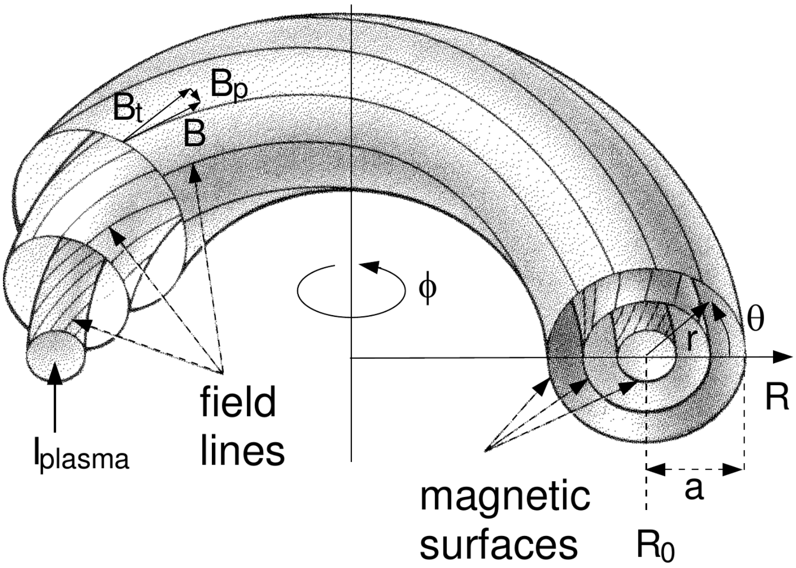

Figure 1.2.: Geometry of the magnetic field lines and nested magnetic flux surfaces in the toroidally symetric tokamak plasma.

1.4. Role of Impurities in Fusion

Impurities, i.e. ions different from the fuel ions, are inevitably present in the plasma because of interaction with the surrounding vessel wall. In order to control and reduce plasma wall interaction (PWI), several strategies have been developed. One of the outcomes was a divertor concept [6], that was first investigated in the former ASDEX tokamak. The divertor configuration is separating the main plasma from the wall by introducing an auxiliary toroidal coil, usually installed bellow the chamber, with the current flowing in the same direction as the main plasma current. Superposition of the poloidal magnetic field from the plasma and the divertor coils produce a so-called X-point, i.e. the point where the poloidal magnetic field components is zero. This magnetic configuration is significantly increasing the length along the magnetic field lines, which the wall impurity particles must pass, before they reach the confinement region and thus the impurity influx is efficiently reduced.

The impurities are affecting the fusion performance in two ways. First of all, the presence of the impurities dilutes the fuel reducing the probability of D and T collisions. Moreover, the impurities increase the radiative cooling of the plasma. While the former is the issue mainly for the light impurities, the radiative cooling is important for heavy ions with charges $Z \gtrsim 40$, which do not have fully striped electron shells even at fusion temperatures. The impact of the impurities can be illustrated by a simple example. We will define the fusion gain factor as

$$Q = \frac{P_{\mathrm{fus}}}{P_{\mathrm{aux}}} \tag{1.5}$$

with P_{fus} denoting the power released by the fusion reaction and P_{aux} the power from the externally applied auxiliary heating sources. The highest value of Q reached experimentally in present devices was 0.6 during a D-T campaign at the Joint European Torus (JET) [7]. The value of Q expected for the prototype of the fusion reactor called International Thermonuclear Experimental Reactor (ITER) [8] is about 10.

We can consider radiative cooling as as "negative electron heating". In order to obtain the same plasma state as without cooling it must be compensated by additional auxiliary heating. Using the definition of the fusion gain factor Q, and including also fuel dilution by the impurities, an explicit dependence on the impurity concentration can be expressed by

$$Q = \frac{P_{\mathrm{fus}}}{P_{\mathrm{aux}}} = \frac{(1 - \sum_{(z>1)} Z_z f_z)^2}{Q_0^{-1} + 4(\langle \sigma v \rangle E_f)^{-1} \sum_z f_z L_z}, \tag{1.6}$$

with Q_0 denoting the fusion gain without impurities, f_z is a concentration of impurity z with charge Z_z and radiative cooling coefficient L_z in units of Wm^3. The reduction of the fusion gain for He, C and W is illustrated in Fig. 1.3. The helium ash concentration reduce the fusion gain to halve for $f_{\mathrm{He}} > 0.1$, carbon for $f_{\mathrm{C}} > 0.03$ and tungsten already for $f_{\mathrm{W}} > 10^{-4}$. Helium and carbon affect mostly via dilution and W mostly due to impurity radiation. Carbon ions are fully ionized at temperatures above 0.1 keV and therefore radiates mainly bremsstrahlung, however the tungsten ions are only partially ionized at fusion temperature (about 10–30 keV) and emit intense line radiation. The difference of two orders of magnitude in the acceptance level between these two types of impurities illustrates, how important it is to understand the transport mechanisms of high-Z impurities, which potentially lead to an accumulation of impurities in the core of the plasma.

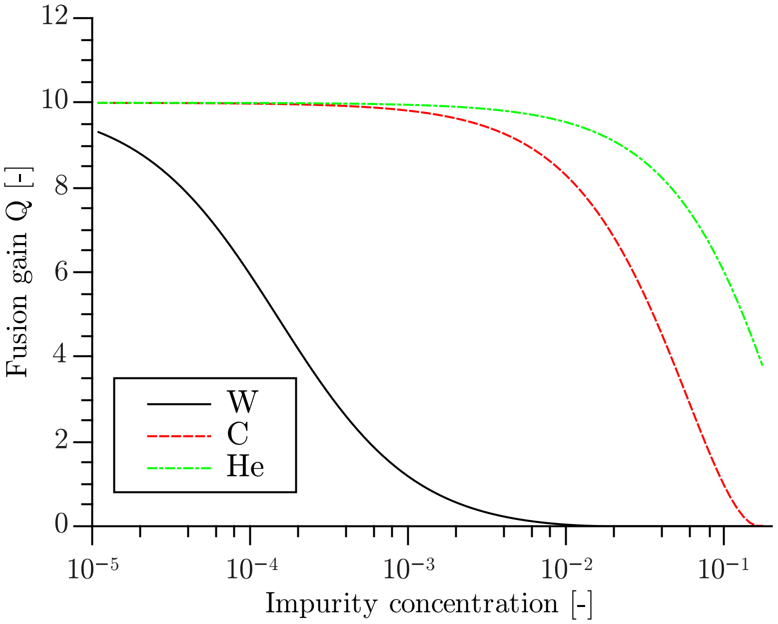

Figure 1.3.: Impact of the impurity concentration on the fusion gain, assuming $Q_0 = 10$ and $T_e = 14\,\text{keV}$.

At the same time, the impurities are essential for the tokamak operation. In the current machines, most of the power from the plasma is conducted to the divertor. However, this power exhaust method would lead to unacceptably high power loads on the material and melting of the divertor heat shield in a reactor. Therefore, a substantial fraction of the power has to be radiated from the edge of the plasma, without deterioration of the core fusion gain. In the optimal case, the profile of the fuel density should be peaked in the plasma core, while the radiation profile should be hollow. As it will be shown in the rest of this thesis, this is difficult to achieve, and a proper impurity control is one of the remaining challenges for fusion reactors.

1.5. Outline of the Thesis

Chapter 2 provides brief description of the ASDEX[1] Upgrade tokamak and the diagnostics required for the analysis of tungsten transport experiments. Chapter 3 describes a diagnostics used to infer the tungsten density in ASDEX Upgrade. Most of the attention is dedicated to the soft-X ray diagnostic, which provids key information about the two-dimensional distribution of tungsten required for this research. Nevertheless, the other diagnostics are still necessary to obtain complete knowledge on the tungsten density dynamics in the whole plasma volume. In the framework of this thesis, a new tomographic inversion code was developed. The method for the high-quality inversions of the line-integrated tungsten emissivity measurements and the detection of the poloidal asymmetries is described in Chapter 4. In Chapter 5, the current status of the impurity transport theory is reviewed. The existing theory is summarized, and the most important consequences for neoclassical and turbulent transport are highlighted. Chapter 6 presents the experimental results focusing on the poloidal asymmetries driven by neutral beams, i.e. the centrifugal asymmetry and the effects of fast particles. Chapter 7 investigates the effect of the poloidal electric field on the tungsten ions. Further, the possibility of the fast particle studies based on the poloidal asymmetries in the impurity density was explored. An example of an in-out asymmetry was analyzed in Chapter 8, demonstrating for the first time a clear impact of these poloidal asymmetries on the core radial transport consistent with the extended neoclassical theory. In the Appendix A is included the details of the developed tomographic inversion algorithm.

---

[1] Axial Symmetric Divertor EXperiment

2. The ASDEX Upgrade tokamak

2.1. Overview

ASDEX Upgrade (AUG) is a medium-sized divertor tokamak (Fig. 2.1), operated since 1991 at the Max-Planck Institute für Plasmaphysik (IPP), Garching, Germany. The major radius of the torus is 1.65 m and the minor radius is 0.5 m, which is about half the size of JET in Culham, UK and a quarter of the size of the ITER tokamak in Cadarache, France. ASDEX Upgrade is particularly suitable for ITER relevant studies due to a similar geometry of the plasma chamber and the divertor configuration. Additionally, due to the availability of large amounts of auxiliary heating power, reactor relevant values for the heat flux across the separatrix occur. AUG is typically operated with a plasma current between 0.6 and 1.2 MA, a toroidal magnetic field of 1.8–3 T and discharge length of about 10 s. The toroidal magnetic field is generated by 16 large copper coils wrapped around the torus and the horizontal coils for shaping and positioning of the plasma are located outside of the toroidal coils.

Figure 2.1.: The chamber of the ASDEX Upgrade tokamak during installation of the tungsten plasma facing components (source: IPP webpage)

One of the unique properties of AUG are the tungsten covered plasma facing components (PFC). Originally, the first wall was built entirely from carbon composite tiles. The tungsten research program started in 1996 by covering of the divertor strike-points by a thin layer of W [9]. Later, the fraction of the covered surface was incrementally increased, reaching up to a full W coverage in 2007 [10]. Now, ASDEX Upgrade represents the only full tungsten fusion device in the world. The divertor tiles, which have to withstand the highest heat fluxes are covered by 200 μm thick tungsten layer that was deposited by a vacuum plasma spray (VPS) coating, while the main chamber was treated by physical vapor deposition (PVD) coatings with various thicknesses up to 4 μm. The only exceptions are the outer divertor, which is composed of the solid tungsten monoblocks since 2014 and one row of inboard tiles, which are made from a ferromagnetic steel. In parallel, experiments aimed at the development of procedures, which reduce the W density in the plasma core were conducted. An acceptable plasma performance and clean plasmas have been demonstrated in the full tungsten AUG, which has justified the decision that ITER will use tungsten as the divertor material. In 2009 an upgrade of the JET tokamak had started and the “ITER-Like Wall” with a tungsten divertor and beryllium tiles covering the chamber walls was installed. Further, the WEST project (Wolfram Environment in Steady-state Tokamak) was initialized in 2013, where the tungsten properties during long term heat load in the tokamak environment will be studied.

2.2. Auxiliary Heating Systems at AUG

AUG is equipped with several auxiliary heating systems providing extra heating in addition to the intrinsic ohmic heating by the plasma current. The neutral beam injection (NBI) is the most commonly used heating system at AUG and provides up to 20 MW of power. Additionally, the plasma can be heated by ion and electron cyclotron heating (ICRH and ECRH) providing up to 5 MW and 4 MW respectively. In the experiment, at most 24 MW of the total heating power have been demonstrated, which established a world record regarding the power over the major radius $P_{\mathrm{sep}}/R = 10\,\mathrm{MW/m}$ and this is the closest achieved value to the $P_{\mathrm{sep}}/R = 15$ foreseen for ITER [11].

2.2.1. Neutral Beam Injection

The NBI system consists of two beam boxes localized in the sectors 15 and 7 (see Fig. 2.2a). Both beam boxes are equipped with four independent sources each delivering up to 2.5 MW of heating power. The sources of the box in section 15 are labeled

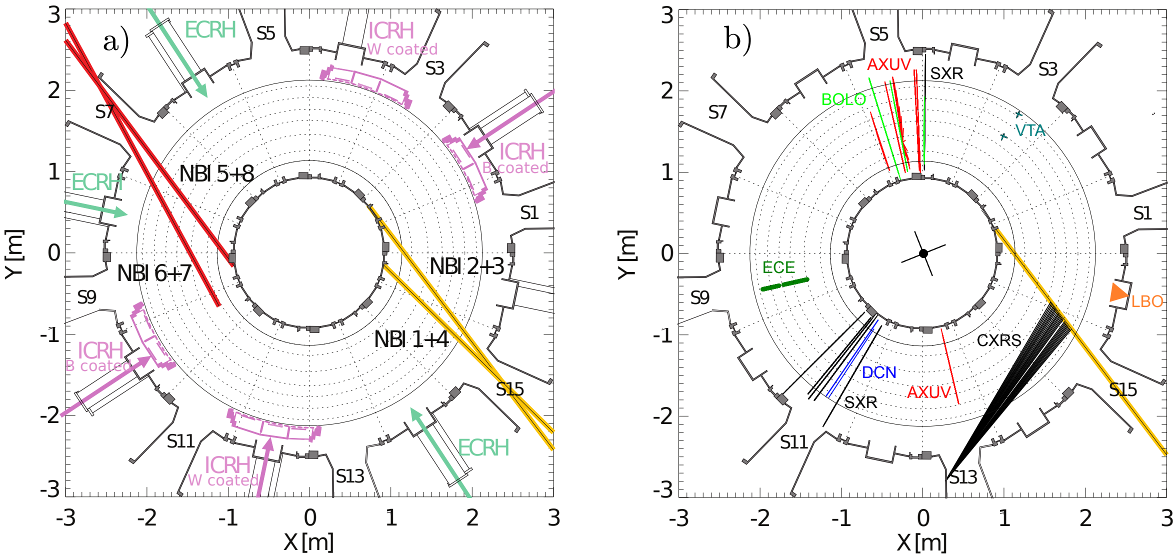

Figure 2.2.: a) The figure depict an overview of the heating sources available in the ASDEX Upgrade tokamak. The tokamak is equipped with eight neutral beam sources NBI 1-8, eight gyrotrons and four ion cyclotron heating antennas. b) most important diagnostics for this study are shown in the right figure. The soft-X-ray diagnostics (SXR), foil bolometers (BOLO) and diode bolometers (AXUV) provide spatially resolved, line integrated measurements of the plasma emissivity. Vertical Thompson scattering (VTA) and ECE heterodyne radiometer (ECE) deliver information about the local value of the electron temperature, while the electron density is obtained by the VTA and the DCN interferometers. The charge exchange spectroscopy (CXRS) enables to measure the ion temperature and plasma rotation.

Q1–Q4 and are equipped with an arc ionization source and a maximal acceleration voltage of 60 kV. Sources Q3 and Q4 are aligned close to the magnetic axis, while Q1 and Q4 are pointing slightly off-axis. The sources of the beam box in sector 7 are labeled Q5–Q8 and are equipped with a radio frequency ionization source and a maximal acceleration voltage of 93 kV. The sources Q6–Q7 are significantly off-axis, with a favorable configuration for the neutral beam current drive. Source Q3 plays an important role, because it serves as a diagnostic beam for the charge exchange spectroscopy system, necessary for a measurement of the plasma rotation and ion temperature.

2.2.2. Electron Cyclotron Resonance Heating

The electron cyclotron resonance heating (ECRH) system installed at AUG consists of eight gyrotrons providing up to 5 MW of power. Since the microwave radiation has a quasi-optical behavior, metal mirrors and waveguides are employed to transmit the emission into the torus. The heating position can be varied via the movement of metal mirrors in the tokamak, deflecting the beam at the desired angle. The poloidal steering of the mirrors can be accomplished swiftly within $\sim 50\,\mathrm{ms}$, while the toroidal movement is slower ($\sim\mathrm{s}$). The gyrotrons frequency is tunable in frequencies, i.e. 105 GHz ($\lambda = 3\,\mathrm{mm}$) and 140 GHz ($\lambda = 2\,\mathrm{mm}$), which corresponds to central second harmonic heating for 1.87 T and 2.5 T according to Eq. (5.42). Due to the narrowness of the maser beam and its short wavelength, the resonance position is a well localized region with an extent of just a few centimeters.

2.2.3. Ion Cyclotron Resonance Heating

The principle of the ion cyclotron resonance heating (ICRH) has already been briefly described in section 5.2.3. Four generators are available on AUG, delivering about 1 MW each. The frequency of these generators is switched simultaneously to the frequencies 30, 36.5 and 40 MHz. The most common heating scheme used for AUG discharges is the hydrogen minority heating. The resonance position of the IC waves is determined by the condition (5.42) and the major radius of the resonance surface is proportional to the magnetic field as it is depicted in Fig. 2.3. The on-axis heating is obtained for magnetic fields of 2.0, 2.45 and 2.7 T, respectively.

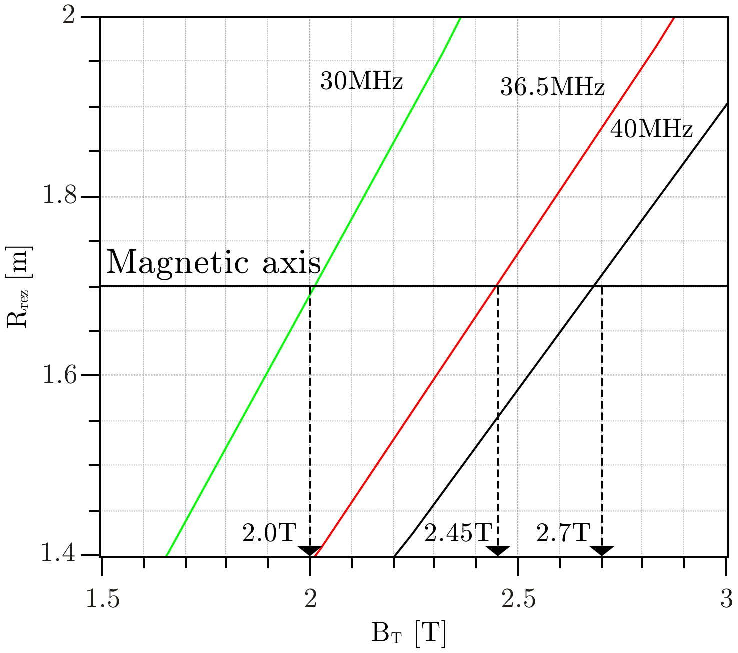

Figure 2.3.: The position of the cold ICRH resonance calculated for the hydrogen minority heating scheme and various values of the generator frequency.

AUG is equipped with two pairs of ICRH antennas, where each antenna of a pair is situated on the opposite sides of the torus (see Fig. 2.2a). During the AUG tungsten program, these antennas were coated by tungsten as well. However, a significant increase in the impurity influx was observed when ICRH heating was used. The strong electric fields in the antenna have accelerated light impurities and increased sputtering of tungsten at the antenna limiters which enhanced the tungsten source. Therefore, limiters of two of the four antennas were coated with boron in 2012. The second antenna pair was redesigned to reduce the RF image currents in the antenna frame and refurbished in 2015. The 3 strap antenna concept was employed [12], effectively reducing the W source by a factor of 2, on the level equal to that of the boron coated antennas. Moreover, by an intentional dephasing of the central and side straps of this antenna, it is possible to modulate the tungsten influx while the heating is kept constant. Therefore, this new antenna also provides a unique tool for W transport studies and modulation transport experiments similar to the one of A. Janzer [13] can be performed.

2.3. Basic Diagnostic

The ASDEX Upgrade tokamak is equipped with an extensive set of diagnostics to monitor the plasma behavior. This can be illustrated by the fact, that about 150 shotfiles and 30 GB of data are recorded for a typical discharge. In the next sections, the most relevant AUG diagnostics for this thesis will be described.

2.3.1. Electron Density

The line integrated electron density is commonly measured by interferometers at tokamaks. Light passing the plasma experiences a small time delay, proportional to the line integrated electron density as the refractive index is changed by the electron density. The phase shift of the laser beam is determined from the interference with a reference signal, and the density is obtained by unwrapping the phase of the measured signal. AUG is equipped with five lines-of-sights (LOSs) of the deuterium cyanide (DCN) laser interferometer system, operating at 195 μm. Additionally, there is a two color system using three CO_2 lasers (at 10.6 μm) and HeNe lasers to compensate for mechanical vibrations of the tokamak vessel [14]. The unfolding is facilitated by the Integrated Data Analysis (IDA) code developed by R. Fisher [15]. Well determined edge profiles are necessary for a reliable unfolding of the line integrated density measurements and therefore the steep pedestal density profile is measured by a dedicated lithium beam diagnostics. In addition to that, n_e is measured independently by the 16 channel core

Thompson scattering (TS) system [16]. The density is proportional to the intensity of the scattered light and in contrast to the interferometers, these measurements are local.

2.3.2. Electron Temperature

The electron temperature is measured by electron cyclotron emission (ECE). The gyrating electrons on their orbits emit photons due to the cyclotron radiation on their gyro-frequency and higher harmonics. If the plasma density is high enough, the plasma can be considered as optically thick at these frequencies, and radiate as the black-body. The radiation intensity is then approximated by the Rayleigh-Jeans formula

$$I = \frac{\omega^2 k T_e}{8\pi^3 c^3}.$$

In such a case, the radiation intensity is proportional to the electron temperature T_e, independent of the electron density. The frequency of the radiation is given by the Larmor frequency and hence depends on the local value of the magnetic field. Therefore, the radial coordinate of the radiation origin can be directly deduced. The toroidal positions of the ECE measurements in a typical AUG discharges are depicted in Fig. 2.2.

The electron cyclotron emission is measured on AUG by a 1D ECE Heterodyne radiometer operating in the X-mode at the second harmonic [17]. This radiometer has 60 channels which are sampled at 1 MHz rate on different consecutive frequency bands. Therefore, this diagnostics provides measurements of the electron temperature with rather high temporal and spatial resolution. The level of accuracy is expected to be about 7% in the absolute value of the temperature due to the calibration uncertainty, limited amplifiers stability, non-linearity and other issues. The observed uncertainty in the position of these measurements is about 1 cm, but it will be reduced when a new model for a warm resonance position and ray tracing will be applied [18].

The electron temperature profiles are also routinely monitored by the vertical Thompson scattering diagnostics (VTA) [19]. This diagnostic measures the Doppler broadening of the light from the very intensive laser pulses scattered by the free electrons in the plasma. However, due to a larger uncertainty and low laser repetition rate, the profiles from the ECE diagnostics are usually preferred in the present work.

2.3.3. Ion Temperature and Rotation

The temperature, rotation, and density of the light impurities are measured by the active charge exchange spectroscopy (CXRS) system. This experimental technique relies on the charge exchange process between a donor neutral D^0 provided by the NBI and an impurity I^{Z+} in the plasma:

$$I^{Z+} + D^0 \longrightarrow I^{(Z-1)+^*} + D^{1+}.$$

The electron captured by the impurity stays for a short time in the excited state and then experiences a radiative decay leading to a cascade of transitions to the ground level. The light emitted during specific transitions is analyzed spectroscopically, and the impurity velocity and temperature with the corresponding statistical uncertainty can be evaluated from the Doppler shift and broadening of the measured spectral line. The impurity temperature is assumed to be equal to the bulk ions, due to significant collisional energy exchange. As predicted by neoclassical theory, the toroidal velocity of the light impurities is slightly lower than of the bulk ions, but the difference is typically less than 5% in the core. The neoclassical correction can be found using the TRANSP (NCLASS) code or an analytical formula [20].

In 2010, an improved core CXRS system (CER) was installed at ASDEX Upgrade [21]. The profiles are now measured along 25 lines of sight (LOS) which cross the NBI path from Q3 beam slightly above the mid-plane between the magnetic axis and the pedestal top (see Fig. 2.2). The CXRS spectra are routinely measured with 10 ms integration time on impurities present in the plasma, typically either B, C or N. After a boronization for wall conditioning the intensity of the boron line dramatically increases and, therefore, the visible boron CX line B V 7-6 (494.467 nm) is preferred. When the boron concentration decreases, the carbon line C VI 8-7 (529.059 nm) can be utilized. In the nitrogen seeding experiments, the line NVII 9-8 (566.937 nm) must be measured because the carbon and boron spectra are partially disturbed by the nitrogen lines.

3. Diagnostics of High-Z Impurities Density in AUG

Since the main focus of the thesis is the high-Z impurity transport, diagnostics regularly used for monitoring of the heavy ions will be introduced in this chapter. The available diagnostic systems can be split into two groups: diagnostics providing many lines of sight (LOS) with a possibility of tomographic reconstruction like the foil and diode bolometers, SXR diagnostic and energy resolved but spatially integrated diagnostics – VUV and SXR spectrometers. The advantages and limitation of each diagnostic in the monitoring of tungsten density will be discussed.

3.1. Foil Bolometers

Foil bolometers are an essential diagnostic designed for the measurement of the radiated power. Ideally, the sensitivity of the bolometers should be constant over the whole relevant radiation range of the plasma, i.e. from UV (1 eV) to SXR (1 keV). Because all materials are highly absorbing photons in the VUV range, optical components and refractive optics cannot be used to transmit the radiation. Therefore, simple pinhole cameras inside of the vessel are employed. In the foil bolometers, the energy of the incident photons is absorbed by a thin metal foil and converted to heat. The foils installed on AUG are from $4.5\,\mu$m thick platinum [22], because only chemically inert metals can withstand a long-term activity of charged radicals without deterioration of their properties. The metal foil acts like a resistor ($1200\,\Omega$) and heating of the foil will slightly increase its resistance. The change in the resistance is measured by a balanced Wheatstone bridge, comparing the exposed foil resistance with an identical foil shielded from the radiation. The bridge is powered by a 500 Hz alternating square signal and the voltage difference between each phase provides a robust measurement of the change in the resistance, immune to the small offset drifts in the signal level. The impulse response function (IRF) of the diagnostic is determined by a finite thermal capacity and heat conductivity of the metal foil. The IRF is close to an exponential curve with a decay time of about 250 ms, measured after each discharge for each channel. The instantaneous incident power is thus obtained by a temporal deconvolution of the measured signal. The effective temporal resolution of the diagnostic is between 5–100 ms, depending on the signal/noise ratio (SNR).

The foil bolometers deliver the absolute radiated power because the metal foils absorb all the incident photons from the UV to the SXR range. A comparison of the relative calibration between the bolometer cameras and foil assembly within the cameras has indicated discrepancies in the range of 10–20 % and we have attempted to compensate for them. Still, some systematical errors can arise due to reflections of UV light within the cameras, stray ECRH radiation or neutrals [23]. The first two issues were significantly reduced by a combination of grooved surfaces and TiO_2/Al_2O_3 anti-reflection coating [24]. In order to avoid the stray ECRH radiation in the vertical camera, protective grids were installed. Nevertheless, still a significant interference can be observed, when LFS ICRH heating at 30 MHz is applied. The setup of LOS of the AUG foil bolometers can be found in Fig. 3.1a. The plasma is observed through six pinholes

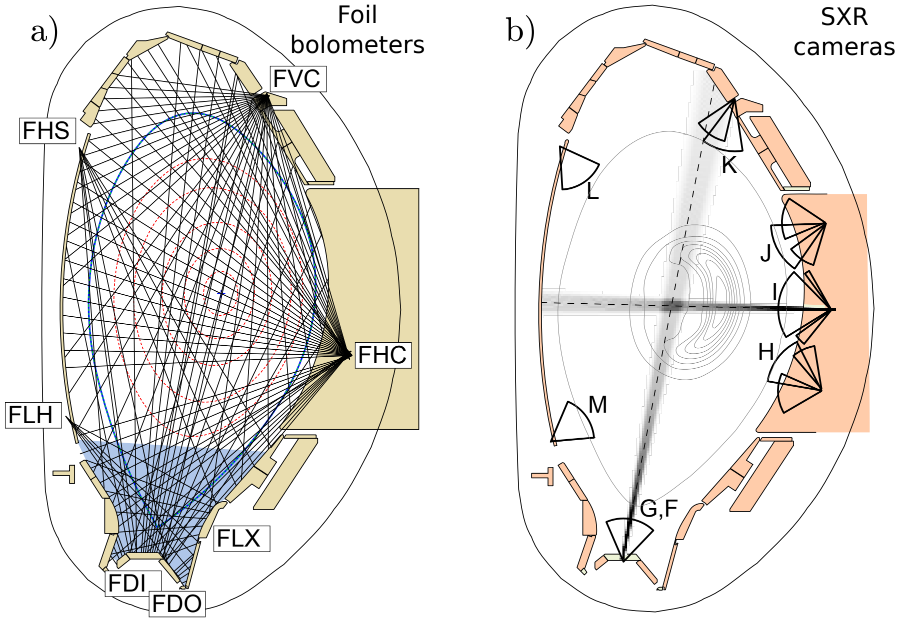

Figure 3.1.: a) Poloidal cross-section of the tokamak illustrating the position of the foil bolometers. The lines of sight crossing the divertor or the X-point region (in blue) are not usable to infer the core radiation, because of a significant contamination by the edge radiation. b) Poloidal projection of the experimental setup of the AUG soft X-ray diagnostic system. The viewing cones of each camera are indicated by black circular sectors. Outboard cameras H, I, J and K are composed of multiple heads each with the slit in the same position. The viewing geometry of the F camera is similar to that of the G camera. However, F is toroidally separated by 137° from the other cameras. In gray the volumes of core LOSs from the G and I cameras are shown and in the background, contours of the real SXR emissivity are presented.

providing a full coverage of the poloidal cross-section with a densely covered region around the X-point. Since only line-integrated measurements are available, the local value of the plasma emissivity must be derived by a tomographic reconstruction. The tomographic code developed by C. Fuchs [25] and later improved by M. Bernert [24] is regularly utilized on AUG. This code is optimized for reconstruction of the divertor region which represents the dominant source of radiation in common discharges. The tomography results are manually tuned by adjusting of the smoothness and the diffusion anisotropy independently for the main plasma and X-point region. Due to a necessary human input for each reconstructed time point, this procedure is highly impractical for the monitoring of many discharges in high temporal resolution. Therefore, a new tomography code, described in the next chapter was developed, providing significant improvements for discharges with a large fraction of the core radiated power. For the reconstruction of the core emissivity are suitable only the LOSs which are not crossing the X-point area, because these are contaminated by a high edge radiation and therefore only some LOSs of the FVC and FHC cameras can be used. Moreover, a typically hollow radiation profile makes the tomographic reconstruction of the core emissivity a rather difficult task.

The measured radiation $\varepsilon_{\mathrm{BOLO}}$ can be interpreted using the cooling factors L_z [Wm^3] for plasma ions and impurities

$$\varepsilon_{\mathrm{BOLO}} = n_e \sum_z L_z n_z = n_e^2 \sum_z L_z n_e c_z, \tag{3.1}$$

where c_z is the concentration of species Z with density n_z. The cooling factors depend primarily on the electron temperature, but also on the level of the impurity transport [26]. However, the influence of the ion transport on the cooling factor of tungsten can usually be neglected due to very fast recombination and ionization rates. The dependence on electron density is weak for the relevant density range and therefore it is neglected in the present work. The electron temperature dependence of the cooling factors is characterized in Fig. 3.2. Detailed derivation and validation of the L_z are given in Refs. [27–29]. The comparison between various sets of atomic data indicates discrepancies in the range of a factor of 2. For charge states above W^{26+} at a temperature $T_e > 0.7\,\mathrm{keV}$ the calculations are performed in elaborate details, and thus the credibility of the atomic data should be higher. Finally, the cooling factor is changing only by a factor of 2 in the temperature range relevant for a core of a regular AUG discharge (i.e. 1–5 keV). Therefore, the temperature dependence is considered to be weak, and the uncertainties in the measurement of the electron temperature do not play an influential role in determining the W density. The foil bolometers are considered as an ideal candidate for a W diagnostic because of the highest credibility of the atomic data and an absolute calibration. Consequently, the other diagnostics were cross-calibrated with respect to the W density determined from the foil bolometer measurements. A summary of the main pros and cons of the foil bolometers can be found in Tab. 3.1.

Pros	Cons
Absolute calibration	Low SNR
The most reliable atomic data	High level of the edge radiation
Weak dependence of L_W on T_e	Poor temporal resolution (10–200 Hz)
	Low number of useful LOSs

Table 3.1.: Overview of the main advantages and disadvantages of the foil bolometers for the monitoring of the W density.

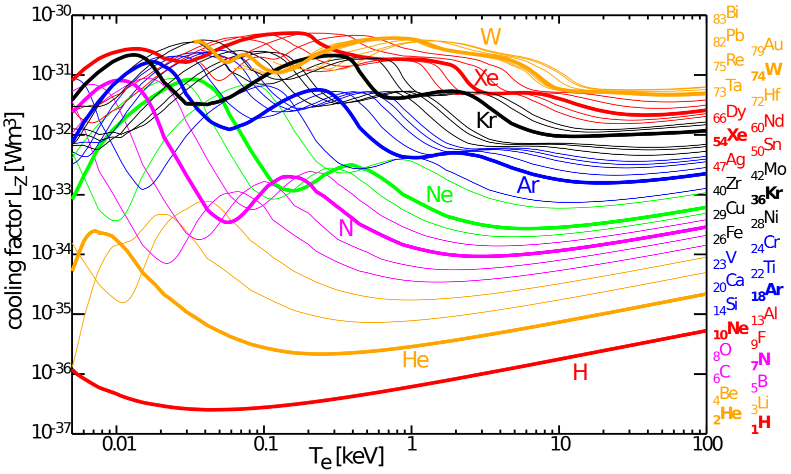

Figure 3.2.: Cooling factors produced by a set of codes from ADAS [30] for many elements between H and Bi [31]

3.2. Soft X-ray Cameras

The description from this section is published in [32]. The current SXR system has been operational since the year 2006 [33]. The diagnostic consists of 15 miniature heads with separate pinholes and chips, assembled to 8 cameras named F, . . . , M resulting in a total of 209 LOSs (see Fig. 3.1). The cameras H, I and J have three heads each; camera K has two and cameras F, G, L and M have only one head each due to spatial constraints in the divertor and between the wall tiles. The design of all heads is identical, with the slit of size 0.3×5.0 mm^2 a distance between slit and chip 14.0 mm. Each array of diodes SXR-diodes is centered perpendicularly to the axis of the heads.

The heads are equipped with a linear array of 35 Centronic Series 5T (LD35-5T) diodes of size 4.6×0.96 mm^2 with 30 μm separation. The diodes are shielded by circularly bended Be foils attached behind the slits. The measured foil thickness is 75 μm with a relative variability below 5 %. The spectral interval with a detection sensitivity higher than 50 % ranges from 2.3 keV to about 13 keV as is shown in Fig. 3.3. In order to limit the range of the incidence angles of the measured lines of sight, roughly only half of the diodes close to the chip center are utilized. Despite this restriction on the incidence angles, the effective thickness of the diodes can vary by 12 % (cameras H, J) up to 19 % (camera I) between the central and the edge diodes. The increased effective thickness enhances the sensitivity only for photons with energies above 7 keV, which are usually not emitted in the cold edge plasma observed by the edge diodes.

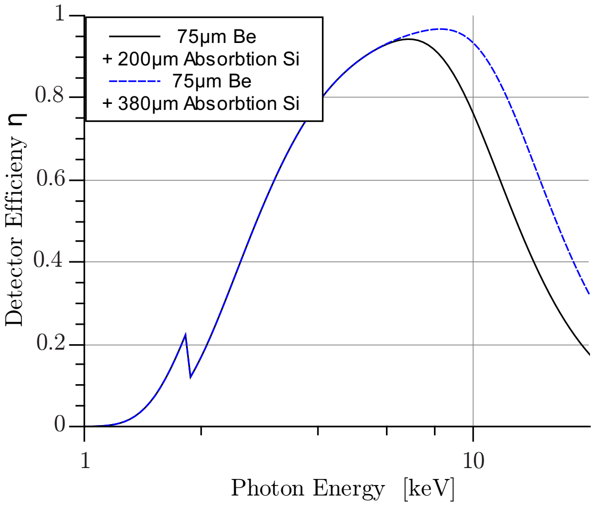

Figure 3.3.: The spectral sensitivity of a diode with a 75 μm thick Be filter, 0.55 μm of a Si_3N_4 passivating layer and a 0.6 μm thick dead layer for two different values the photosensitive layer thickness - 200 μm and 380 μm [34]. The lowest limit of the thickness is estimated to be equal to the electron diffusion length as was estimated in [35]. The maximum active layer thickness is given by the thickness of the diode Si substrate (380 μm).

The positions of all cameras and their observation cones are depicted in Fig. 3.1b. Camera F is situated in the tokamak sector 5 of 16, while the rest are in sector 11 separated by 137°. The spatial resolution can be estimated from the width of the volume of sight (VOS) in the plasma core. The full width at half maximum of the vertical VOS of camera F is 7 cm due to the significant distance from the plasma core, but only 4 cm for the horizontal camera I, which is the closest. The available spatial resolution of the tomography is moderately improved by synergies of multiple overlapping camera heads as shown in Fig. 3.1b.

The etendue of the LOSs was calculated by a full 3D model of the VOS including all obstacles in the paths [36, 37]. The toroidal spreading of the VOS and the toroidal curvature of the plasma column cause an outward radial shift of the VOS centroid in the plasma core of around 5 mm compared to the LOS treatment. The largest radial shift due to this effect is observed for the vertical LOSs of the F,G and K cameras. This effect is included in the tomography in the present work by an analytical correction [36].

The signals from the diodes are measured by two distinct acquisition systems. The older one, measuring 80 LOSs (mainly the H camera and the lower half of the I camera), is equipped with 12-bit analog-digital converters (ADCs) with a 500 kHz sampling frequency and an 80 kHz low pass filter. The newer system acquires the remaining 128 LOSs with 14-bit ADCs, 2 MHz sampling frequency, and a fixed low pass filter at 500 kHz. Both systems are used for the regular tomographic reconstructions and, therefore, the slower system is interpolated on 2 MHz sampling rate.

The amplification chain is composed of a preamplifier installed close to the tokamak vessel and a two stage main amplifier in a shielded area. The gain of the preamplifier can be varied in the range 3.75–250 μA/V and the main amplifier's gain can be set between 1 and 2^{10}. The power incident on the diodes is estimated from the general factor 3.62 W/A describing the diodes sensitivity in the X-ray range [38]. However, an independent absolute calibration (like in [39]) was not performed on AUG.

3.3. Tungsten Density Measurement

The excellent spatial resolution and high accuracy of the measurement predestine the SXR diagnostic to be the workhorse diagnostics for the monitoring of two-dimensional W density profile in the plasma core. Moreover, it is the only AUG diagnostic suitable for sufficiently accurate measurements of small poloidal asymmetries in the impurity density. The measured SXR radiation is interpreted using the cooling factors L_W^{SXR} which are folded with the energy dependent Be filter transparency and diode sensitivity (see Fig. 3.3). The SXR cooling factor normalized by a total cooling factor for bolometers is depicted in Fig. 3.4. The cooling factor is changing between 1 and 3 keV by more than 2 orders of magnitude and between 3–10 keV it is roughly constant. Such a strong dependence of L_W^{SXR} on the electron temperature causes significant uncertainties in the low-temperature regions, because the uncertainty in T_e measurements propagate to the W density measurement. Moreover, the accuracy of the W density measurement depends strongly on the atomic data quality. Since the SXR diagnostic is not absolutely calibrated, large systematical errors can be present in the absolute level of the W density. Therefore, we have invested a significant effort to the cross-calibration of this SXR diagnostics with respect to the foil bolometers.

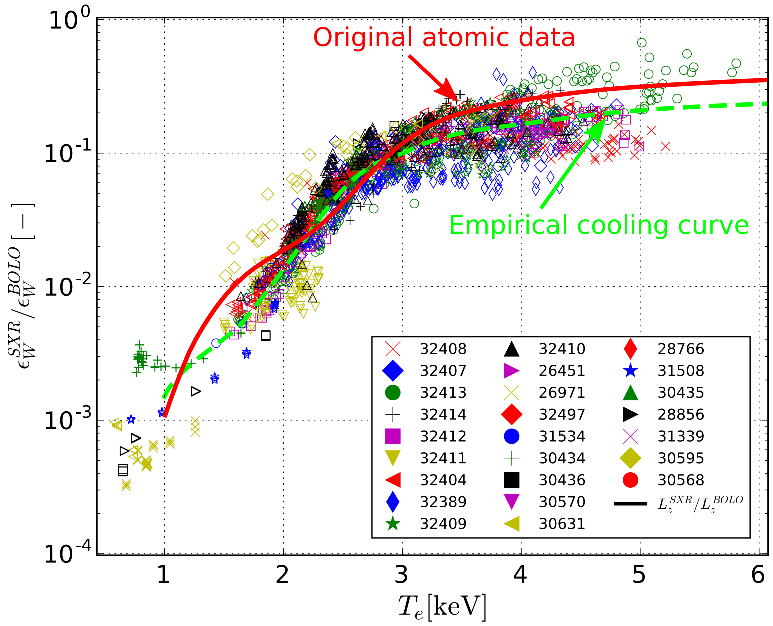

Figure 3.4.: Markers correspond to the experimentally measured ratio between the SXR emissivity from tungsten and the total emissivity measured by the foil bolometers. The red line indicates the expected dependence determined from the ratio of the spectrally folded and the total cooling factor, while the green line is a spline fit.

At first, the level of the experimentally observed bremsstrahlung was compared with the computed bremsstrahlung for discharge #31697. The unique property of this discharge is a rather high electron density (about $1.4{\cdot}10^{20}\,\mathrm{m}^{-3}$) and very low impurity content. The boron concentration, measured from CXRS, is about 0.15%, the nitrogen level is below 0.05%, and the W concentration is about $5 \cdot 10^{-6}$. Also, the level of the other impurities is presumed to be negligible. The electron temperature and density profiles were determined from the Thompson scattering diagnostics. The measured SXR bremsstrahlung in the temperature range between $1 - 1.5\,\mathrm{keV}$ is by a factor of $2{\pm}0.2$ larger than expected from the measured electron temperature and density, indicating a significant calibration error. A further verification using other high-density discharges, including He discharges, has confirmed this conclusion. However, the exact cause of such major discrepancy is unknown and cannot be found without a proper *in situ* calibration of the SXR cameras.

The second part of the investigation involved the comparison between the tungsten emissivity observed by the foil bolometers and the SXR radiation as measured by the AUG SXR system. For this analysis, a set of discharges with a high W concentration was chosen. The regions of the discharges, where the observed SXR radiation did not exceed the bremsstrahlung level by at least a factor of 2 or when $T_e < 1.5\,\mathrm{keV}$ were excluded. As an exception, the discharges with core W accumulation were included, because the extremely high W concentration allowed to study its radiation at even lower temperatures. The obtained ratios of the SXR vs. the total emissivity can be found in Fig. 3.4. The uncertainly at high temperatures is dominated by the inaccuracy in the reconstructed emissivity from the foil bolometers, while at low temperatures the uncertainty in the bremsstrahlung level, electron temperature and also SXR reconstruction dominate. Despite this, a discrepancy between the calculated cooling factor (red line) and the spline fit of the measured data (green) is visible for temperatures below 2 keV and also for temperatures above 3 keV. In the low-temperature region, the observed SXR radiation is roughly 4 times smaller and in the high-temperature region it is about 1.5 times lower than expected from the atomic data. Assuming, that the SXR brightness is overestimated by a factor of 2, as the bremsstrahlung measurement suggests, the discrepancies are even larger. The only possible explanation is the combination of an imprecise model of the diode sensitivity with a large uncertainty in the atomic data. The correction factors identified in this section have a critical importance for the evaluation of the W transport coefficient in the temperature range below 3 keV. Ignoring the corrections would lead to a noticeable influence on the evaluation of the transport coefficient. Similarly to the previous diagnostics, the key properties of the SXR diagnostics are summarized in Tab. 3.2.

Pros	Cons
Excellent time resolution (80–1000 kHz)	**Strong dependence of L_W on T_e**
High spatial resolution	Bremsstrahlung can exceed W radiation
Excellent SNR	Absolute calibration is not available
Sufficient accuracy to observe the poloidal asymmetries in W density	

Table 3.2.: Overview of the main advantages and disadvantages of the SXR diagnostic

3.4. VUV and SXR Spectrometers

The previously discussed diagnostics do not allow for an energy (i.e. spectral) resolution of the plasma radiation. However, AUG is also equipped with spectrometers covering the VUV and SXR range. The most important spectrometers for the determination of the W density will be introduced in this section. The LOS of the spectrometers are crossing the plasma core mostly horizontally (see Fig. 3.5) and therefore the measurement should not be affected by the in-out asymmetries in the W density.

3.4.1. Grazing Incidence Spectrometer

The essential tool for the energy resolved W analysis is a grazing incidence (GI) spectrometer manufactured by the McPherson company. A detailed description is given in [40], while here only the major features will be mentioned. The radiation from the plasma passes through a slit and then it incidences on a grating under a grazing incidence angle $\alpha = 2°$. This angle is necessary to reduce the absorption of VUV light, but also to increase the effective grooves density from the direction of the incident beam. The VUV radiation can be analyzed in the range between 2–50 nm (25–600 eV). The dispersed radiation is detected by two independently movable micro-channel plates (MCP), each observing a wavelength range of about 4 nm. The electrons produced by the MCP are accelerated to a phosphor layer installed behind them, and the fluorescent light is transported to a linear array of diode detectors via bundles of optical fibers. Finally, the data acquisition system record the signal with 1 kHz frame rate.

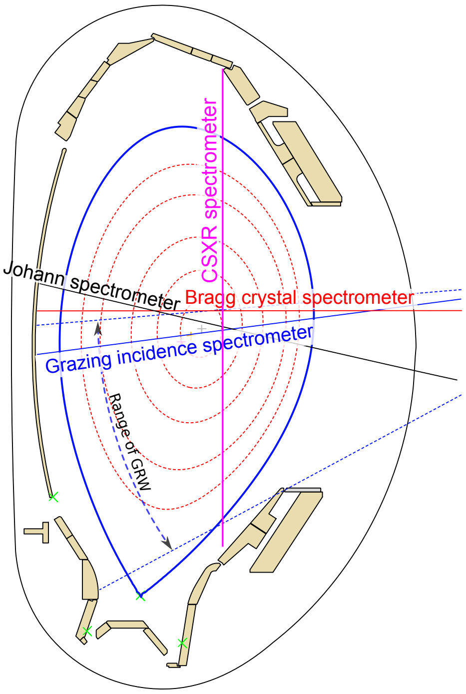

Figure 3.5.: The geometry of LOS for the VUV and SXR spectrometers available on AUG.

The tungsten concentration is routinely evaluated from the quasi-continuous radiation feature between 4–7 nm shown in Fig. 3.6. This feature is composed of many inseparable lines from ion stages W^{27+}–W^{35+} occurring at temperatures between 0.8–1.8 keV. This feature is observed by the first MCP, while the second MCP observes W lines between 12–16 nm originating from the ions W^{40+}–W^{45+}, corresponding to the temperature range 1.8–5 keV. The radiation observed by the spectrometer is integrated along the LOS, however, because the radial region where the ions exist may be relatively narrow, some spatial resolution may be obtained as well. The measured intensity $I_W(\lambda)$ is given by the equation

$$I_{W^{z+}}(\lambda) = C(\lambda) \int_{\mathrm{LOS}} n_e n_w f_z(T_e) \mathrm{PEC}(\lambda, T_e) \mathrm{d}l \tag{3.2}$$

where $C(\lambda)$ is an absolute calibration constant, f_z stands for the fractional abundance of the ion z and the photon emissivity coefficients (PEC) are obtained from the collisional-radiative model. Since the temperature dependence of f_z is much stronger than that

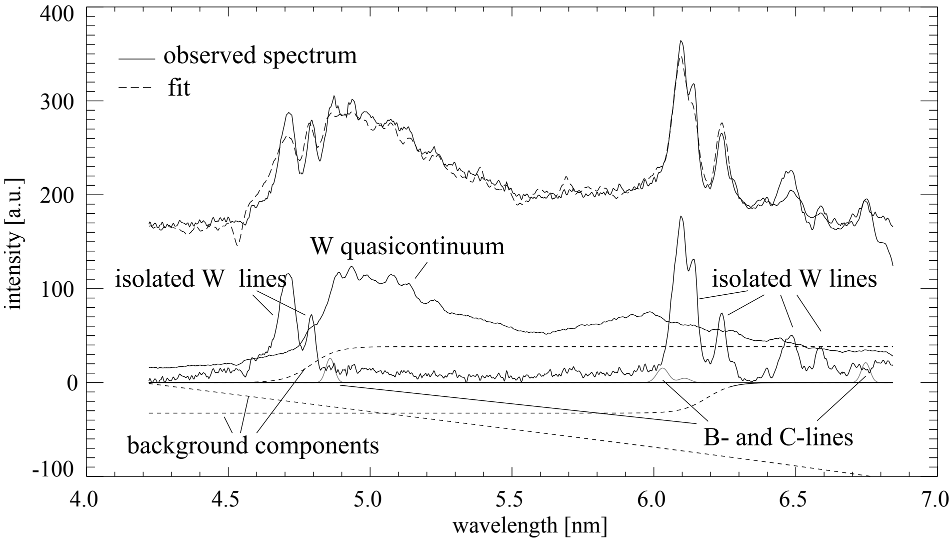

Figure 3.6.: The comparison of the measured and fitted spectrum of the W quasi-continuum feature. Additional to of the quasi-continuum there are also individual spectral lines of tungsten. (Taken from [41])

of the PEC, the radial profile of the emissivity is mostly determined by f_z. Assuming that n_w is constant over the relevant temperature and the corresponding radial range, the tungsten density can be evaluated from Eq. 3.2.

The absolute calibration of the spectrometer is based on the injection of the tungsten impurity and comparison with respect to the W density estimated from the foil bolometers. More details about these calibration procedures and the used atomic data are provided in [13, 27, 42].

Since the GI spectrometer is routinely utilized for the evaluation of the W density, it is imperative to validate the measurement with respect to the foil bolometers. Such comparisons were performed on the subset of discharges used for the cross-calibration of the SXR diagnostic (Sec. 3.3). The W density from the bolometer weighted by a fractional abundance of the investigated ions and normalized by the W density estimated from the calibrated GI spectrometer is given in Fig. 3.7. A clear negative dependence of the electron temperature can be observed for the high-temperature lines in Fig. 3.7b. The W density determined from the quasi-continuum (Fig. 3.7a) is roughly 50 % overestimated and without a clear temperature dependence. The only exception are discharges with W accumulation deviating for $T_e < 1.2\,\mathrm{keV}$, possibly because the profiles in the region of the accumulation show rather steep gradients and the assumptions behind the method used to evaluate the W density from the spectrometer are violated. The other discrepancies are within of the expected uncertainties of the atomic data. The difference in the W density estimated from the bolometer and GI spectrometer can

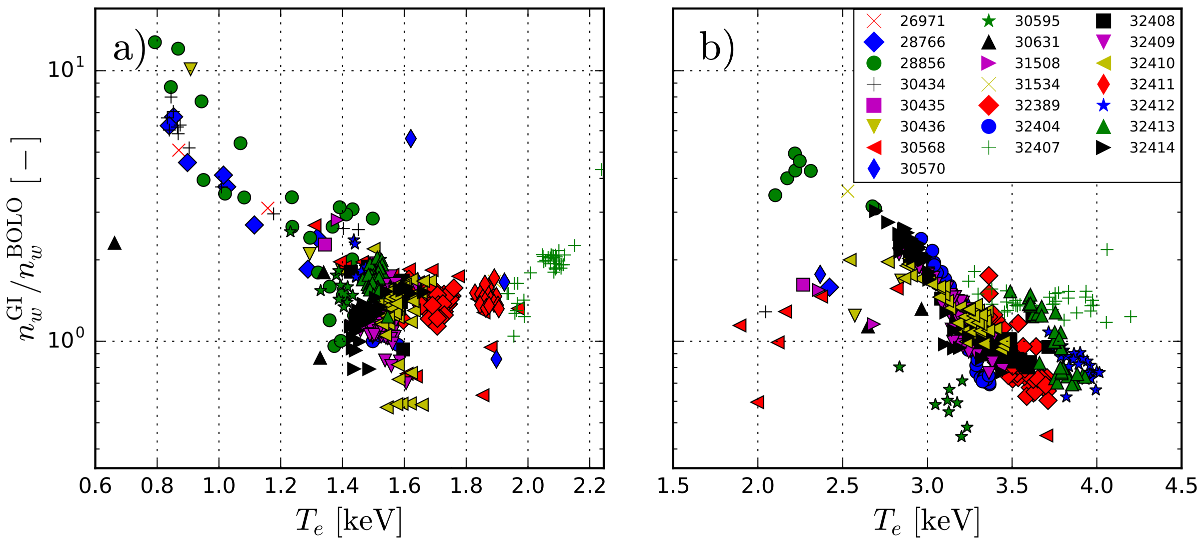

Figure 3.7.: Ratio of the density estimated from the GI spectrometer and from the bolometers for a) quasi-continuum feature from ions stages W^{27+}–W^{35+} and b) lines from ion stages W^{40+}–W^{45+}.

be diminished if the investigation is limited only to hot discharges with the core electron temperature above 4 keV, which fulfill all discharges studied in the experimental part of this thesis.

3.4.2. Johann Spectrometer

The Johann spectrometer (JS) uses a bent quartz crystal ($2d = 4.25$ Å) with a curvature radius R as a dispersive element. The entrance slit and the detector have to be localized tangentially on the Rowland circle with a radius $R/2$. The Bragg diffraction on the dense and regular periodic grid of the crystal, enables to achieve very high resolving power of $\Delta\lambda/\lambda$ about 1000. The Johann spectrometer on AUG is configured to monitor the single ion stages W^{44+}, W^{45+} and W^{46+} with 3 ms time resolution. These ions occur in the temperature range between 2.4 and 6 keV and therefore the information provided by the JS is highly redundant with the SXR diagnostic, which in addition provides much higher temporal and spatial resolution. The JS has an advantage, if other heavy impurities radiating in the SXR range are present because the measurement is not disturbed by their presence on the contrary to the standard SXR diagnostic.

3.5. Summary

In this chapter, a detailed description of the diagnostics crucial for the evaluation of the W density was provided. Each W diagnostic covered a slightly different part of the plasma parameter space. This is illustrated by the Fig. 3.8, where the dependence of the minimal necessary signal level on T_e and c_W was analyzed. The bolometric measurements require a very high W concentration in order to exceed the edge radiation that is usually dominating and also to increase the SNR. The SXR diagnostic requires higher temperatures and a W concentration high enough to significantly exceed the bremsstrahlung level. And finally, the spectrometers can observe W radiation already from a very low concentrations, over a broad range of temperatures but with very limited spatial and temporal resolution. The best diagnostic coverage is achieved in the high-temperature discharges with significant tungsten concentration, which is typically related to a low or a moderate electron density and a large fraction of the core electron heating preventing core W accumulation. Since clear discrepancies were observed between the available W diagnostics, the cross-calibration with respect to the foil bolometers was performed. This calibration step has significantly improved the reliability of the impurity transport analysis.

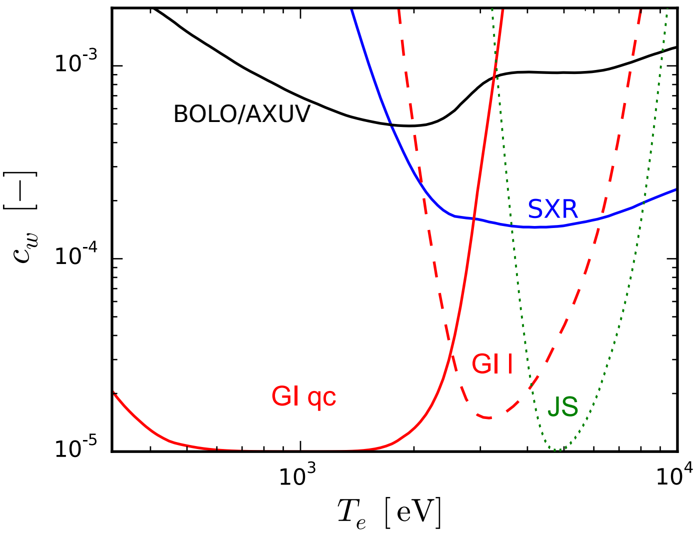

Figure 3.8.: Contours of the minimal signal level in the parameter space of electron temperature T_e and tungsten concentration c_W shown for all available AUG W diagnostic. The other plasma parameters were obtained from the standard AUG H-mode discharge.

4. Tomographic Reconstruction of the Local Emissivity

The study of the poloidal and radial transport requires monitoring of the tungsten dynamics over the whole poloidal cross-section of the plasma with high accuracy and excellent spatial and temporal resolution. However, the diagnostics essential for revealing the W distribution described in Chapter 3 provide only line integrated measurements of the plasma emissivity. Therefore, a mathematical procedure called *tomography inversion* is exploited in order to recover the local emissivity from the line integrated brightness. Tomography is a naturally ill-conditioned problem, which means that a small perturbation in the measurements can cause unacceptably large errors in the tomographic reconstruction. This is resolved by introducing prior knowledge via the so-called *regularization*. Since the conclusions from a tungsten transport experiment relies on the excellent quality of the inverted emissivity profiles, a lot of effort has been invested into developing, testing and validating an advanced tomographic reconstruction code.

In the first part of this chapter, we will provide a brief introduction to the problem of the tomographic inversion with a limited number of lines of sight. In the second part, the reconstruction method is validated by reconstructing the artificial emissivity profiles. Moreover, the reconstruction uncertainty is investigated as well. The final part of the chapter is dedicated to a quantification of the poloidal asymmetries. Parts of this chapter are published in [32].

4.1. The Tomography Problem

The pinhole camera does not directly measure the local emissivity, but only a signal integrated over the volume of sight (VOS). The goal of tomography is thus to reveal the best estimate of the local spatial distribution of the emissivity. The power P_i incident on the detector i is given by

$$P_i = \iiint_{\mathrm{VOS}} \frac{\Omega_i(\mathbf{r})}{4\pi} G(\mathbf{r}) \mathrm{d}V, \tag{4.1}$$

where the integration is done over the whole volume observed by the detector; $\mathbf{\Omega}_i(\mathbf{r})$ denotes the solid angle of the cone from the exposed surface of the detector and $G(\mathbf{r})$ is the emitted power density in W/m^3, i.e. the spectral power density integrated over the sensitivity range of the detector. The brightness b_i (in units W/m^2) can be expressed via the *etendue*, defined as the product of the solid angle $\mathbf{\Omega}_i$ and the area A perpendicular to the axis of the cone $\mathbf{\Omega}_i$

$$b_i = P_i \frac{4\pi}{\langle A\Omega_i \rangle} = \iint \mathcal{T}_i(R,z) G(R,z,\varphi) \mathrm{d}R \mathrm{d}z. \tag{4.2}$$

The coordinates R and z correspond to the horizontal and vertical directions in the poloidal tokamak cross-section, φ represents the toroidal angle and $\langle \cdot \rangle$ represents the average value over the diode surface. Since the toroidal extend of the VOS is small, a variation of the emissivity G in the toroidal direction will be ignored. The operator $\mathcal{T}_i$ then introduces a mapping of the 2D emissivity G to a discrete measurement b_i. This operator is defined as follows:

$$\mathcal{T}_i(R,z) = \int \frac{\Omega_i(R,z,\varphi)}{\langle A\Omega_i \rangle} R \mathrm{d}\varphi \tag{4.3}$$

and describes the geometric properties of the diagnostics. The equation (4.2) for b_i represents the Fredholm integral equations of the first kind, which will be solved by a discretization on a rectangular grid with the total number n of volume elements (pixels). Thus, the problem can be rewritten as a set of m linear equations for m detectors

$$b_i = \sum_{j=1}^{n} T_{ij} g_j \qquad i \in 1, \dots, m \tag{4.4}$$

$\mathbf{T} \in \mathbb{R}^{m,n}$ denotes a geometry matrix, defining the contribution of a pixel j to the measurement i and g_j is the local emissivity at the j-th pixel in units of W/m^3. The measured brightness $\hat{b}_i$ is subject to experimental errors. Therefore, $\hat{b}_i = b_i + \xi_i$, where ξ_i represents a random error with zero mean and a variance of σ_i^2.

4.1.1. Tikhonov Regularization

The system of equations obtained by discretization of the Fredholm integral equations is ill-posed and for the plasma tomography also usually significantly under-determined ($m \ll n$). A common method to find a unique and sensible solution is the Tikhonov-Philips regularization [43] in the general form, which searches for a minimum of the functional $\Lambda(\mathbf{g})$ given by

$$\Lambda(\mathbf{g}) = (\mathbf{Tg} - \hat{\mathbf{b}})^T \mathbf{\Sigma}^{-1} (\mathbf{Tg} - \hat{\mathbf{b}}) + \lambda O(\mathbf{g}). \tag{4.5}$$

The first term stands for the data fidelity, i.e. the residuum weighted by the expected covariance matrix $\mathbf{\Sigma}$, $O(\mathbf{g})$ denotes a regularization functional and λ is a positive regularization parameter balancing the strength of a priori constraints with respect to the goodness of fit. For the sake of simplicity, we will further assume that $\mathbf{T}$ and $\mathbf{b}$ are already weighted by a square root of the covariance matrix

$$\mathbf{T} \leftarrow \mathbf{\Sigma}^{-\frac{1}{2}} \mathbf{T} \qquad \mathbf{b} \leftarrow \mathbf{\Sigma}^{-\frac{1}{2}} \mathbf{b}.$$

In other words, we are removing the ill-posedness of the problem by an intentional biasing of the solution. The biasing is unavoidable and any other approach to solve the tomography is hiding this regularization as well. Using the optimal choice of priori knowledge and a detailed model of the diagnostic, the bias can be minimized.

A priori knowledge about the emissivity profiles is imposed by the operator $O(\mathbf{g})$, which is often some kind of a roughness penalty and a boundary constraint. The regularization operator is typically a quadratic form $O(\mathbf{g}) = \mathbf{g}^T \mathbf{H}(\mathbf{g}) \mathbf{g}$, with a symmetric and positive semi-definite operator $\mathbf{H} \in \mathbb{R}^{n,n}$ which can be a function of $\mathbf{g}$. A common boundary constraint is zero emissivity at the borders, enforced by adding a sufficiently large positive value to the diagonal points of $\mathbf{H}$ corresponding to the pixels outside of the boundary and this is forcing these pixels during reconstruction to zero.

The minimum of Eq.(4.5) can be now expressed as a quadratic optimization problem for a constant positive definite matrix $\mathbf{H}$

$$\Lambda(\mathbf{g}) = ||\mathbf{Tg} - \hat{\mathbf{b}}||_2^2 + \lambda \mathbf{g}^T \mathbf{H} \mathbf{g} \tag{4.6}$$

with the minimum reached at

$$\mathbf{g} = (\mathbf{T}^T \mathbf{T} + \lambda \mathbf{H})^{-1} \mathbf{T}^T \hat{\mathbf{b}}. \tag{4.7}$$

A direct solving of this system of linear system of equations is possible. However, due to the large dimensionality of the matrices ($n \times n$), the high computational complexity $\mathcal{O}(n^3)$ of the inversion, and the required number of inversions to find a proper λ this procedure is highly impractical. Much more efficient algorithms to solve Eq. (4.7) and methods to estimate the optimal value of λ, have been developed within this thesis and more details can be found in the Appendix A. As a result the linear system of equations is typically solved with a complexity $\mathcal{O}(n)$, allowing for large number of pixels n and a fast inversions.

4.1.2. Minimum Fisher Information

We have not specified the **H** operator, yet. The most common regularization operators are the identity operator, suppressing the Euclidean norm of the solution, and the Laplace operator, reducing the curvature of the emissivity profile [44, 45]. Nevertheless, the special features of the SXR profiles, like the peaked distribution of the SXR radiation, the sharp gradients, and the large dynamic range, make the nonlinear Minimum Fisher Information regularization (MFI) [46] an ideal candidate for the regularization functional. This functional can be expressed in the following form:

$$O_{\mathrm{MFI}}(G) = \iint \mathrm{d}S \frac{1}{G} (\nabla_{\mathbf{u}} G)^T \mathbf{J}_2 (\nabla_{\mathbf{v}} G), \tag{4.8}$$

where $\mathbf{u}(x, y)$ and $\mathbf{v}(x, y)$ are two locally orthogonal vector fields and $\mathbf{J}_2 \in \mathbb{R}^{2,2}$ represents a matrix of ones. If $\mathbf{u}$ is parallel with the Cartesian coordinates, the method is called *isotropic* MFI and if $\mathbf{u}$ is locally tangential to the magnetic flux surfaces, the *anisotropic* MFI regularization is obtained. More details about the implementation of the anisotropic MFI can be found in [47]. The regularization operator **H**, representing a linearized and discretized functional (4.8), is given by:

$$\mathbf{H}^{(k)} = \sum_{\ell \in \{\mathbf{u}, \mathbf{v}\}} \mathbf{B}_\ell^T \mathbf{W}^{(k)} \mathbf{B}_\ell, \tag{4.9}$$

where $\mathbf{B}_\ell$ denotes a discretized gradient operator ∇_ℓ and $W_{ij}^{(k)}$ is a weight matrix defined as the inverse of $\mathbf{g}^{(k)}$

$$W_{ij}^{(k+1)} = \delta_{ij} / \max \{g_j^{(k)}, \varepsilon\}.$$

The MFI regularization must be solved iteratively, because the weight matrix W depends on the emissivity $\mathbf{g}$.

4.2. Reconstruction Uncertainty

Assuming that a reconstruction was obtained using Eq. (4.7), the next obvious question is how accurate is the reconstruction and how to estimate the uncertainty of the solution and the derived quantities. The answer is complicated due to the significant contribution of the regularization bias because the bias can represent the dominant fraction of the mean square error (MSE).

In this section, the components of the MSE will be examined, and an analytical formula for the covariance matrix of the solution will be proposed. Additionally, we will describe a way to treat the systematical errors.

4.2.1. Statistical and Regularization Error

The regularized solution of Eq. (4.7) leads to the following expression for the mean square error (MSE) in $\mathbf{g}_\lambda$ (see [32]):

$$\left\langle (\mathbf{g}_\lambda - \mathbf{g}^*)^2 \right\rangle_k = \sum_{i=1}^{r} f_{i,\lambda}^2 \frac{\mathbf{V}_{ki}^2}{D_i^2} + \left[\sum_{i=1}^{m} (1 - f_{i,\lambda}) \frac{\mathbf{U}_i^T \mathbf{b}^*}{D_i} \mathbf{V}_{ki} + \left(\left(\mathbf{I}_n - \mathbf{V}\mathbf{V}^T \right) \mathbf{g}^* \right)_k \right]^2, \tag{4.10}$$

where $\langle \cdot \rangle$ indicates averaging over the fluctuating part, $\mathbf{g}^*$ is the accurate, but unknown, radiation profile and $\mathbf{b}^* = \mathbf{T}\mathbf{g}^*$ is the ideal measurement, also unknown. (For the definition of $\mathbf{V}$, $\mathbf{U}$ and $\mathbf{D}$ see Appendix A.) The first term on the right side describes the variance caused by the statistical uncertainty in the data. The error distribution is assumed to have zero mean, and the standard deviation normalized to one. The term in the square brackets represents the bias of our solution. The left term is the *regularization error* caused by suppressing small features in the measurement $\mathbf{b}^*$. Finally, the last term is a consequence of the rank deficiency of the projection matrix $\mathbf{T}$, and we will call it *singularity error*. The regularization error and the singularity error cannot be estimated without knowledge of the real radiation profile $\mathbf{g}^*$ and the brightness $\mathbf{b}^*$. However, tests were performed on a class of expected emission profiles to estimate the influence of the bias on the reconstructed quantities. When only a weak regularization is applied, all filtering factors f_i will be close to one, and the statistical error will dominate. On the other hand, if high regularization is used, most of the f_i values vanish, and the error is dominated by the regularization error. The singularity error can be reduced only by including a priori knowledge more consistent with the solution (like anisotropic smoothing) and by better angular and spatial diagnostic coverage.

The pixel size of our reconstruction was assumed to be small enough to keep the discretization error negligible. Moreover, the systematic errors in the geometry of the LOSs, their calibration, and other imperfections in the geometry model were not included, because they can be significantly reduced by a self-calibration method as it will be shown in Sec. 4.2.3. Finally, the regularization parameter λ is subject to statistical uncertainty as well. Nevertheless, close to the optimal regularization level, i.e., the value of λ minimizing the MSE, the MSE value is only weakly sensitive to perturbations in λ.

The statistical uncertainty in the reconstructed profile can be assumed as a lower bound for the real uncertainty. Based on the standard uncertainty propagation approach, the covariance matrix of the solution $\mathbf{g}_\lambda$ is given by

$$\Sigma_{ij}^g = \langle (g_i - \langle g_i \rangle)(g_j - \langle g_j \rangle) \rangle = \sum_{k=1}^{r} f_k^2 \frac{V_{ik} V_{jk}}{D_k^2}. \tag{4.11}$$

The tests of the phantom reconstructions performed in the present work indicate that the statistical variance is usually about half of the total MSE. Fig. 4.1a shows a zoom-in of a reconstruction of an artificial profile. The variances Σ^g_{ii} associated with each pixel i can be imaged as is demonstrated in Fig. 4.1b. Further, Fig. 4.1c shows the correlation of a single pixel indicated by the black cross with the neighboring pixels determined from the corresponding row of the covariance matrix. The width and shape of the correlation peak provide an estimate of the local spatial resolution.

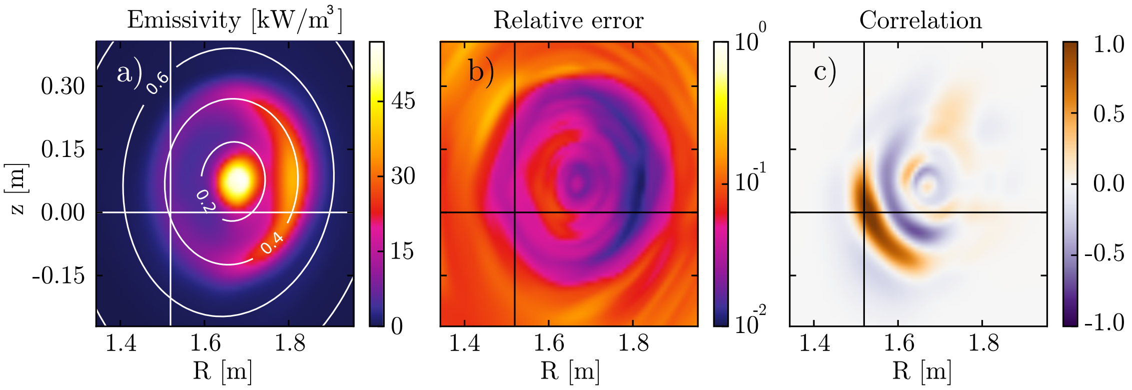

Figure 4.1.: a) The SXR emissivity in the plasma core reconstructed from a phantom by the anisotropic MFI method. The white contours indicate magnetic surfaces. b) The relative standard deviation $\delta_i = \sqrt{\langle g_i^2 - \langle g_i \rangle^2 \rangle} / \langle g_i \rangle$ of the reconstruction is shown. This is estimated from the diagonal of the covariance matrix $\sqrt{\Sigma_{ii}}/g_i$. c) The correlation of the pixel j, indicated by the black cross, to the surrounding pixels determined from the i-*th* row of the covariance matrix Σ_{ji}/Σ_{jj}. The same pixel j is also marked in (a) and (b) of the figure.

4.2.2. Reconstruction of Artificial Radiation Profile

A common way to assess the performance of a tomography method is to reconstruct phantom profiles. We have prepared a set of representative phantoms with increasing complexity, changing from a simple Gaussian function to a very peaked one, sharply hollow one and finally to a complex hollow-peaked asymmetric profile as is shown in the upper row of Fig. 4.2. The reconstructions were evaluated using a fine grid of 100×150 px. Moreover, we have used the anisotropic MFI regularization. The noise level in the brightness, based on real discharge noise, was on average equal to 2 % of the signals in each LOS. The difference between the original and the reconstructed profiles are depicted on the bottom of Fig. 4.2. Only small discrepancies can be observed on the sharp edges of the artificial profiles, which are the consequence of a finite resolution of the SXR diagnostic. No other significant artifact is present, indicating a small role of the regularization bias. Nevertheless, significant artifacts were observed in the real reconstructions, indicating systematic errors in the model of the SXR diagnostic.

4.2.3. Systematic Errors

Unavoidable limitations of the experimentally achievable accuracy are given by the systematic uncertainties in the geometry and calibration of the SXR cameras. Small deviations of the diode positions with respect to the camera slit in combination with their short focal length have a strong influence on the LOS positions and their etendue. A mere 0.2 mm deviation of a diode position leads to a roughly 2 cm shift of the LOS in the plasma core and consequently up to 20 % discrepancies in the measured brightness in the regions of steep SXR radiation.

Position and calibration errors are commonly observed within multi-camera SXR system [46, 48–50], because a large number of viewing angles provides sufficient redundancy of the measurements and the discrepancies can be identified and corrected. In the following text the corrections applied in the present work are explained.

Relative Cross-calibration of the Sensitivity

The relative calibration of the SXR cameras at AUG was estimated for every discharge in an iterative manner. First, the initial calibration factors were used to perform a reconstruction of the whole discharge. Then, a single correction factor for each camera was obtained in order to minimize the deviation between measured data and back-projected brightness. This procedure was repeated until convergence, which was typically achieved in the first step. Tests on the artificial profiles indicate that the cross-calibration can provide estimates with an accuracy well below 0.1 %. The evolution of the cross-calibration factors for five experimental campaigns is shown in Fig. 4.3. The scatter for the core heads is rather low, about 1–2 % within a single campaign. Higher variations are observed in J3 and K1 during the first examined campaign probably caused by a deviation of the Be filter thickness, which was retrospectively measured to be up to 20 μm different from the designed thickness of 75 μm. The higher scatter found in the side heads (green in Fig. 4.3) is caused by a low signal level, residual errors in the positioning of these cameras and uncertainties in the sensitivity and etendue of the off-axis LOSs. Neutron degradation [51] may also be present since the total fluence over the AUG campaign is about $5 \cdot 10^{16}$ neutrons/m^2. However, no signatures of the neutron damage in the relative calibration were observed.

.

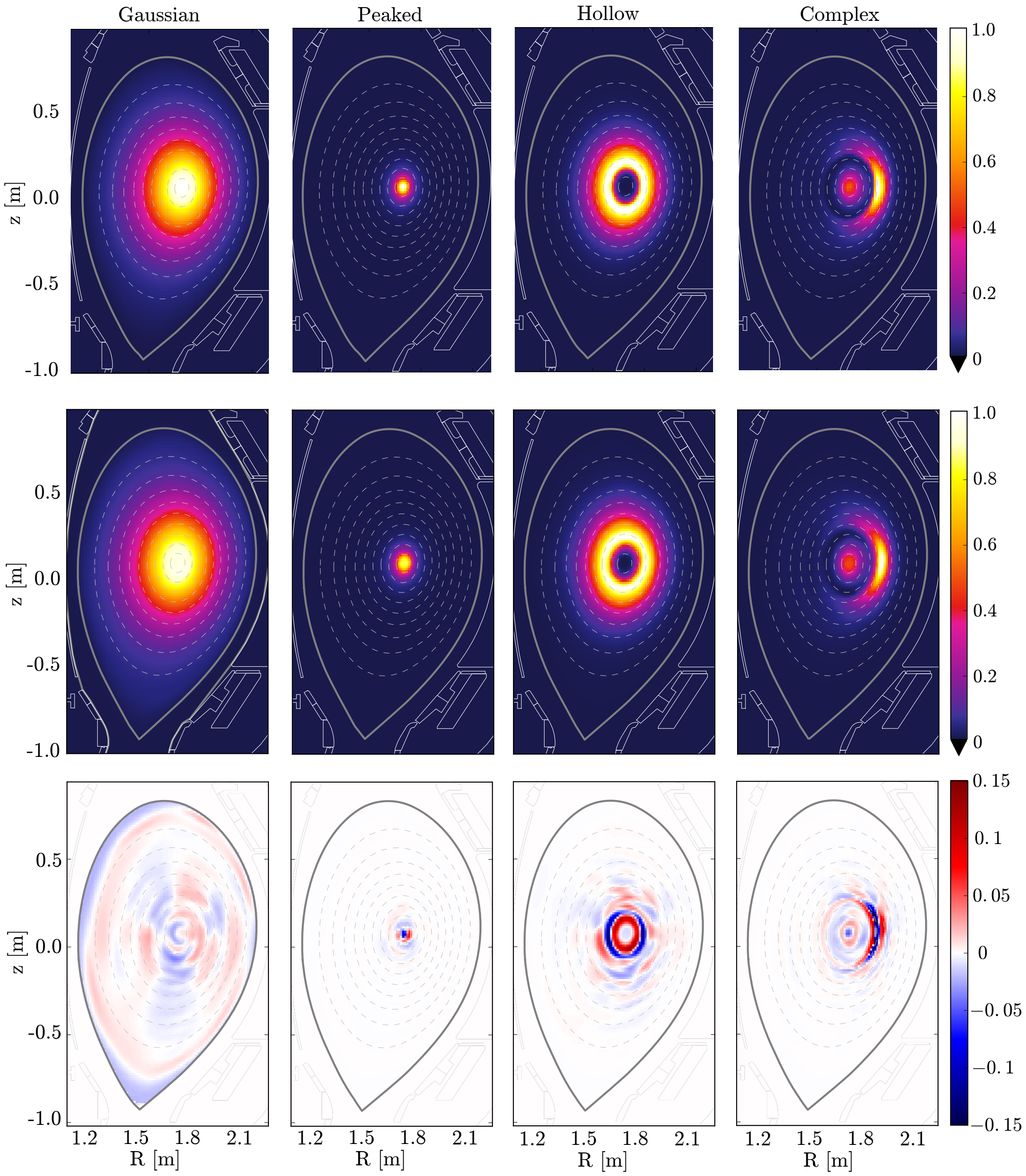

Figure 4.2.: (upper row) Four phantoms used to evaluate the properties of the regularization selection methods. (middle row) The reconstruction of the phantoms with the regularization level estimated by GCV (see Appendix A), which have always been very close to the optimal level. (lower row) Residua between reconstruction and phantoms. All profiles are shown in the same color scale as the phantom profiles.

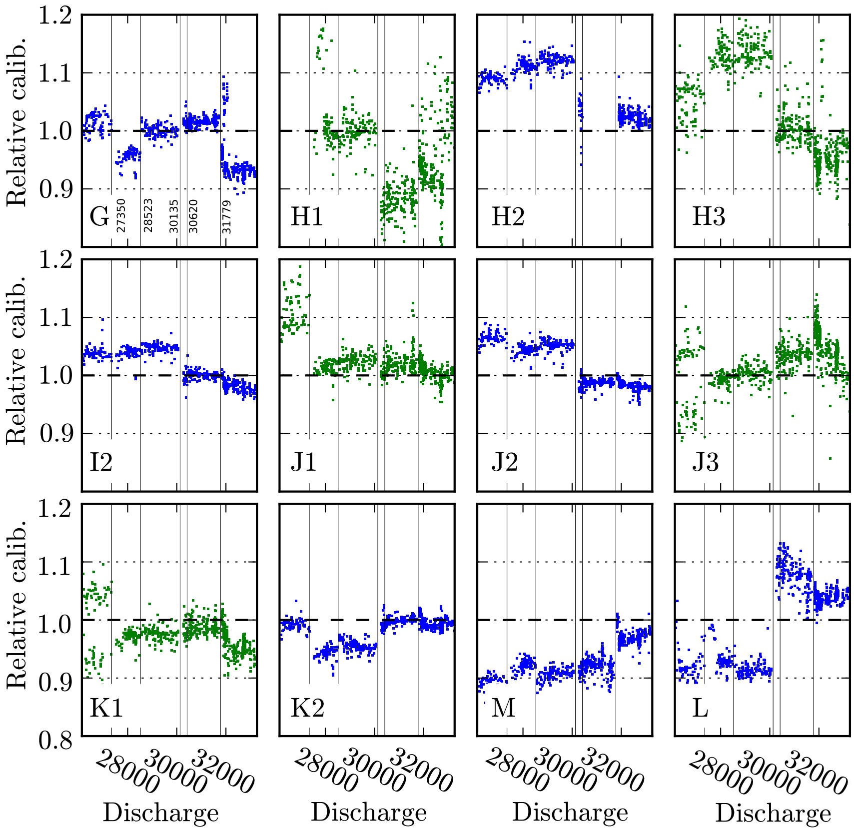

Figure 4.3.: Relative calibration factors for each of the 12 regularly used SXR camera heads evaluated for 758 discharges between 2011 and 2016; the blue points indicate factors for core heads, while the green correspond to the side heads. Vertical lines indicate vents of the chamber, replacing of the diode arrays or Be filters and an extension of the viewing angles for cameras G, L and M.

Adjustments of the Viewing Geometry

The self-consistent calibration of the head positions was obtained in a set of discharges with negligible centrifugal asymmetries and significant variation in the peaking of the radiation profile. The shape of the magnetic flux surfaces was verified by a comparison between the CLISTE code [52] and the TRANSP equilibrium solver [53] constrained by the kinetic profiles. The deviation in the position of the flux-surfaces in the selected discharges was smaller than 5 mm. The optimal position correction was identified by a gradient descent algorithm iteratively modifying the poloidal tilt for each of the 13 heads, to minimize the residuum between the measured brightness and the backprojection. New cross-calibration factors matching the actual geometry had to be estimated in every step. The regularization level was fixed to reduce the number of the nested optimization loops and increase the stability. Additionally, since no poloidal asymmetries were expected in the selected discharges, the solution was kept constant on the flux surfaces by the projection matrix **P** introduced in the section 4.1.1. In the end, the optimal tilt was estimated as a median over the set of tested discharges. The variation in the tilt corrections was about $0°3'$ for the core heads and $0°12'$ for the side heads. The proper cross-calibration and self-consistent positioning of the camera heads have reduced the reconstruction residue by order of magnitude. Further, the suppression of the systematic errors has significantly enhanced the stability and reliability of all regularization selection methods when used in the experimental measurements. Finally, the measurement accuracy of small stationary poloidal asymmetries in the SXR radiation was also significantly improved. Manipulation of the cameras during the maintenance events of the tokamak chamber has always resulted in small position deviations and therefore it is imperative to repeat this adjusting every campaign.

4.3. Evaluation of the Poloidal Asymmetry

In this section, the application of the tomography for the observation of the small stationary asymmetries in the poloidal radiation profile will be discussed. The AUG SXR diagnostic provides a sufficient number of cameras, covering the plasma from various directions (see Fig. 3.1), in order to observe the MHD modes with poloidal mode numbers m of up to 5 [54]. However, the measurement of the stationary asymmetries puts enormous demands on the accuracy of the SXR profile and usually it is not possible to reliably infer more than the first, or rarely first two poloidal harmonics. In this section, the definition of the asymmetry used in the experiment will be provided, and an analysis of the possible uncertainties or systematical errors will be performed.

4.3.1. Definition of the Experimentally Measured Asymmetry

The poloidal asymmetry of impurity density n_z will be defined as the first cosine and sine component in the poloidal decomposition of the profile normalized by the flux surface average $\langle n_z \rangle$, mapped to the ρ, θ coordinates, where ρ is the radial coordinate and θ is angle in Cartesian coordinates. The definition is expressed by the following formula:

$$n_z(\rho, \theta) = \langle n_z \rangle (\rho) \left(1 + \delta(\rho) \cos\theta + \zeta(\rho) \sin\theta + \ldots\right), \tag{4.12}$$

where the cosine component δ will be called the *in-out* asymmetry and the sine component ζ will be denoted as the *up-down* asymmetry. Since the SXR radiation is emitted by multiple species, the observed asymmetry can be associated with the tungsten emissivity only if its radiation significantly exceeds that of the other ions. If this is not the case, the SXR asymmetry is given by

$$\delta = \frac{\sum_z \langle n_z \rangle L_z \delta^{(z)}}{\sum_z \langle n_z \rangle L_z} \tag{4.13}$$

where $\delta^{(z)}$ stands for the asymmetry of the ion species z and L_z are the corresponding cooling factors. Assuming asymmetric radiation of the tungsten and the remaining radiation coming from light impurities with negligible asymmetry, following expression can be found

$$\delta_{\mathrm{SXR}} = \frac{\varepsilon_{\mathrm{W}}}{\varepsilon_{\mathrm{SXR}}} \delta^{(\mathrm{W})}. \tag{4.14}$$

Therefore, the measured asymmetry is reduced by a ratio between the tungsten and the total emissivity with respect to the original W asymmetry.

4.3.2. Main Sources of the Uncertainty

The measured asymmetry is subject to a significant number of inaccuracies, which should be suppressed or at least correctly quantified and propagated in the final estimate of the confidence interval. The uncertainties in the measured poloidal asymmetry originate from the errors in the tomography and the mapping of the emissivity from the R, Z to the ρ, θ coordinates.

The reconstruction uncertainty is composed of the statistical variance and the bias. The statistical variance of the reconstruction is estimated from the covariance matrix (4.11). The random samples from the multivariate Gaussian distribution of the solution provide an estimate of the statistical variance of the asymmetry profile. The regularization bias was investigated by a reconstruction of the poloidally symmetric artificial profile. The careful design of a regularization operator and the other components of the tomography code allowed for a reduction of the deviation in the asymmetry below 2 % from the zero asymmetry. Fig. 4.4 demonstrates the quality of the reconstruction for an asymmetric radiation profile. The discrepancies between the original and the reconstructed profiles are below 0.05 for a complex 2D radiation profile with a large alternating in-out asymmetry and zero up/down asymmetry.

However, in the real discharges, additional imperfections originating from the errors in the geometry, calibration of the SXR diagnostic and position of the magnetic equilibrium are present. The procedure used to reduced the discrepancy between the mutual position of SXR cameras and the magnetic equilibrium was described in Sec. 4.2.3. This self-consistent calibration has significantly reduced the discrepancies between the SXR cameras and the systematical offset of the measured asymmetry.

The last and often the most important source of uncertainty is the accuracy of

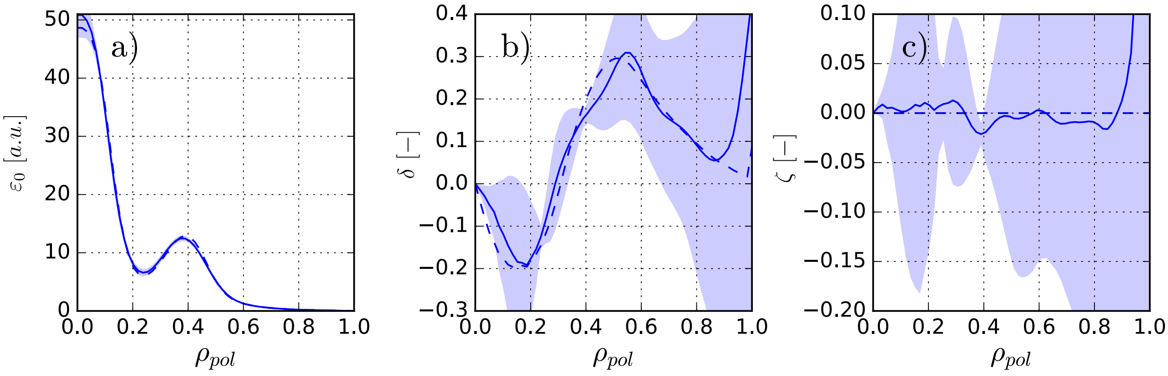

Figure 4.4.: Comparison of prescribed (dashed line) and reconstructed (solid line) asymmetry profiles for a peaked-hollow profile. a) flux surface averaged profiles, b) in-out asymmetry, c) up-down asymmetry. The confidence interval is indicated by a light blue background.

the plasma equilibrium. The uncertainty caused by a mapping on the magnetic equilibrium shifted by ΔR_{mag} is expressed by following approximation

$$\Delta\delta \approx \frac{\partial}{\partial r}\ln(\varepsilon_{\mathrm{SXR}}(1+\delta))\Delta R_{\mathrm{mag}}. \tag{4.15}$$

Due to a steep radiation profile (i.e. $\frac{\partial \varepsilon_{\mathrm{SXR}}}{\partial r} \gg \varepsilon_{\mathrm{SXR}}/R_{\mathrm{mag}}$) a small error in the plasma position can cause a large error in the asymmetry δ. Accurate knowledge of the plasma position is, therefore, essential for a reliable estimate of the poloidal asymmetry. On AUG, multiple magnetic equilibrium codes are available – commonly used are CLISTE [52], the TRANSP equilibrium solver [53] and the Bayesian solver IDE [55, 56]. The most advanced solver is IDE; however, because it is not fully optimized yet, the shape of the magnetic flux surfaces often clearly mismatch the SXR observations. The TRANSP code is constrained by the measured kinetic pressure profile and the modeled pressure profile of the fast particles. And finally, an ordinary run of CLISTE is constrained by the external magnetic measurements only. Comparison between CLISTE and TRANSP is provided in Fig. 4.5a for a high-pressure and in Fig. 4.5b for a low current discharge. In the case of the high-pressure discharge, the CLISTE significantly overestimates the Shafranov shift. On the other hand, for the low current discharge, the discrepancy in the position of the plasma center is marginal. The clear difference can be observed in the spacing between the flux surfaces, which indicates too flat current profile from CLISTE. However, it does not affect the measured asymmetry. Since the differences between the codes are substantial, we will use the TRANSP equilibrium.

In order to examine the discrepancies between the position obtained from the reconstruction of the SXR emissivity and the one calculated by CLISTE, we have compared

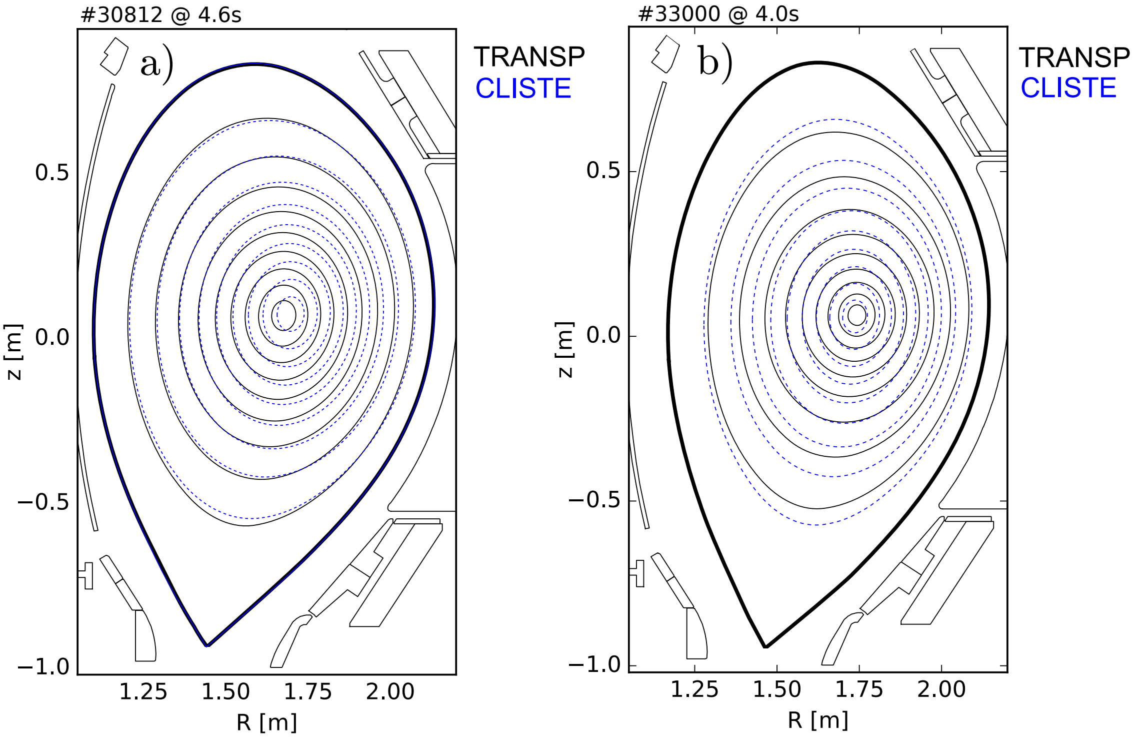

Figure 4.5.: Comparison of the CLISTE flux surfaces constrained by magnetic measurements (dashed) and the TRANSP equilibrium solver constrained by kinetic profiles and the CLISTE separatrix (full line). a) Discharge 30812 with a highly anisotropic population of the fast particles, $I_p = 1\,\mathrm{MA}$ low $q_{95} = 4.4$ b) Elongated discharge 33000 with a peaked current profile, $I_p = 0.6\,\mathrm{MA}$ and high $q_{95} = 7.4$.

the position from a large number of discharges. The histograms, indicating discrepancies in the core, on mid-radius and at the edge of the plasma are depicted in Fig. 4.6. The comparison was evaluated as the difference between the center of mass of reconstructed emissivity in the examined region and the modeled emissivity using plasma shape from CLISTE and the radial profile from the measured SXR radiation. Thus all plasma shaping effects are included, and no further corrections (in contrary to [57]) are necessary. The position of the maximum of each histogram deviates from zero by less than 3 mm. The core radial position is skewed towards the positive values due to the centrifugal asymmetry. Except for this, we can conclude that the discrepancy is between 0.5–1 cm. Moreover, because the kinetic constrained TRANSP equilibrium should be even more accurate, we will use this equilibrium for the further analysis of the asymmetries.

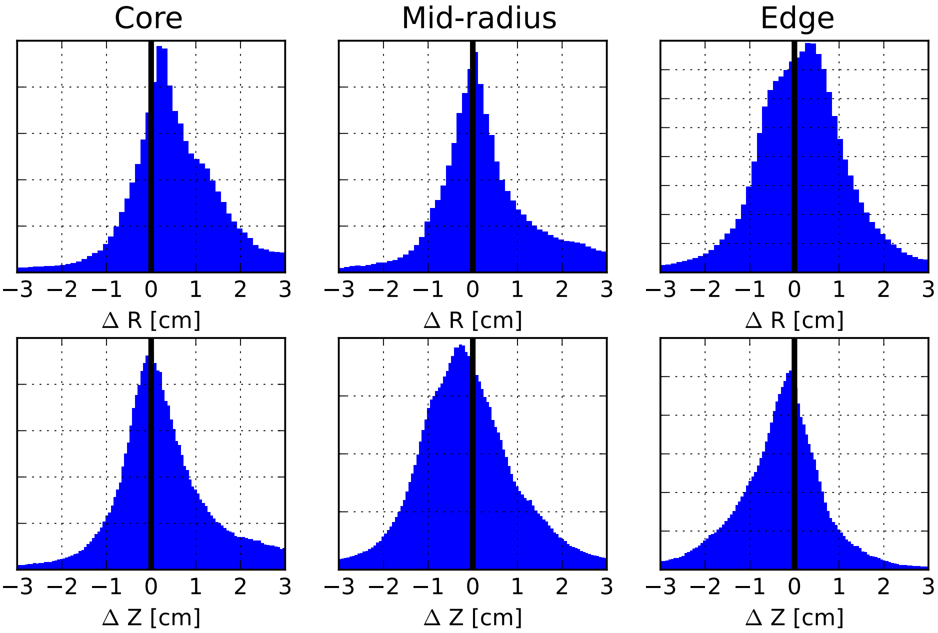

Figure 4.6.: Histograms represent a difference between the plasma position estimated from SXR radiation and the CLISTE equilibrium. The comparison was evaluated the current flat-top phases of 230 H-mode discharges from the campaign 2015/2016.

4.4. Summary

In this chapter, a method was established which allows for the investigation of the 2D tungsten distribution. Since no tomography code, providing a tomographic reconstruction in the required quality, was available in the fusion community, a new tomography tool has been developed. The code originates from M. Odstrčil and J. Mlynář [47], however, almost complete refurbishing was necessary to meet our requirements. New methods for the inversion and choice of the proper regularization level were developed. The new code is fast and stable, such that whole sets of discharges can be studied with minimal human input. Moreover, the high resolution of the inversions enables a reconstruction with a unprecedented level of detail. Due to the steep SXR radiation profiles, the accurate alignment of the cameras and the magnetic equilibrium is crucial for the estimate of the poloidal asymmetries. Small discrepancies can lead to significant errors and a loss of the credibility of the results. Therefore, a careful testing of the tomography code and the chain of the post-processing codes was performed to avoid any systematical bias in the reconstruction.

5. Impurity Transport in Tokamaks

Optimized particle and energy confinement is essential for an economical operation of future fusion reactors, because confinement properties of the plasma are directly related to the final size and cost of the machine. This is also the reason why the experimental and theoretical understanding of transport is a problem of the utmost importance.

In an ideal case, a charged particle follows a straight magnetic field line forever. However, in the real magnetized plasma, the particles are subject to drifts in inhomogeneous magnetic fields, Coulomb collisions with other particles causing the *collisional transport* and microscopic fluctuations due to a coherent behavior of large groups of particles driving the *turbulent transport*. In view of the fluid theory, the collisions cause friction between plasma species. The radial collisional transport that is driven by a friction force perpendicular to the magnetic field and the flux surface is referred as the *classical transport*, while the friction force along the curved magnetic field lines caused by a toroidal geometry leads to the *neoclassical transport*.

The present chapter provides the theoretical background of transport theory, necessary for the later experimental investigations. At first, the collisional and the turbulent transport are discussed, highlighting the mechanisms responsible for the interaction between parallel and radial impurity transport. Section 5.2 reviews the parallel transport theory also providing new models for fast particles driven poloidal asymmetries. At last, the consequences of the impurity asymmetries on the radial transport are discussed in Sec. 5.3.

5.1. Radial Impurity Transport

Because the tokamak plasma is close to the local thermodynamic equilibrium a linear relation between the fluxes of general quantities J_i and the thermodynamic forces X_j pushing the system towards to equilibrium exist. This mechanism is expressed by the first Fick's law as:

$$\mathbf{J} = \mathcal{L}\mathbf{X} \tag{5.1}$$

where $\mathcal{L}$ is referred to as a *transport matrix*. As was pointed out by L. Onsager [58], the coefficients of $\mathcal{L}$ cannot be arbitrary. According to the second thermodynamic law and microscopic reversibility of the equations of motion, $\mathcal{L}$ must be a positive definite matrix. The main goal of transport theory is to provide the coefficients of the transport matrix. Quantities of our interest u_j are first moments of the distribution function, i.e. the densities of all species, momentum, heat, and the thermodynamic forces represented by the gradients of these quantities. Since the matrix $\mathcal{L}$ has nonzero off-diagonal terms, a gradient of a quantity u_j can drive a flux of other quantities. The diagonal terms are called diffusion coefficients, while the off-diagonal terms are referred to as convective velocities or pinch. Let's assume that the flux J_i of i-th quantity u_i, then

$$J_i = \mathcal{L}_{i1}\nabla u_1 + \mathcal{L}_{i2}\nabla u_2 + \ldots \mathcal{L}_{in}\nabla u_n. \tag{5.2}$$

Now, by separation diffusion $D_i \equiv \mathcal{L}_{ii}$ and collecting the off-diagonal contributions to the convection flux $V_i u_i$, the expression is reduced to

$$J_i = -D_i\nabla u_i + V_i u_i \tag{5.3}$$

Combining the flux J_i with the particle conservation, a diffusive-advective type of differential equation called the *transport equation* is obtained.

5.1.1. Impurity Transport Equation

We would like to find an expression for the radial impurity transport in real tokamak geometry based on the formula (5.3). The conservation law for particle density n_Z of an impurity in an ionization stage Z can be expressed in the integral form as

$$\frac{\partial}{\partial t}\int_V n_Z = -\oint_{\partial V} \mathbf{\Gamma} \mathrm{d}\mathbf{S} + \int_V \mathcal{S} \tag{5.4}$$

where V is the investigated volume, $\mathbf{\Gamma}$ is the particle flux density and $\mathcal{S}$ is a sum of all sources and sinks due to ionization, recombination and charge exchange. Specifically, an equation for radial transport, perpendicular to the magnetic flux surfaces is of our interest. As it will be demonstrated in section 5.3.1, parallel transport is significantly faster than radial transport in the plasma core, which is an underlying reason why we can treat radial and parallel transport separately. The derivation of a flux surface average of Eq. (5.4) follows the steps in [59]; however, we will not assume the particle flux density $\mathbf{\Gamma}$, the source term $\mathcal{S}$ and the particle density n_Z to be constant on flux surfaces and a careful analysis of the consequences will be performed.

The flux surfaces will be labeled by the coordinate r defined as

$$r = \sqrt{\frac{V}{2\pi^2 R_0}}, \tag{5.5}$$

derived from the volume of the torus $V(r)$ with the major radius R_0. Such a definition leads to a convenient form of the transport equation, similar to the continuity equation in cylindrical coordinates. If we define a unit vector $\hat{r} \equiv \nabla r / \|\nabla r\|$, normal to the flux surface, pointing outside of the enclosed volume, then the surface integral of the flux density becomes

$$\oint \mathbf{\Gamma} \mathrm{d}\mathbf{S} = \oint \mathbf{\Gamma} \cdot \nabla r \frac{\mathrm{d}S}{\|\nabla r\|}. \tag{5.6}$$

The following relation can be used to express the flux surface average[1] (FSA) of a general scalar quantity $\mathcal{A}$

$$\langle \mathcal{A} \rangle = \frac{1}{V'} \oint \mathcal{A} \frac{\mathrm{d}S}{\|\nabla r\|} \tag{5.7}$$

and

$$\int_{V(r)} \mathcal{A} \mathrm{d}V = \int_0^r V' \langle \mathcal{A} \rangle \mathrm{d}r \tag{5.8}$$

where V' is a derivative of the volume enclosed by a flux surface with respect to the flux coordinate r. The expression for the continuity equation (5.4) becomes

$$\frac{\partial}{\partial t} \int_0^r \mathrm{d}r \langle n_Z \rangle V' = -V' \langle \mathbf{\Gamma} \cdot \nabla r \rangle + \int_0^r \mathrm{d}r V' \langle \mathcal{S} \rangle. \tag{5.9}$$

Differentiating this equation with respect to r and using the definition of $r(V)$ in Eq. (5.5) yields a radial transport equation similar to the form in cylindrical geometry,

$$\frac{\partial \langle n_Z \rangle}{\partial t} = -\frac{1}{r} \frac{\partial}{\partial r} r \langle \mathbf{\Gamma} \cdot \nabla r \rangle + \langle \mathcal{S} \rangle. \tag{5.10}$$

The last step is to evaluate the FSA of the scalar product $\mathbf{\Gamma} \cdot \nabla r$. Starting from

$$\mathbf{\Gamma} \cdot \nabla r = -D(\theta) \|\nabla r\|^2 \frac{\partial n_Z}{\partial r} + v(\theta) \|\nabla r\| n_Z, \tag{5.11}$$

the particle density can be separated into a poloidally dependent and independent part using $\tilde{n}(\theta) = n_Z(\theta) / \langle n_Z \rangle$ and substituting Eq. (5.11) back to Eq. (5.10)

$$\frac{\partial \langle n_Z \rangle}{\partial t} = \frac{1}{r} \frac{\partial}{\partial r} r \left(D^* \frac{\partial \langle n_Z \rangle}{\partial r} - v^* \langle n_Z \rangle \right) + \langle \mathcal{S} \rangle, \tag{5.12}$$

---

[1] The flux surface average of a scalar function Φ is defined as

$$\langle \Phi \rangle = \lim_{\delta \mathcal{V} \to 0} \frac{1}{\delta \mathcal{V}} \int_{\delta \mathcal{V}} \Phi \, dV$$

where $\delta \mathcal{V}$ is the volume confined between two flux surfaces.

where D^* and v^* are FSA transport coefficients weighted by an asymmetry factor $\tilde{n}$

$$D^* = \langle D(\theta) \|\nabla r\|^2 \tilde{n} \rangle \tag{5.13a}$$

$$v^* = \langle v(\theta) \|\nabla r\| \tilde{n} \rangle - \langle D(\theta) \|\nabla r\|^2 \frac{\partial \tilde{n}}{\partial r} \rangle. \tag{5.13b}$$

Since the transport coefficients D_0, v_0 obtained from transport models like NEO [60] or GKW [61] are usually defined with respect to the low field side gradients, a small modification of the previous relations is necessary:

$$D^* = D_0 \tilde{n}_0 \frac{\partial r}{\partial r_m} \tag{5.14a}$$

$$v^* = v_0 \tilde{n}_0 - D_0 \frac{\partial \tilde{n}_0}{\partial r} \frac{\partial r}{\partial r_m}, \tag{5.14b}$$

where $\tilde{n}_0$ is the asymmetry factor $\tilde{n}$ evaluated at the low field side and the minor radius r_m is taken to be half of the width of the flux-surface at the elevation of the flux-surface centroid. For the sake of simplicity, the asterisk will be omitted from now on, and we will always use only the FSA averaged coefficients according to the definitions (5.13) and (5.14).

The source and sink term $\langle \mathcal{S}_Z \rangle$ couples transport of the ionization stage Z with the neighboring stages of the impurity by the following relation

$$\begin{aligned} \langle \mathcal{S}_Z \rangle = &- (n_e S_Z + n_e \alpha_Z + n_0 \alpha_Z^{cx}) n_Z \\ &+ n_e S_{Z-1} n_{Z-1} + (n_e \alpha_{Z+1} + n_0 \alpha_Z^{cx}) n_{Z+1}. \end{aligned} \tag{5.15}$$

S_Z is the impurity ionization rate into the stage Z, α_Z is the recombination coefficient from the ionization stage Z including a contribution from di-electronic and radiative recombination and α_Z^{cx} is the recombination coefficients for charge exchange with neutral atom n_0. By summing Eq. (5.12) for all the ion stages and excluding the neutrals, all terms in $\langle \mathcal{S}_Z \rangle$ will cancel out except for the ionization and recombination between the neutral atom and the single ionized ion. The result is a transport equation for the impurity particle density independent of the charge state. The transport coefficients v and D will be an average of the transport coefficients for each ion stage weighted by the local value of fractional abundances of these stages. A solution of the coupled set of equations (5.15) and (5.12) can be found numerically using a transport code like STRAHL [62].

5.1.2. Classical Transport

In this section, we provide a brief overview of processes driving classical transport. A detailed derivation can be found in [63, 64]. The classical transport theory is based on the Coulomb interaction of individual charged particles in a strongly magnetized plasma. The collisions between particles of the same species do not lead to net radial particle transport since identical particles would only exchange their position. Therefore, in a pure hydrogenic plasma the classical transport would be rather weak, due to a low transfer of momentum between light electrons and roughly 2000 times heavier protons. As soon as impurities are present in the plasma, friction between the bulk ions and impurities become an important drive for collisional transport. In contrast, heat transport is driven mostly by collisions within a single species, because a heat flux between different species α and β, $m_\alpha < m_\beta$ is reduced by a factor $\sqrt{m_\alpha/m_\beta} < 1$.

In the fluid description of plasma, the momentum balance equation can be expressed as [64]:

$$m_\alpha n_\alpha \frac{\mathrm{d}\mathbf{u}_\alpha}{\mathrm{d}t} = e_\alpha n_\alpha(\mathbf{E} + \mathbf{u}_\alpha \times \mathbf{B}) - \nabla p_\alpha + \mathbf{F}_{\alpha\beta}, \tag{5.16}$$

where $\mathbf{E}$ is an electric field, $\mathbf{B}$ a magnetic field, m_α and m_β are masses of both species and $\mathbf{F}_{\alpha\beta}$ is a friction force. For two species α and β with a Maxwellian velocity distribution and equal temperature, the friction force is

$$\mathbf{F}_{\alpha\beta} = m_\alpha n_\alpha \nu_{\alpha\beta}(\mathbf{u}_\beta - \mathbf{u}_\alpha) = m_\beta n_\beta \nu_{\beta\alpha}(\mathbf{u}_\alpha - \mathbf{u}_\beta), \tag{5.17}$$

where $\mathbf{u}$ is the flow velocity and $\nu_{\alpha\beta}$ is the collision frequency between species α and β

$$\nu_{\alpha\beta} = \frac{4\sqrt{2\pi}}{3(4\pi\varepsilon_0)^2} \frac{Z_\alpha^2 Z_\beta^2 e^4 \sqrt{\mu_{\alpha\beta}} \ln \Lambda_{\alpha\beta}}{T^{3/2}} \frac{n_b}{m_\alpha}. \tag{5.18}$$

where $\mu_{\alpha\beta}$ is reduced mass of both species and $\Lambda_{\alpha\beta}$ is the Coulomb logarithm [65]. The friction experienced by the species α from all other species is then the sum of the friction forces $\mathbf{F}_\alpha = \sum_{\alpha\neq\beta} \mathbf{F}_{\alpha\beta}$. The perpendicular fluid velocity is in the zero order determined from Eq. (5.16) by neglecting a friction and time derivative as

$$\mathbf{u}_{\perp,\alpha}^{(0)} = \frac{\mathbf{E} \times \mathbf{B}}{B^2} - \frac{\nabla p_\alpha \times \mathbf{B}}{e Z_\alpha n_\alpha B^2}. \tag{5.19}$$

Since the first term on the right, called $\mathbf{E} \times \mathbf{B}$ drift, is the same for all species, the friction can be caused only by a charge dependent diamagnetic drift proportional to gradient of the pressure p_α. Without friction or up-down asymmetries in the particle density, the zero order flows do not lead to a net radial transport. The friction force driven by the first order flows $\mathbf{u}_\alpha^{(0)}$ and $\mathbf{u}_\beta^{(0)}$ is

$$eZ_\alpha n_\alpha \mathbf{u}_\alpha^{(1)} \times \mathbf{B} = -\mathbf{F}_\alpha \equiv -m_\beta n_\beta \nu_{\beta\alpha}(\mathbf{u}_\alpha^{(0)} - \mathbf{u}_\beta^{(0)}). \tag{5.20}$$

By projecting this equation on the plane perpendicular to $\mathbf{B}$ and substituting the zero order flow $\mathbf{u}_{\perp,\alpha}^{(0)}$ from (5.19) one obtains the classical radial flux for species α driven by friction with species β:

$$\frac{\Gamma_{\perp,\alpha}}{n_\alpha} = D_{CL}^\alpha \nu_{\alpha\beta} \left(-\frac{\nabla n_\alpha}{n_\alpha} + \frac{Z_\alpha}{Z_\beta} \left(\frac{\nabla n_\beta}{n_\beta} - H_{\alpha\beta} \frac{\nabla T}{T} \right) \right), \tag{5.21}$$

where the classical diffusion coefficient D_{CL}^α is expressed by the formula

$$D_{CL}^\alpha = \frac{m_\alpha T \nu_\alpha}{Z_\alpha^2 B^2} = \frac{\rho_\alpha^2}{2} \nu_\alpha.$$

Such a diffusion coefficient corresponds to a random walk process with the mean step size equal to the Larmor radius ρ_α and the mean step frequency ν_α.

The term in Eq. (5.21) proportional to ∇n_α represents the diffusive flux, while the other terms describe the convective part of the flux. The gradient in the temperature usually reduces the inward flux of the particles and this effect is called *temperature screening*. The temperature gradient factor $H_{\alpha\beta}$ is represented by:

$$H_{\alpha\beta} = \frac{3}{2} \frac{m_\alpha}{m_\alpha + m_\beta} - 1 - \frac{Z_\beta}{Z_\alpha} \left(\frac{3}{2} \frac{m_\beta}{m_\alpha + m_\alpha} - 1 \right),$$

$H_{\alpha\beta}$ is roughly equal to one-half for a heavy impurity. The temperature screening is caused by the decrease of the cross-section for Coulomb collisions with temperature.

Classical transport in the cylindrical geometry is independent of the poloidal angle. However, the situation in toroidal geometry is very different. The distance between the flux surfaces on the LFS is shorter than on the HFS, their circumference is larger due to increased R_0, and finally, the Larmor radius is larger on the outboard side, because the magnetic field is lower. All terms favor the radial flux contribution from the LFS side, which is at the mid-radius about a factor of five higher than the inboard contribution.

5.1.3. Neoclassical Transport

The toroidal bending of the magnetic field leads to the additional neoclassical flux. The gradient and curvature of the magnetic fieldlines in the toroidal configuration give rise to the diamagnetic current, causing charge separation, a vertical electric field and the ejection of particles on the outboard side via the $\mathbf{E} \times \mathbf{B}$ drift. However, the charge separation is compensated due to the helical structure of the magnetic fieldlines (see Fig. 1.2), and the parallel Pfirsch-Schlüter (PS) current arises to suppress the charge separation. The parallel component of the friction forces emerged due to the PS flux then gives rise to neoclassical transport. A detail derivation of this theory is available in [66]. In this section, we will summarize only the most relevant parts, in order to discuss the impact of the poloidal asymmetries in the neoclassical transport in Sec. 5.3.2.

First of all, we will discuss the Pfirsch-Schlüter (PS) transport regime, i.e. the case when the mean free path of the ion is much shorter than the circumference of the torus. The perpendicular zero order flow is given by Eq. (5.19). The parallel flow necessary to keep the total divergence free (i.e. $\nabla \cdot \mathbf{u}_\alpha^{(0)} = 0$), is expressed as

$$u_{\alpha||} = -\frac{RB_t}{B}\frac{\mathrm{d}\Phi}{\mathrm{d}\psi} + \frac{K_\alpha(\psi)B}{n_\alpha},$$

where $\boldsymbol{\Phi}(\psi)$ is the electric potential as function of the poloidal magnetic flux ψ and $K_\alpha(\psi)$ is an integration constant determined from the periodicity of $n_\alpha(\theta)$. Since the diamagnetic flow has vertical direction and field lines inclination changes its sign between the inboard and outboard side (see Fig. 5.1 left), also the parallel flow and thus the friction force, causing the radial neoclassical flux, must change its direction (see Fig. 5.1 right). The parallel friction force $R_{\alpha||}$ caused by the PS flow was expressed by [67, 68] in the following form:

$$R_{\alpha||} = \frac{RB_T n_i T_i}{\Omega_i \tau_{i\alpha}}\left(\frac{n_i'}{n_i} - \frac{1}{2}\frac{T_i'}{T_i}\right) + \frac{m_i n_i}{\tau_{i\alpha}}\left(u - \frac{K_\alpha}{n_\alpha}\right)B \tag{5.22}$$

where $\boldsymbol{\Omega}_i$ is an ion cyclotron frequency and $\tau_{i\alpha}$ is the ion impurity collision time

$$\tau_{i\alpha} = \frac{2\sqrt{\pi}}{4\nu_{i\alpha}} \tag{5.23}$$

The particle flux is related to the parallel friction force by the following flux friction relation [64, 66]

$$\langle \boldsymbol{\Gamma}_\alpha \cdot \nabla r \rangle = \frac{\mathrm{d}r}{\mathrm{d}\psi}\frac{RB_T}{Z_\alpha}\left\langle \frac{R_{\alpha||}}{eB} \right\rangle. \tag{5.24}$$

By substituting the friction force (5.22) into this relation and assuming the particle density n_α evenly distributed over the flux surface, one can derive the conventional PS

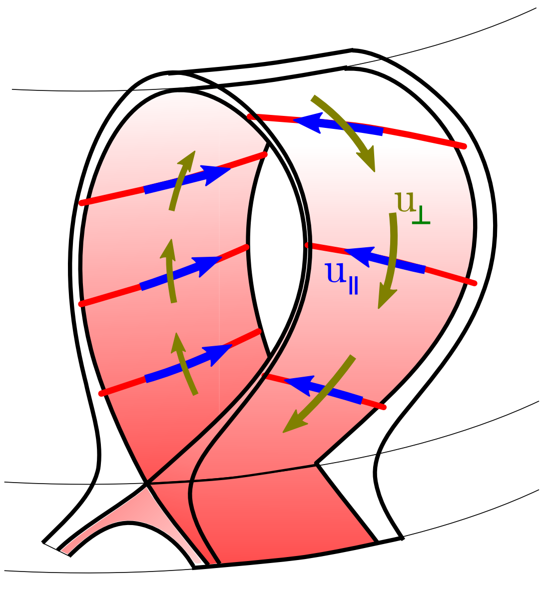

Figure 5.1.: (left) An illustration of the perpendicular diamagnetic flow and the parallel return flows in a plasma. (right) The radial Pfirsch-Schlüter flux of the impurity calculated on the real magnetic equilibrium (courtesy of R. Dux)

transport coefficients

$$D^{PS} = \frac{\langle RB_T \rangle}{(\partial\psi/\partial r)^2} K^{PS} \left(\left\langle \frac{1}{B^2} \right\rangle - \frac{1}{\langle B^2 \rangle} \right) \frac{m_\alpha k T \nu_\alpha}{e^2 Z_\alpha^2} \tag{5.25a}$$

$$v^{PS} = Z_\alpha D^{PS} \left(\frac{n_i'}{n_i} + \frac{H^{PS}}{K_{PS}} \frac{T_i'}{T_i} \right) \tag{5.25b}$$

where the term in (5.25a) before K^{PS} can be expressed as $2(q/B)^2$ in the case of a large aspect ratio, where q is the safety factor[2]. In such case, the neoclassical diffusion coefficients are just enhancing the classical value by a geometrical factor $2q^2$. The explicit expression for the terms K^{PS} and H^{PS} can be found in [66, 69] and depends on the impurity strength parameter $a = n_\alpha Z_\alpha^2 / n_i$ and the normalized ion

---

[2] The safety factor q is defined as the number of toroidal turns, which the field line pass per a single poloidal turn:

$$q = \frac{\Delta\varphi}{2\pi}$$

where $\Delta\varphi$ is the toroidal angle passed by the magnetic field line.

collisionality $\nu_D^* = \nu_D Rq/v_{th}$:

$$K^{PS} = 1 - \frac{0.52a}{0.59 + a + 1.34\nu_D^{*-2}} \tag{5.26a}$$

$$H^{PS} = -\frac{1}{2} + \frac{0.29 + 0.68a}{0.59 + a + 1.34\nu_D^{*-2}}. \tag{5.26b}$$

For the high-Z impurities the impurity strength parameter is usually low and therefore K^{PS} and H^{PS} reduce to 1 and 0.5, similarly to the case of the classical transport.

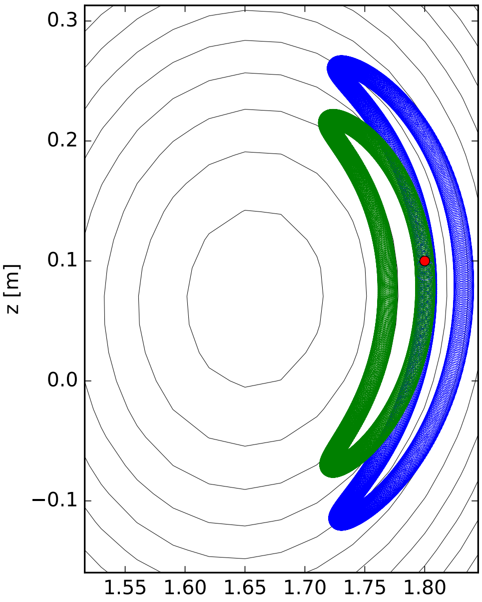

Figure 5.2.: The orbits of 20 keV ions trapped in the gradient of the toroidal magnetic field shown in a poloidal projection. Both particles have the identical starting conditions, but they move in the opposite directions.

When the collisionality of the plasma is sufficiently low, another contribution to the neoclassical flux becomes relevant. The gradient of the toroidal magnetic field causes trapping of particles due to the conservation of the gyromagnetic moment $\mu = mv_\perp^2/2B$, which is an adiabatic invariant. The conservation of μ together with energy conservation gives a condition for trapping:

$$\left.\frac{v_{||}}{v_\perp}\right|_{\mathrm{LFS}} < \sqrt{\frac{B_{\mathrm{HFS}}}{B_{\mathrm{LFS}}} - 1} \tag{5.27}$$

where B_{HFS} and B_{LFS} is the magnetic field on HFS and the LFS of the flux surface. The superposition of the particle movement along the field line and the drift results in orbits with a characteristic banana shape shown in Fig. 5.2. These orbits contribute significantly to neoclassical transport, because the particles can be trapped or de-trapped via collisions. In such a case, the particle changes its position radially by a distance of the order of the banana width w_b. The particle diffusion coefficient will be determined by the banana width and the effective collisional frequency for detrapping ν_b. The additional contribution to neoclassical diffusion is

$$D_{banana} = w_b^2 \nu_b = \frac{q^2}{\varepsilon^{3/2}} D_{CL}. \tag{5.28}$$

where ε is the *local inverse aspect ratio* defined as r/R_0. Since ε is between zero in the core and 1/3 at the edge of the conventional tokamaks and q changes between 1 and 5, the banana transport is significantly higher than the classical and the PS transport when the collisionality is low. Moreover, because the trapped particles remain mostly on the outboard side of the plasma, also the banana radial flux is not constant on the flux surface. The importance of the banana contribution depends on the so-called effective plasma collisionality, defined as

$$\nu_\alpha^* = \frac{qR\nu_\alpha}{\sqrt{T/m_\alpha}\varepsilon^{3/2}}, \tag{5.29}$$

which is used to distinguish the importance of collisions on the particle trajectory. When $\nu_\alpha^* > \varepsilon^{-3/2}$, the banana bouncing time is longer than the collisional time. On the other hand, for $\nu_\alpha^* < 1$ the trapped particles have enough time to pass their orbit before a detrapping occurs.

We can distinguish three collisional regimes: the banana regime for $\nu_\alpha^* < 1$, the plateau regime for $1 < \nu_\alpha^* < \varepsilon^{-3/2}$ and the Pfirsch-Schlüter regime for $\nu_\alpha^* > \varepsilon^{-3/2}$. Because the collisionality dependents on Z_α^2, impurities can be in a different regime than the bulk ions. Such a case is illustrated in the Fig. 5.3, where the deuterium ions are deep in the banana regime, while the boron ions are in the plateau regime in the outer region of the plasma, and finally the tungsten ions exist in-between the PS and the plateau regime. The total radial neoclassical flux decomposed into the individual contributions from the PS, the Banana-Plateau and the classical term is shown in Fig. 5.4. The lowest collisionality is dominated by the contribution from the banana term. When the collisionality is increased, the fraction of particles trapped on the banana trajectories is reduced as well as the banana flow. This region is called the plateau regime because the diffusion coefficient is only weakly dependent on collisionality. Finally, the high collisionality regime is entirely dominated by the PS contribution with a small contribution from the classical flux.

5.1.4. Micro-instabilities and Turbulent Transport

Already in the early days of plasma experiments, a discrepancy between the collisional and the experimentally measured transport was observed [70]. The observed energy losses significantly exceeded the classical predictions, and the surplus flux was referred to as the anomalous transport. Since then, the understanding of plasma physics has considerably improved and the dominant cause for the anomalous flow was identified to be turbulence. The turbulence is due to the collective behavior of the plasma. The particles can organize themselves into larger correlated structures which provide more efficient transport mechanisms than the individual collisions and release faster the free energy of the system. The main effect of the turbulence are the fluctuations

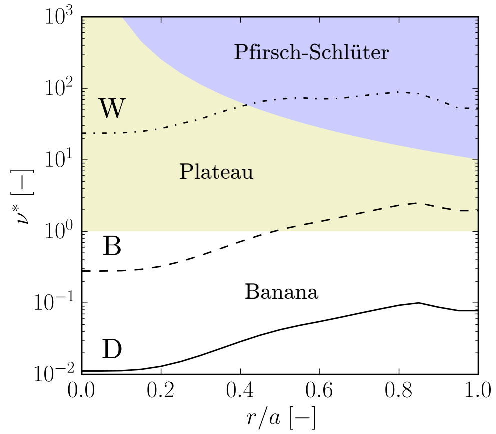

Figure 5.3.: The effective collisionality evaluated for AUG discharge 30812 at 4.6 s. The three lines corresponds to deuterium, boron and tungsten ions, while the shaded regions indicate various collisionality regions.

in the density and temperature correlated with fluctuation in electrostatic potential causing A net $\mathbf{E} \times \mathbf{B}$ drift. The radial turbulent flow $\Gamma_r^{(turb)}$ is then proportional to the perturbation in the particle density $\tilde{n}$ and the electric potential $\tilde{\phi}$

$$\Gamma_r^{(turb)} \propto \langle \tilde{n} \tilde{v}_{E\times B} \rangle_t. \tag{5.30}$$

It is important to note that the fluctuations itself do not lead to net radial transport, but also correlations among them are necessary.

Many types of drift instabilities can arise in tokamak plasmas. However, two linear instabilities dominate a range of the typical plasma parameters relevant for the particle transport. It is the ion temperature gradient mode (ITG) and the trapped electron mode (TEM). The ITG instability is destabilized, if the normalized ion temperature gradient $R/L_{T_i} = -R\nabla \ln T_i$ exceeds a critical gradient. In this case, the ion heat flux shows a strong dependence on the temperature gradient. Such behavior is called stiff transport. Since the gradients on the plasma axis are trivially zero and they are growing towards the plasma edge, the critical gradient is reached at a certain radius. This radius is often, but not always, located close to the magnetic surface where $q(\rho) = 1$.

5.2. Parallel Impurity Transport

Often it is assumed that the transport along the magnetic field lines is fast enough to suppress a variation in the particle density and temperature on the flux surface. This assumption is not valid if a poloidally directed force, acting upon the particles, exists. In

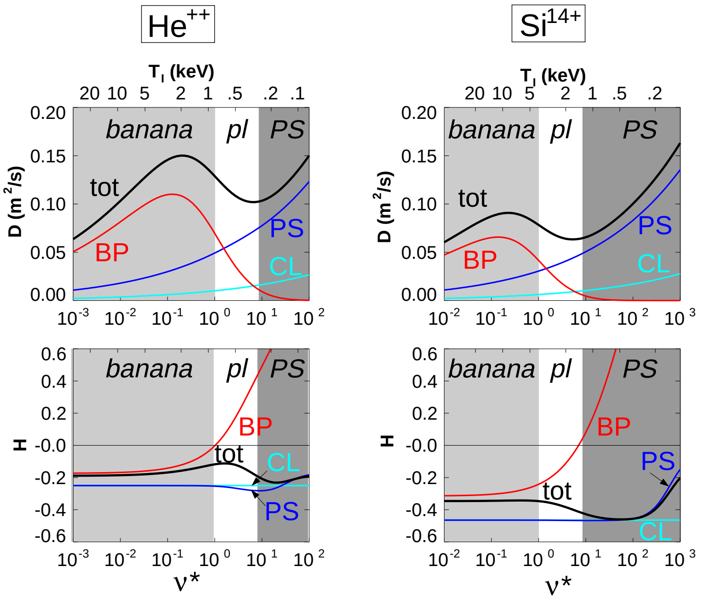

Figure 5.4.: The collisionality scan over the neoclassical diffusion coefficient D (upper row) and the T_i screening coefficient H in the lower row computed in [59] shown versus the ν^* of the impurities ions. The total diffusion coefficient and H factor (tot) are decomposed into classical (CL), Pfirsch-Schlüter (PS), and banana-plateau contribution (BP). The collisionality scan was accomplished by a pure temperature scan with $T_e = T_i$, and thus the collisionality of impurity and bulk ions was changing in the same time. The shaded areas indicate banana, plateau and Pfirsch-Schlüter regime.

such a case, parallel transport causes a fast response of the density towards a poloidally asymmetric profile. The equilibrium profile of a particle species with the Maxwellian distribution is described by the fundamental momentum balance equation derived in [64]:

$$\nabla p_\alpha + \nabla \cdot \pi_\alpha - n_\alpha m_\alpha (\mathbf{u}_\alpha \cdot \nabla)\mathbf{u}_\alpha + Z_\alpha n_\alpha \nabla \Phi + Z_\alpha n_\alpha (\mathbf{u}_\alpha \times \mathbf{B}) = \mathbf{R}_\alpha \tag{5.31}$$

where $\mathbf{u}_\alpha$ is flow velocity of the species α, π_α is the viscosity tensor and $\mathbf{R}_\alpha$ expresses the sum of all friction forces acting on the particle species α. Together with the continuity equation $\nabla \cdot (n_\alpha \mathbf{u}_\alpha) = 0$ and charge quasineutrality $\sum_\alpha n_\alpha Z_\alpha = 0$, Eq. (5.31) provides for each species enough constraints to evaluate the poloidal density profiles of all impurities and the main ions.

The parallel momentum balance equation is obtained by multiplying Eq. (5.31) by $\hat{\mathbf{b}} = \mathbf{B}/||\mathbf{B}||$ and neglecting the viscosity π_α, which is small compared to the other terms:

$$\frac{\nabla_{||} n_\alpha}{n_\alpha} + eZ_\alpha \frac{\nabla_{||}\Phi}{T_\alpha} - \frac{m_\alpha \nabla_{||} u_\alpha^2}{2T_\alpha} = R_{\alpha||}, \tag{5.32}$$

where $\nabla_{||} \equiv \hat{\mathbf{b}} \cdot \nabla$. In the following sections, this equation will be used to derive the asymmetry driven by inertia and by non-Maxwellian species. The comprehensive overview of the theoretical and experimental work done in a parallel impurity transport can be found in Tabs. 2.1 and 2.2 in Ref. [71].

5.2.1. Centrifugal Force

The centrifugal force on impurities was first described in the paper of Hazeltine and Ware [72]. However, their research was focused on the impact of the electrostatic perturbation due to the impurity ion asymmetry on a neoclassical transport of the main ions. An explicit formula for the impurity density profile was derived a decade later in the paper [73] and rediscovered for the experimental community in the seminal paper of J. Wesson [74] another decade later. The latter also provides analytical approximations useful for the comparison with experimental measurements. The first experimental observation of the effects of centrifugal force on the iron ions was accomplished at the ASDEX tokamak by SXR tomography during NBI heated, ELM-free H-mode [75].

The centrifugal force is usually negligible for the bulk ions, but the mass of heavy impurities is one or two orders of magnitude larger than that of deuterium, and thus a significant force is present already for a moderate toroidal rotation velocity of the plasma. The centrifugal force is acting on all particles, however within a flux surfaces the particles more distant from the torus axis will experience a stronger force than the particle closer to the axis. The unevenness in these forces plays a key role in the equilibrium distribution. The derivation of an approximation for the equilibrium impurity profile starts from Eq. (5.32), after neglecting the friction force. In such a case, the parallel momentum balance equation can be integrated over a poloidal angle, and a set of algebraic equations describing the poloidal variation of the density is obtained:

$$\frac{n_\alpha}{n_\alpha^*} = \exp\left[-Z_\alpha \frac{e\tilde{\Phi}}{T_\alpha} + M_\varphi^2 \frac{m_\alpha}{m_p} \frac{(R/R^*)^2 - 1}{T_\alpha/T_e}\right] \qquad \text{for all } \alpha, \tag{5.33}$$

where the asterisk denotes the value on the outer midplane, $M_\varphi = \omega_\varphi R^*/\sqrt{2T_e/m_p}$ is the Mach number of hydrogen ions with angular velocity ω_φ and $\tilde{\Phi} = \Phi - \Phi^*$ represents the perturbation in the electric potential. Equation (5.33) can be further simplified assuming the Boltzmann relation for electrons, the trace heavy impurity z and a small centrifugal asymmetry of the light impurities and bulk ions. The equation for the electric potential obtained from the charge quasineutrality is then

$$\frac{e\tilde{\Phi}}{T_e} \approx \sum_{\alpha \in \text{ions}} Z_\alpha \frac{n_\alpha^*}{n_e^*} \left(eZ_\alpha \frac{e\tilde{\Phi}}{T_i} + m_\alpha M_\varphi^2 \frac{(R/R^*)^2 - 1}{T_\alpha/T_e} \right). \tag{5.34}$$

Substituting the potential to Eq. (5.33), an approximation for $n_z(\theta)$ is obtained:

$$\ln\left(\frac{n_z}{n_z^*}\right) \approx \frac{m_z\omega_\varphi^2}{2T_i}\left(1 - \frac{Z_z m_i}{m_z}\frac{Z_{\text{eff}}T_e}{T_i + Z_{\text{eff}}T_e}\right)(R^2 - R^{*2}), \tag{5.35}$$

where m_i and T_i are the mass and temperature of the bulk ions, while Z_z and m_z are the charge and mass of the impurity. Because of the significant collisional heat exchange between impurity and bulk ions, the ion temperatures are typically equilibrated [76]. Finally, we have assumed $m_\alpha/m_p \approx 2Z_\alpha$ for the light impurities. The approximation for $n_z(\theta)$ is for typical conditions in the AUG tokamak almost accurate and the relative difference with respect to the direct numerical solution of Eq. (5.33) is lower than 0.5 %. The centrifugal asymmetry depends on the ratio of the rotation velocity and ion temperature because it is caused by the balance between the centrifugal and the pressure force. The presence of other impurities or heavier bulk ions reduces the asymmetry due to a larger centrifugal asymmetry of these species and increased perturbation in $\tilde{\mathbf{\Phi}}$ counteracting the centrifugal force.

5.2.2. Electrostatic Force

Variation in the electrostatic potential over a magnetic flux surface has often been ignored, arguing that the passing electrons can move along the field lines to shortcut any possible changes. However, this is not entirely true because of the electron pressure counteracting their complete redistribution. The poloidal variation of the plasma potential predicted by neoclassical theory was investigated in [77] and the following scaling overall collisional regimes was derived:

$$\frac{e\tilde{\mathbf{\Phi}}}{T_e} \sim -\varepsilon\frac{\rho_{i_\theta}}{L_{T_i}}\sin\theta, \tag{5.36}$$

where $\rho_{i_\theta} = \sqrt{2T_i m_i}/eB_\theta$ is the poloidal Larmor radius of the bulk ions. Since the inverse aspect ratio ε and ρ_{i_θ}/L_{T_i} are small in the neoclassical ordering, the term on the right-hand side is negligible. Also, the effect of a parallel electric field generated by a transformer has a negligible impact on the ion distribution, because the typical loop voltage (i.e. the voltage on a loop wire surrounding the torus) is roughly 1 V, while the energy of the core ions is three orders of magnitude higher. However, the situation can be very different in the stellarators as was discussed in [78, 79], where significant poloidal asymmetries in impurity density can arise. The pioneering observation has been made in W7-AS stellarator [80], where a small up-down asymmetry in SXR radiation has been reported.

Nevertheless, processes in tokamaks that can sustain a stationary perturbation in

$\tilde{\Phi}$ exist. The most prominent phenomenon are fast particles produced by auxiliary heating systems. Since these particles are not in thermal equilibrium, their pressure may be significantly anisotropic. This effect was first predicted for the fast ions from the neutral beam injection (NBI) in [81] and for fast ions produced by ion cyclotron range of frequencies (ICRF) heating [82], which were later observed on the JET tokamak [83] and recently on the Alcator C-Mod tokamak [84].

The poloidal distribution of any particle species can be calculated using the constants of motion: energy $\mathcal{E} = mv^2/2$, magnetic moment $\mu = mv_\perp^2/2B$ and canonical angular momentum $\mathcal{P}_\varphi = mRv_\varphi + q\psi$, where ψ is poloidal magnetic flux. The effect of the self-generated variation in the electrostatic potential is neglected and the zero orbit width approximation is applied, i.e. particles will not leave their flux surfaces. The particle density of a species with a distribution function $f(r, \mu, \mathcal{E})$ is then expressed using the radial coordinate r and the magnetic field B representing the poloidal coordinate as

$$n_f(r, B) = 4\pi \int_0^\infty \mathrm{d}\mathcal{E} \int_0^{\mathcal{E}/B} \mathrm{d}\mu \frac{B}{v_{||}} f(r, \mu, \mathcal{E}). \tag{5.37}$$

where $v_{||} = \sqrt{2(\mathcal{E} - \mu B)}$. When the particles are Maxwell distributed or their distribution fulfills $\frac{\partial f}{\partial \mu} = 0$, the particle density will be independent of the poloidal coordinate, which can be verified trivially by integration of Eq. (5.37). Consequently, the number of particles reflected by the magnetic mirror force at a certain value of B is compensated by the slowing down of the passed particles in such way that the number of particles is proportional to the toroidal extend of the volume $\propto R$ and the particle density stays constant.

Because the fast ions are usually light and their temperature is much higher than the self-generated perturbation in the electrostatic potential $e\tilde{\Phi}$, we can neglect the effects of the centrifugal and the electrostatic forces on their poloidal distribution. On the other hand, the potential $\tilde{\Phi}$ is affecting other ions present in the plasma: the higher charge the ion has, the stronger is the effect. Perturbations in the density of a heavy trace impurity can be derived from the Boltzmann distribution for electrons and the quasineutrality relation. Because the perturbation of the electric potential is small, $e\tilde{\Phi}/T_e \ll 1$, the Boltzmann distribution can be expanded

$$\frac{e\tilde{\Phi}}{T_e} = \ln \frac{n_e}{n_e^*} \approx \frac{1}{n_e^*} \left(Z_f(n_f - n_f^*) + \sum_{i \neq f} Z_i(n_i - n_i^*) \right). \tag{5.38}$$

The ion density n_i of the light non-trace impurities and bulk ions is replaced by an expansion of Eq. (5.33) and the following relation for $\tilde{\Phi}$ is obtained

$$e\tilde{\Phi}\left(\frac{1}{T_e}+Z_{\mathrm{eff}}\frac{1}{T_i}\right)=Z_f\frac{1}{n_e^*}\left(n_f-n_f^*\right). \tag{5.39}$$

Now, as an estimate for $\tilde{\Phi}(\theta)$ is available, it can be substituted back to Eq. (5.33) and the poloidal profile of the heavy ion density n_z is expressed as

$$\ln\left(\frac{n_z}{n_z^*}\right)\approx-\frac{n_f-n_f^*}{n_e}\frac{Z_zZ_fT_e}{T_i+Z_{\mathrm{eff}}T_e}. \tag{5.40}$$

When the centrifugal force is present, we can follow the derivation in the previous section to get a final expression for n_z including both, the centrifugal asymmetry and the fast particles effect

$$\begin{aligned}\ln\left(\frac{n_z}{n_z^*}\right)\approx&-\frac{n_f-n_f^*}{n_e}\frac{Z_zZ_fT_e}{T_i+Z_{\mathrm{eff}}T_e}+\\&+\frac{m_z\omega_\varphi^2}{2T_i}\left(1-\frac{Z_zm_i}{m_z}\frac{Z_{\mathrm{eff}}T_e}{T_i+Z_{\mathrm{eff}}T_e}\right)(R^2-R^{*2}).\end{aligned} \tag{5.41}$$

Perturbations in the fast particle fraction $(n_f-n_f^*)/n_e^*$ produced by ICRF and NBI have a typical value of 10^{-2} and therefore the density perturbation for low-Z impurities is negligible. However, heavy impurities like tungsten with a charge $Z_z\sim45$ can show substantial asymmetry. The electric force acts opposite to the centrifugal force, pushing impurities to the high-field side. Since the primary sources of the fast particles in AUG are NBI and ICRF, we will discuss these in more detail.

5.2.3. Fast Particles from ICRF Heating

Ion cyclotron (IC) heating is based on the excitation of fast magnetosonic (compressional Alfvén) waves in the plasma with a frequency Ω. The resonance conditions is given by:

$$\omega-k_{||}v_{||}-n\Omega_{ci}=0\quad\text{for:}\quad n\in\mathbb{N},\Omega_{ci}=\frac{|eZ_i|B}{m_i}. \tag{5.42}$$

where $k_{||}$ is a parallel wave-vector which together with parallel ion velocity $v_{||}$ cause the Doppler shift of the resonance layer. Heating of the bulk ions at the fundamental frequency ($n=1$) is not efficient due to a plasma screening of the left-handed wave component E_+ close to the resonance [85]. A common approach to overcome this situation is called *minority heating* scheme. When a small fraction (i.e. $\lesssim10\%$) of ions with a different mass-to-charge ratio is added, the plasma screening of E_+ is substantially reduced at the IC fundamental frequency of the minority and the power will be efficiently absorbed by this minority ions [86]. The most common minority in the deuterium plasma is hydrogen, which is present as an impurity in the deuterium plasma or deliberately added by a gas puff. The ICRF power can also be absorbed by fast deuterium particles at the second and third harmonic [87] or in the three-ions scheme [88, 89] which is anticipated to be used for the ITER D-T campaign.

The first detailed investigation of the temperature anisotropy and the poloidal electrostatic potential due to ICRF heated species was accomplished in [82]. The temperature anisotropy was calculated using a bounce-averaged Fokker-Planck equation with a bi-Maxwellian distribution for the fast ions. A simple approximation for the poloidal distribution of the ions. It has been found:

$$\frac{n_f}{\langle n_f \rangle} \approx 1 + \left(\frac{\langle T_\perp \rangle}{\langle T_{||} \rangle} - 1 \right) \varepsilon \cos\theta, \tag{5.43}$$

where $\langle T_\perp \rangle$ and $\langle T_{||} \rangle$ are flux surface averaged perpendicular and parallel temperatures of the heated ions. A similar assumption was also used in later experimental investigations at Alcator C-Mod [71]. According to Eq. (5.43), the fast particles are accumulated on the outboard side of the plasma for $T_\perp > T_{||}$ due to increased trapping. Moreover, the asymmetry is proportional to an inverse aspect ratio ε and the anisotropy factor $\eta \equiv T_\perp / T_{||} - 1$. A detailed investigation of bi-Maxwellian species was published in [90], where the complete model for the self-consistent poloidal distribution of density and temperature for all plasma species was proposed.

The assumption of bi-Maxwellian distribution is valid only for heating at the LFS of the flux surface, if the resonance layer is crossed by trajectories of all particles. In contrast to that, part of the trapped particles do not reach the resonance if the resonance magnetic field is smaller than the lowest value on the flux surface, and they are heated only indirectly via collisions with other fast particles. Moreover, the heating causes an increase of the perpendicular momentum of the ions and will lead deeper trapping. Therefore, the particles with the highest temperature anisotropy exit the IC resonance surface and the maximal achievable anisotropy will be strongly reduced.

A better analytic approximation for a fast ion distribution function proposed in [91] has the form

$$f_D(r, \mu, \mathcal{E}) = \left(\frac{m}{2\pi} \right)^{3/2} \frac{n_{\mathrm{ic}}(r)}{T_{\perp,\mathrm{ic}} T_{||,\mathrm{ic}}^{1/2}} \exp\left(-\frac{\mu B_{\mathrm{ic}}}{T_{\perp,\mathrm{ic}}} - \frac{|\mathcal{E} - \mu B_{\mathrm{ic}}|}{T_{||,\mathrm{ic}}} \right) \tag{5.44}$$

where the subscript *ic* indicates quantities evaluated at the IC resonance surface. This distribution function will be later refereed to as *Dendy's model.* The LFS minority distribution estimated from Dendy's model for various ICRF heating positions is shown in Fig. 5.5. Obviously only the LFS heating (a) produces a bi-Maxwellian distribution, while for other cases, the distribution shows a double peaked feature called “rabbit ears”.

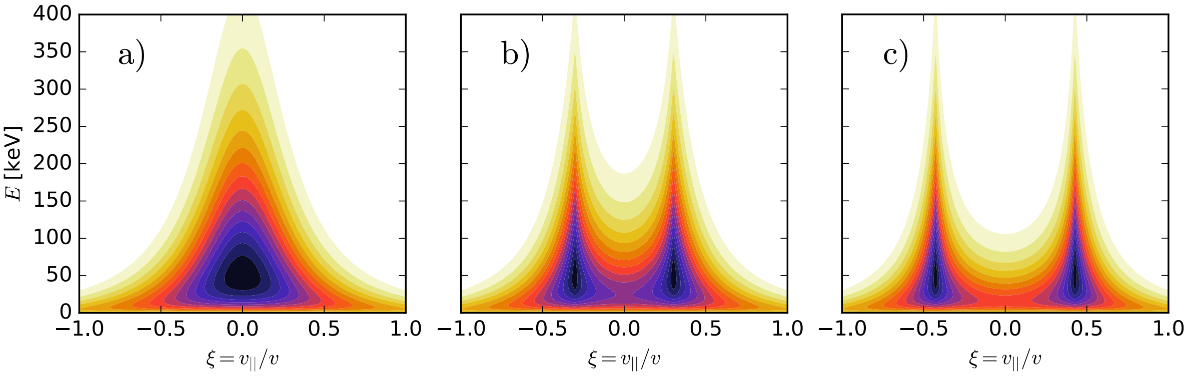

Figure 5.5.: The shape of Dendy’s distribution function (5.44) for $T_{||,\mathrm{ic}} = 10^4\,\mathrm{keV}$ and $T_{\perp,\mathrm{ic}} = 10^5\,\mathrm{keV}$ at $\varepsilon = 0.1$ evaluated at the LFS. The resonance surface is situated at a) the LFS, b) the center and c) the HFS.

A large advantage of the distribution function (5.44) is that their first moments, i.e. density and temperature, can be expressed as analytical formulas [92]:

$$\frac{n(\mathcal{B},\mathcal{T})}{n_{\mathrm{ic}}} = \mathcal{T}_- \left[1 + \left(\frac{\mathcal{T}_+}{\mathcal{T}_-} - 1\right)\sqrt{\frac{\mathcal{T}}{\mathcal{B}}(\mathcal{B}-1)}H(\mathcal{B}-1)\right] \tag{5.45}$$

where $\mathcal{T} = T_{\perp,\mathrm{ic}}/T_{||,\mathrm{ic}}$, $\mathcal{B} = B_{\mathrm{ic}}/B$ and

$$\mathcal{T}_\pm = [\mathcal{B} \pm (\mathcal{B}-1)\mathcal{T}]^{-1} \tag{5.46}$$

and the effective parallel and perpendicular temperatures are [93]

$$\frac{T_{||}}{T_{||,\mathrm{ic}}} = \frac{T_-}{n/n_{\mathrm{ic}}}\left\{1 + H(\mathcal{B}-1)\left[\mathcal{T}(1-\mathcal{B}^{-1})\right]^{3/2}\left(\frac{T_+}{T_-} - 1\right)\right\}$$

$$\frac{T_\perp}{T_{\perp,\mathrm{ic}}} = \frac{n_{\mathrm{ic}}}{n}\left\{T_-^2 + H(\mathcal{B}-1)\sqrt{\mathcal{T}(1-\mathcal{B}^{-1})}\left[\frac{\mathcal{T}_+ - \mathcal{T}_-}{2\mathcal{B}} + \mathcal{T}_+^2 - \mathcal{T}_-^2\right]\right\} \tag{5.47}$$

If the resonance layer is outside of the investigated flux surface, B_{ic} must be replaced by the nearest value of the magnetic field on the flux surface. Note that neither the density nor the temperature of the fast ions are constant on the flux surface, therefore one has to be careful, where these quantities are evaluated when the results of the fast particles modeling are interpreted. The profiles in the TORIC-FFPMOD code [94], which is part of the TRANSP suite of codes [95], are stored as flux surface averaged values, while the output from TORIC-SSFPQL [96] is evaluated at the LFS of the flux surface. The actual value of $\mathcal{T}$ at resonance, required to evaluate the density profile, must be thus found by a numerical inversion of the Eq. (5.47). The disadvantage of the Dendy's model is that it does not converge to the Maxwell distribution for $T_\perp = T_{||}$ and therefore it can be applied only to the fast particles fulfilling $T_\perp \gg T_{||}$.

5.2.4. Fast Particles from Neutral Beam Injection

The effect of the fast NBI ions on the poloidal electric field was first investigated in the theoretical paper [81]. However, since then, no progress has been made on the theoretical and experimental sides of this problem. The experimental verification of this phenomenon is challenging, due to the significant centrifugal asymmetry which results from the momentum input by the tangential NBI, while a small poloidal variation in the density of the fast passing ions from NBI is induced. The proper measurement, therefore, requires a perpendicular beam injection, a balanced beam injection or an excellent measurement of the asymmetry and the accurate model for the poloidal distribution of the high-Z ions. The first two options are not available in the AUG tokamak, and therefore we have to utilize the third one .

The fast particles distribution from a basic model [97] for NBI heating at AUG is depicted in Fig. 5.6a. The positions of the peaks are given by the injection energy of the beam (i.e. 59 keV for the beam box 1 and 91 keV for the beam box 2) and the maximum in the pitch $\xi \equiv v_{||}/v$ depends on the cosine of the angle between the beam and the magnetic field, where the injected neutrals were ionized. Since the poloidal asymmetry of the fast ions is independent of their energy, we will marginalize the distribution over E and study only the ξ dependence. The LFS fast particles distribution function can be approximated by the simple analytical function

$$f^*_{\mathrm{NBI}}(\xi) \propto \exp\left(-|\xi - \xi_0|/w\right) \tag{5.48}$$

where ξ_0 is determined by the position of the injection peak and width w is roughly 0.3 for a 59 keV beam. The poloidal profile of the fast particles density can be evaluated from Eq. (5.37) after a coordinate transformation

$$n_f(B) = \int_{-1}^{1} \mathrm{d}\xi\ f_{\mathrm{NBI}}(\xi^*(\xi, B)) \tag{5.49}$$

and the LFS value of the pitch ξ is calculated from the conservation of E and μ:

$$\xi^*(\xi, B) = \mathrm{sgn}(\xi)\sqrt{1 - \frac{B^*}{B}\left(1-\xi^2\right)}. \tag{5.50}$$

The comparison between the approximation in Eq. (5.48) and the analytical distribution function is shown in Fig. 5.6b and the corresponding poloidal profile from Eq. (5.49) in Fig. 5.6c. In the limit of the entirely tangential beam injection, when all NBI particles are passing (i.e. $|\xi_0| \simeq 1$) the fast particle density is given by

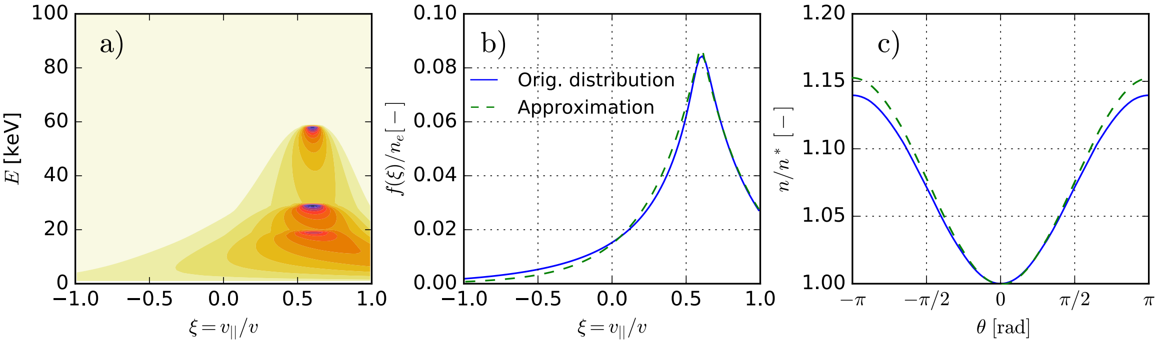

Figure 5.6.: a) Distribution function of the fast particles from NBI obtained from the analytical solution of the Fokker-Planck equation [97], neglecting finite Larmor radius effects. Three injections points for $E_0 = 59\,\mathrm{keV}$, $E_1 = E_0/2$ and $E_2 = E_0/3$ at $\xi_0 = 0.6$ are clearly distinguishable. b) the distribution function marginalized over the energy, where the full line denotes the original distribution, while the dashed line is the approximation in Eq. (5.48) c) the fast particles distribution at $r/a = 0.15$, the dashed line corresponds again to the approximation.

$$\frac{n}{n^*} = \frac{R^*}{R}, \tag{5.51}$$

because the number of fast particles on the flux surface is constant and the volume is proportional to R_0. Therefore the density varies as $\sim 1/R$. The radial profile of the fast particle density is provided by modeling codes, like NUBEAM [98], which is part of TRANSP. NUBEAM can also provide the complete distribution function for a few selected time-points.

5.2.5. Other Sources of Fast Particles

In the study [82], and references herein it was predicted that supra-thermal electrons produced via the electron cyclotron heating (ECRH) should drive a significant perturbation in the electrostatic potential due to trapping, similarly to the ICRF ions. However, the situation is very different. The heating of electrons in resonance with electron cyclotron wave slightly increases their mass by the relativistic effect and their resonance position is thus shifted towards the HFS, out of the heating position. Therefore, the ECRH is affecting almost exclusively the thermal electrons. This effect, together with high collisional momentum exchange between electrons, causes that the fraction of the fast electrons is lower than 10^{-4}, as is shown in Fig. 5.7.

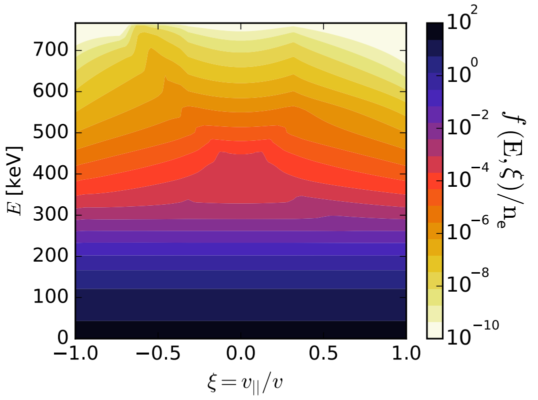

Figure 5.7.: Distribution functions of the electrons heated by ECRH evaluated by RELAX code [99] for ASDEX Upgrade discharge 33697 at 1.68 s and $\rho_\theta = 0.2$. (courtesy of S. Denk)

5.3. Impact of Asymmetries on Radial Transport

In the previous sections, the background for the description of perpendicular and parallel transport of the impurities was explained. In this section, we will focus on the mutual influence between those two effects and the consequences for the radial transport. First, the assumption, under which parallel and perpendicular transport can be treated separately, is discussed. Afterward, the impact of the poloidal transport on the neoclassical and turbulent fluxes will be investigated.

5.3.1. Decoupling of Parallel and Radial Transport

The necessary condition for the separation of the parallel and perpendicular impurity transport is given by the ratio of typical timescales denoted as $\tau_{z,||}$ and $\tau_{z,\perp}$. If the condition $\tau_{z,||} \ll \tau_{z,\perp}$ is fulfilled, we can safely assume immediate redistribution of the impurity on the flux surface and the radial transport will act on the stationary, yet still asymmetric profile. If the assumption is not valid, the localized impurity sources or density perturbations will not be fully redistributed on the flux surface before spreading radially. Additionally, the stationary parallel impurity distribution can be affected by the radial flux.

Since the high-Z impurities are highly collisional, they have a short mean free path and the parallel transport is thus dominantly diffusive with $D_{z,||} = v_{z,th}^2 \tau_{z,||}$. The parallel relaxation time $\tau_{z,||}$ is obtained by solving the diffusion equation with a periodic boundary condition as

$$\tau_{z,||} = \frac{1}{\tau_{iz}} \left(\frac{qR_0}{v_{z,th}} \right)^2 \tag{5.52}$$

Perpendicular transport is often dominated by the anomalous contribution. The experimentally measured time, which the impurity perturbation requires to propagate from the edge to the core, is on AUG about 10 ms. The condition $\tau_{z,||} \ll \tau_{z,\perp}$ is well fulfilled in the plasma core, where is $\tau_{z,||} \approx 10\,\mu$s. However, due to the high mass of tungsten and the thus low thermal velocity, the poloidal redistribution at the plasma edge can be rather slow, between 1–10 ms. Therefore, the impurity perturbation can already reach the plasma core, while it is still not yet poloidally equilibrated at the edge. This effect should be taken into account when impurity transport in the plasma pedestal is investigated, while radial transport in the core can be safely considered as a 1D problem.

5.3.2. Modified Neoclassical Transport

One of the limitations of the standard neoclassical theory is the assumption of approximately constant particle density over the magnetic flux surface. This condition is very well fulfilled by the bulk ions and the electrons, but can easily fail for heavy impurities. This weakness was recognized already in early times of plasma research [73, 100–102], however, due to the lack of experimental measurements, the asymmetries were neglected in the neoclassical transport codes, until recently.

The theoretical investigations were focused on the impurities deep in the Pfirsch-Schlüter regime and the collisionless main-ion regime. The most complete description is derived in the recent paper of C. Angioni and P. Helander [68], where a formula for the neoclassical impurity flux in presence of an arbitrary asymmetry was found. The change in the flux is described by geometry factors modifying K^{PS} and H^{PS} from the definition (5.26) in the following way:

$$\frac{\tilde{K}^{PS}}{K^{PS}} = \frac{1}{2\varepsilon^2} \left(\left\langle \frac{\tilde{n}}{b^2} \right\rangle - \left\langle \frac{b^2}{\tilde{n}} \right\rangle^{-1} \right) \tag{5.53a}$$

$$\frac{\tilde{H}^{PS}}{H^{PS}} = \frac{\tilde{K}^{PS}}{K^{PS}} - \frac{1}{3}\frac{f_c}{\varepsilon^2} \left(1 - \left\langle \frac{b^2}{\tilde{n}} \right\rangle \right), \tag{5.53b}$$

where $\tilde{n} = n_z/\langle n_z \rangle$, $b^2 = B^2/\langle B^2 \rangle$ and f_c denotes the effective fraction of circulating (passing) main ions. In the limit of a large aspect ratio and weakly varying trace impurity density, we take

$$\tilde{n} = 1 + \delta \cos\theta + \zeta \sin\theta \tag{5.54}$$

where the parameters δ and ζ describe out-in and up-down asymmetries, respectively. The approximations for the factors in Eq. (5.53) was derived in [68]

$$\frac{\tilde{K}^{PS}}{K^{PS}} = \left(1 + \frac{\delta}{2\varepsilon}\right)^2 + \frac{\zeta^2}{\varepsilon^2} \tag{5.55a}$$

$$\frac{\tilde{H}^{PS}}{H^{PS}} = \frac{\tilde{K}^{PS}}{K^{PS}} - \frac{\sqrt{2\varepsilon}}{3}\left(\frac{\delta}{\varepsilon} + \frac{\delta^2 + \zeta^2}{2\varepsilon^2}\right). \tag{5.55b}$$

The geometric correction in the Eq. (5.53a) was provided already in the paper of T. Fülop [103], and the approximation Eq. (5.55a) is consistent with the dependence estimated in Ref. [104, 105] for the centrifugal asymmetry.

When the in-out poloidal asymmetry is small, the neoclassical flux is enhanced by a factor $1 + \delta/\varepsilon$. Therefore, outboard impurity accumulation increases the magnitude of transport, while the inboard accumulation reduces transport, as one could also expect from the Fig. 5.1 illustrating the PS flow pattern. If the inboard asymmetry is increased to the level when $n \sim b^2$ (i.e. $\delta/\varepsilon \approx -2$), the inboard and outboard flows will cancel and the net neoclassical flow will be zero. An additional increase of the inboard asymmetry enhances the flow but the sign of the second term in Eq. (5.53b) is changed and the T_i screening is reduced. On the contrary, during a very strong poloidal localization, the enhancement of the PS flow by a factor $(2\varepsilon)^{-1}$ should take place. Such an asymmetry can be observed during cooling events due to intensive W radiation when a sudden increase in the tungsten Mach number up to 10 were measured.

However, these formulas were derived for the impurities deep in the PS regime and bulk ions in the banana regime and as was shown in Fig. 5.3, such an assumption is usually not valid for the core of the AUG tokamak. Therefore, the modeling with the NEO code will be performed in section 8.3, in order to verify this approximation. The neoclassical drift kinetic code NEO includes comprehensive treatments of the poloidal asymmetries valid independently of the collisionality regime [106]. It provides a first-principle calculation of the transport coefficients directly from the solution of the multi-species drift kinetic equation in the real tokamak geometry.

5.3.3. Magnetic Drift Pinch

In the previous section, we have assumed only the ion-impurity friction driven neoclassical flow. The particle drifts described by Eq. (1.3) were ignored because the radial drifts of the particles above the midplane were exactly canceled by their drifts below the midplane. However, when some process breaks the up/down symmetry, more particles will drift up than down (or vice versa), and the net radial particle flux will occur. The local radial guiding center flux in the absence of strong poloidal electric fields is given by

$$\Gamma_\alpha^r(\theta) = \int (\mathbf{v}_\perp \cdot \nabla r) f_\alpha \mathrm{d}^3 v = \frac{m_\alpha \mathbf{B} \times \nabla B \cdot \nabla r}{Z_\alpha e B^3} \int \left(\frac{v_\perp^2}{2} + v_{||}^2 \right) f_\alpha \mathrm{d}^3 v \tag{5.56}$$

Assuming the Maxwellian distribution f_α, a particle density can described by (5.54) and computing the flux surface average, we will obtain

$$\frac{R\Gamma_\alpha^r}{\langle n_\alpha \rangle} \approx -\frac{T_i(1 + m_\alpha M_\varphi^2)}{eZ_\alpha B_0} \zeta. \tag{5.57}$$

The sign of the right hand side depends on the orientation of the magnetic field and a negative value is typical for the AUG configuration with downward ion drift direction. The particle flux in Eq. (5.57) causes substantial outward flow if the particles are accumulated on the bottom of the flux surfaces. This flow is two orders of magnitude larger than the enhancement of the neoclassical PS flow due to the in/out asymmetry [107].

5.3.4. Asymmetry Enhanced Turbulent Transport

The impact of the poloidal asymmetries on turbulent transport has started to be investigated recently in the work of F. Casson [108] and T. Fülop [67]. The turbulence modes are localized essentially in the outboard part of the plasma, as is illustrated in the Fig. 5.8. The fast rotation has two main consequences. In a frame co-moving with the plasma appears the Coriolis and centrifugal forces causing additional drifts. Moreover, the particle trapping due to the inertial forces causes a poloidally asymmetric particle density, which leads to the development of a weak perturbation in the background poloidal electric field, causing an additional $E_\theta \times B_\varphi$ drift. The latter effect also plays a role for the electrostatic force generated by the fast particles.

The gyrokinetic particle flux is usually decomposed as

$$\frac{R\Gamma_z^{\mathrm{turb}}}{\langle n_z \rangle} = D_z^{\mathrm{turb}} \left(\frac{R}{L_{n_z}} + C_T \frac{R}{L_T} + C_u u' + C_p \right), \tag{5.58}$$

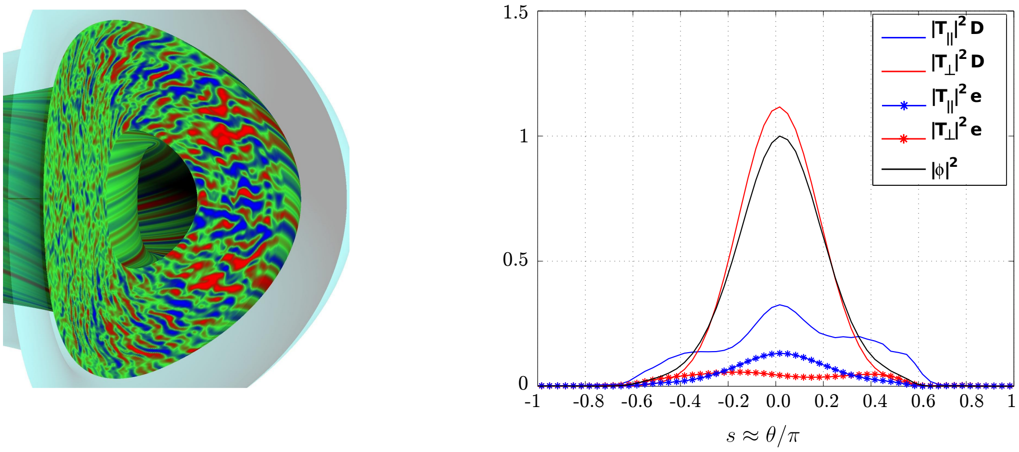

Figure 5.8.: Turbulent transport is driven by interchange modes localized in the "bad curvature" region of the plasma, i.e. on the low field side. On the left is depicted a poloidal cut through a GYRO simulation [109], illustrating a higher magnitude of the fluctuations in the outboard region. On the right are shown the dominant eigen-vectors of the quasilinear solver GKW for various quantities. The highest magnitude of the mode is localized on the LFS (courtesy of C. Angioni).

where the coefficients D_z^{turb}, C_T, C_u and C_p represent diffusion, thermo-diffusion, roto-diffusion and a pinch, while $R/\tilde{L}_{n_z}$ is a generalized logarithmic density gradient of the impurity, which includes the rotation effects derived in [110]. If the background plasma is only weakly effected by the asymmetry and the heavy ions are present in the trace concentration, the magnitude of the turbulent flux scales as

$$R\Gamma_z^{\text{turb}} \propto \int \mathrm{d}\theta n_z(\theta)|\phi|^2 / \int \mathrm{d}\theta|\phi|^2, \tag{5.59}$$

which describes a weighted integration over the mode envelope $|\phi(\theta)|^2$ with the asymmetric density profile n_z. The mode amplitude $|\phi|^2$, evaluated for a real tokamak geometry is plotted on the right of Fig. 5.8. Since the turbulent fluctuations are strongly localized on the outboard side of the plasma, a further approximation of (5.59) is feasible:

$$\frac{R\Gamma_z^{\text{turb}}}{\langle n_z\rangle} \propto \frac{n_z^*}{\langle n_z\rangle} \approx 1+\delta. \tag{5.60}$$

Most of this variation in the particle flux may be described by a correction of D_z^{turb}. The other terms in the expression (5.58) can still play a role, when a stationary, impurity density scale length L_z^0 is evaluated. Such an investigation was performed by Moradi and Mollen [111, 112]. The poloidal impurity density profile in these studies was described as

$$\frac{n_z(\theta)}{n_z(\theta_0)} = \left[\cos^2(\theta - \theta_0)\right]^N , \tag{5.61}$$

where N is the asymmetry scale factor and θ_0 define the position of the density maximum. The density profile for various values of N was evaluated in Fig. 5.9a and the corresponding change of L_z^0 is depicted in Fig. 5.9b. For $\theta_0 = 0$, impurities accumulate on the outboard side and L_z^0 increase weakly with N. On the other hand, for $\theta_0 = \pi$, an inboard accumulation of the impurities is assumed, the scale length L_z^0 decrease with N and the impurity profile becomes flatter, which is a desired result for a fusion reactor. However, the effect of the inboard asymmetry ($\theta_0 = \pi$) is strongly exaggerated, mainly due to the unrealistic poloidal profile of the impurity density used in these studies (Fig. 5.9a) and an extensive range of the parameter N which was considered. The poloidal density profile described by the Eq. (5.61) is close to zero over a large poloidal extent of the outboard region already for small values of N. Because this region corresponds to the primary localization of the turbulent flux, such a profile would cause a significant reduction of the impurity turbulent flux and a change in the normalized gradient. Moreover, the largest observed inboard accumulation on AUG corresponds to $N \sim 0.2$. The real change in the normalized density gradient evaluated in the experimental conditions at Alcator C-Mod tokamak [113] is far below the experimental uncertainty with a negligible impact on the final impurity density profile.

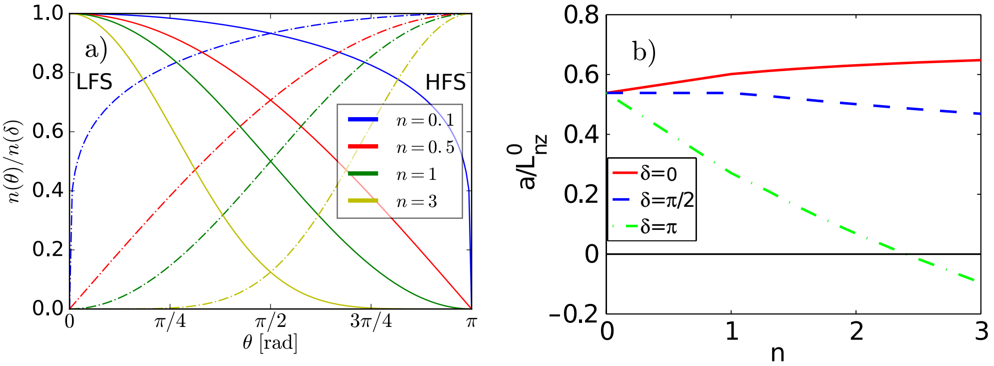

Figure 5.9.: a) Impurity density profiles, which were obtained by evaluation of Eq. (5.61) for various N factors. The full lines represent an outboard asymmetry (i.e. $\theta_0 = 0$) and dashed-dotted lines stays for an inboard asymmetry ($\theta_0 = \pi$). b) Zero flux impurity density scale length a/L_z^0 calculated from a flux surface averaged density profile [111]. The scale length a/L_z^0 was evaluated for various levels of the asymmetry factor n and for a LFS, up/down and HFS asymmetry.

5.4. Conclusions

In this chapter, an overview of the parallel transport theory was presented. The most important forces affecting the parallel force balance in the plasma core represent the electrostatic and the centrifugal force. Both can lead to a significant variation of the impurity density on the flux surfaces. A new model for the asymmetry of fast NBI ions and a better approximation for the solution of the parallel force balance equation was derived in this thesis (see Fig. 5.6). Further, recent progress in the theoretical understanding and the experimental validation of the parallel transport theory has motivated a significant effort in improving our knowledge about the radial transport of high-Z impurities. A major step in that development was the extension of the neoclassical theory, including an arbitrary poloidal asymmetry in the impurity density. This allowed for the identification of the neoclassical effects on radial transport due to a poloidal asymmetry.

However, a detailed experimental verification of these effects is still missing. Asymmetries caused by fast NBI ions have not been observed, and only a very few pioneer studies about ICRF driven asymmetries have been published recently. Also, their effect on radial transport is not experimentally validated. The only experiments available are comparing an experimentally measured stationary impurity density profile with the modeling based on the NEO and GKW codes [114–116]. However, if some part of the impurity transport is not well understood, such measurements can lead to erroneous conclusions. The goal of this thesis is to carefully verify these predictions and identify missing pieces required to explain the dynamics of tungsten transport in a tokamak.

6. Neutral Beam Driven Poloidal Asymmetries

The large torque input from the tangential NBI on AUG leads inevitably to the fast rotation rotation and the centrifugal force, which was reported from many tokamaks with external momentum input from NBI like the former ASDEX [75], AUG [117] or JET [118–120]. Moreover, the centrifugal asymmetry driven by an intrinsic rotation was also reported from the Alcator C-Mod tokamak [121]. However, except for the last study, only a basic scaling of the asymmetry was confirmed, without comparison with a complete model as described by Eq. 5.35.

In this chapter, the poloidal asymmetry in the dominantly NBI heated discharges will be investigated. A thorough understanding of the NBI heated discharges is imperative for the analysis of more complex scenarios, where also other heating sources are present. The objective is to test the validity of the model Eq. (5.35) for the plasma with a fast toroidal rotation and examine an influence of the fast NBI ions described by the Eq. (5.35).

6.1. Centrifugal Asymmetry

Although the centrifugal asymmetry is regularly present during NBI heating, most of the discharges are not suitable for a detailed analysis due to a significant uncertainty in the measured asymmetry and the modeling. Moreover, if any imperfection in the model of centrifugal force exists, we would expect the difference to be observable when the centrifugal force reaches largest values. Such conditions are well fulfilled by discharges with a reduced magnetic shear such as discharge #30937, causing a significant confinement improvement.

6.1.1. Properties of the Plasma Discharge

The discharge #30937 was selected for further analysis due to its enormous poloidal asymmetry, excellent quality of the SXR reconstruction and well measured kinetic profiles for modeling. Off-axis electron cyclotron current drive and early heating[1]

---

[1] The early heating is a plasma scenario when the NBI is started before the plasma current flattop.

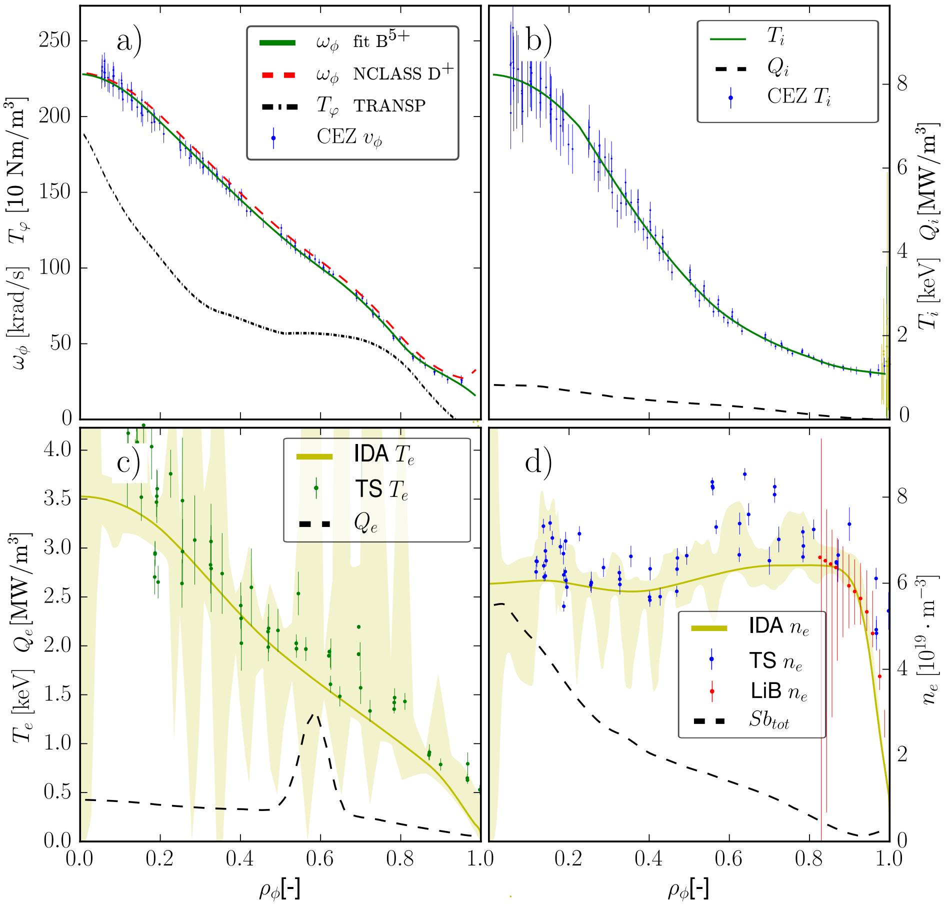

Figure 6.1.: The kinetic profiles for #30937 at 1.53 s a) The full line represents the angular velocity of boron, the red dashed line is a neoclassical corrected velocity of the bulk ions and the black dashed line represents the torque density [30 Nm/m^3] modeled by TRANSP b) The ion temperature is presented and the black dashed line indicates the ion heating profile Q_i [MW/m^3] c) The electron temperature from Thompson scattering with a spline fit and shaded confidence region obtained from IDA and electron heating profile Q_e [MW/m^3] from TRANSP is shown d) The electron density obtained by IDA from the combination of Thompson scattering , DCN and lithium beam is presented along with the neutral particle source term $S_{b,tot}$ from TRANSP.

resulted in an elevated q-profile with a central value of $q_0 \approx 1.5$, negative magnetic shear at $\rho_{\mathrm{tor}} = 0.2$ and consequently significantly reduced turbulent transport. The plasma current has reached a flattop value of 1.0 MA at 1.3 s while the edge safety factor was gradually decreasing to $q_{95} = 3.8$. The auxiliary heating was provided by 7.5 MW of NBI and 1.4 MW of the off-axis ECRH at $\rho_{\mathrm{tor}} = 0.6$. The discharge has not reached the stationary phase because it disrupted at 1.59 s. Shortly before the disruption, the confinement factor calculated using the ITERH98-P(y,2) scaling [122] exceed the value of $H_{98} = 1.3$ when also the poloidal asymmetry was maximal. The kinetic profiles, i.e. the plasma temperature, density, and rotation are displayed in Fig. 6.1 for $t = 1.53\,\mathrm{s}$. The core electron temperature was $T_e = 4\,\mathrm{keV}$, while the ion temperature has reached an unusually high value of 8 keV. As a consequence of the L-H transition happening earlier, the electron density profile is slightly hollow, with an average value about $6 \cdot 10^{19}\,\mathrm{m}^{-3}$. Due to the moderate electron density, excellent confinement and large momentum input from three NBI sources, an exceptionally high core toroidal velocity of $v_\varphi = 420\,\mathrm{km/s}$ was achieved. Consequently, extraordinary values of the Mach number were observed, with the maximum of 0.5 in the plasma core, decreasing slightly to 0.3 towards the pedestal top. The enormous centrifugal force caused that the tungsten were accumulated almost exclusively on the outboard side of the plasma. The perpendicular transport time $\tau_\perp$ is ∼10 ms, assuming an edge transport coefficient of $D \approx 1\,\mathrm{m}^2/\mathrm{s}$ and a characteristic size of the W radiation feature of 10 cm. The parallel transport time $\tau_{||}$ was estimated at the edge using Eq. (5.52) to $\tau_{||} \approx 0.3\,\mathrm{ms}$. The difference between these two timescales is sufficient to enable separate analysis of the parallel and perpendicular transport.

The SXR radiation profile is depicted in Fig. 6.2. The tomographic reconstruction was obtained using the brightness from all SXR cameras (see Fig. 3.1b) except the core H2 head, which had a broken biasing connector and the pair of side cameras I1, I3 with lower thickness of the Be filter. The cameras F, G, K, I and M show rather small differences from the back-projected brightness. On the other hand, a discrepancy can be observed in the J and L camera. The difference in the J camera was most probably caused by a small inaccuracy in the focal length of the camera and the discrepancy in the L camera should be due to imperfections in the 3D model of the heat shield which is partially limiting the field of view of this camera. However, because the most relevant vertical cameras for the measurement of in-out asymmetries, i.e. F, G and K, are fitted almost exactly, a reasonable accuracy of the measured centrifugal asymmetry can be expected.

The tomographic inversion is shown in the right part of Fig. 6.2. The radiation profile is hollow with a significant peak on the right side that is caused by tungsten radiation. The outboard side localization can be seen on the bolometers as well, however, because only two core cameras are available, the credibility and precision of the reconstruction are significantly lower. The hollow radiation profile is caused by ion temperature screening and hollow ion density profile, which has produced the outward particle drift (see Eq. (5.25)). The outboard side localization of the tungsten is a direct consequence of the large centrifugal force affecting the tungsten ions.

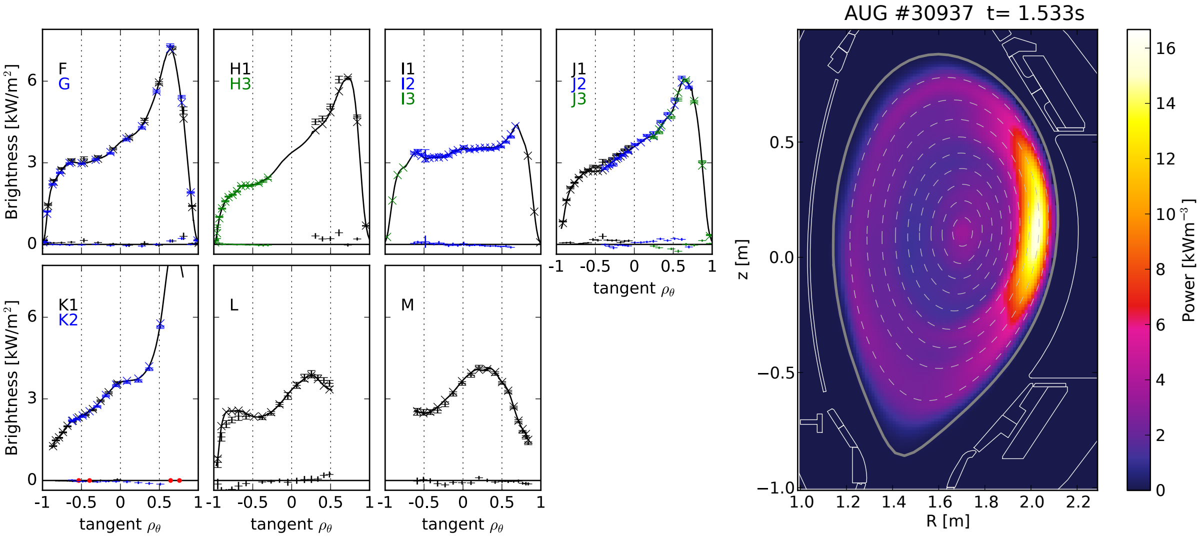

Figure 6.2.: (left) The SXR brightnesses measured in the discharge #30937 at 1.533 s averaged over 0.6 ms. The measured brightnesses are shown by horizontal crosses with error bars indicating the estimated uncertainty along with back-projected values from the tomographic reconstruction (diagonal crosses), cuts through projection space averaged over the width of the VOS (smooth black line), and crosses close to the zero line indicating residua between measurements and back-projections. (right) The tomography of the SXR radiation profile evaluated at a resolution of 100×150 px with residuum $\chi^2/m = 2.6$ and a regularization level of $q_\lambda = 52\,\%$ estimated by the GCV method indicating an excellent quality of the inversion.

6.1.2. Model of the Centrifugal Force

The poloidal asymmetry of the SXR radiation has been evaluated based on the centrifugal force model (see Sec. 5.2.1) for all ion species, i.e. the tungsten ions, light impurities and bulk ions. Additionally, a correction for the neoclassical friction forces was included into our model, following the approach of T. Fülöp [103] further elaborated by M. Reinke [71]. The friction forces can be usually neglected in the plasma core. However, the high Mach number in the investigated discharge should cause a significant enhancement. The consequence of the friction forces is a reduced in-out and increased up-down asymmetry for approximately $\rho_{\mathrm{tor}} > 0.9$ and roughly a 10 % up-down asymmetry inside of the pedestal top.

Our model of the overall asymmetry of the SXR radiation was based on Eqs. (4.13) and (4.14). The light impurity concentration, required to evaluate the bremsstrahlung level, was determined from the boron density measured by the CXRS system. Since the discharge was conducted only four days after a tokamak wall boronization, the boron is expected to be the dominant light impurity. The total SXR emissivity $\varepsilon_{\mathrm{tot}}$ in Eq. (4.14) was obtained by flux surface averaging of the experimentally measured SXR emissivity. The modeled two-dimensional SXR radiation profile, depicted in Fig. 6.3a, clearly demonstrates a very similar poloidal dependence as the experimentally observed radiation in Fig. 6.2. Additionally, the comparisons between the radial profile of the experimentally measured and modeled in/out and up/down asymmetries are shown in Figs. 6.3(b,c). The core asymmetry is significantly affected by the bremsstrahlung and therefore the measured, and also the modeled SXR asymmetry are substantially lower than the asymmetry of tungsten itself. The measured in/out asymmetry reproduce the modeled profile for $\rho_{\mathrm{tor}} < 0.5$ within the uncertainty, however, further outside 30 % discrepancy is present, which cannot be explained by the experimental uncertainty of neither the tomographic reconstruction nor the kinetic profiles used in the radiation model. This discrepancy will be explained after a careful investigation of the poloidal radiation profile in the next section. Some difference can be observed also in the up-down asymmetry, which do not fit our model at the edge of the plasma. However, a tomographic reconstruction of the emissivity so close to the edge from the line-integrated measurements is very inaccurate.

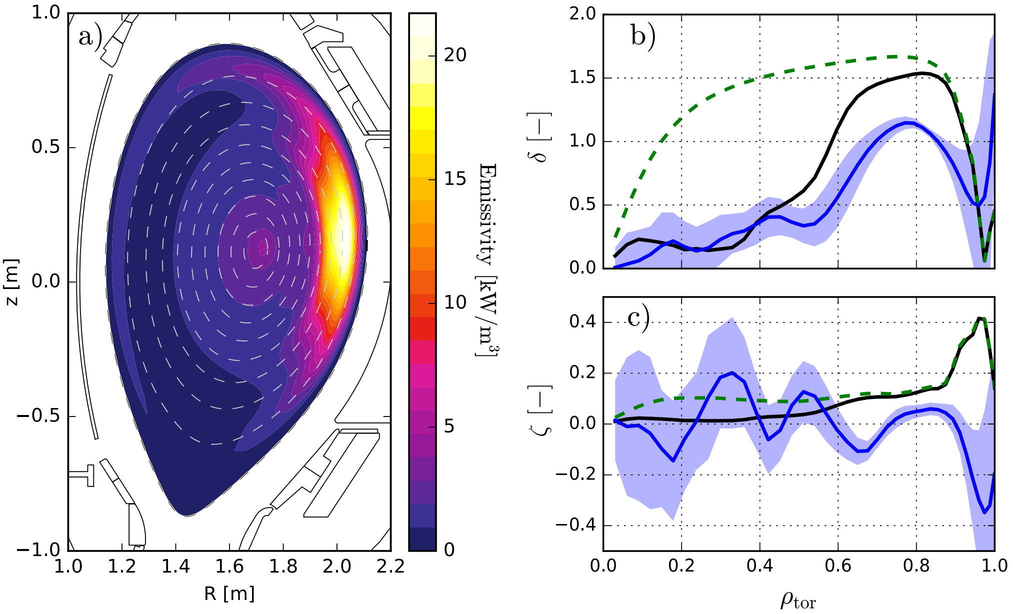

Figure 6.3.: a) Modeled 2D distribution of the SXR radiation in the discharge #30937 at 1.53 s, corresponding to the experimental profiles in Fig. 6.2. b) Profile of the in/out asymmetry δ and c) up/down asymmetry ζ, where the dashed line corresponds to the modeled tungsten asymmetry, full black line to the SXR radiation including radiation from a light impurities and background plasma and the blue line is the experimentally measured asymmetry.

6.1.3. Detailed Analysis of the Poloidal Profile

Elucidating the origin of the observed discrepancy at $\rho > 0.5$ requires a more comprehensive analysis of the poloidal radiation profile. The measured radiation profile in Fig. 6.4a was obtained by the mapping of the 2D SXR emissivity at $\rho_{\mathrm{tor}} = 0.75$ on the geometric angle. The measured SXR emissivity is almost constant at the HFS (i.e. for $\theta < -\pi/2$ and $\theta > \pi/2$), and it grows by a factor of six at the LFS. The modeled W density profile has a similar dependence, but a constant offset of $2.3\,\mathrm{kW/m^3}$ had to be added to match the observations. The bremsstrahlung is one order of magnitude smaller than this offset and thus cannot explain the additional radiation. This excessive SXR radiation is routinely observed at the edge of low-density discharges in AUG, and since it does not show asymmetry, it must be caused by light impurities, which are not affected by the centrifugal force.

The poloidal dependence of the total radiation reconstructed from the foil bolometers (cf. Fig. 6.4b) has a very similar shape as the profile from the SXR cameras. For the comparison, the modeled W emissivity was rescaled by the ratio of the total to the SXR cooling factors with respect to the SXR profile. The poloidal profile is slightly higher than expected, but the discrepancy can be explained by 5 % uncertainty in the electron temperature. In the total emissivity, no radiation offset is observed. The radiation peak is also slightly shifted towards the positive values of θ, which it is most probably a reconstruction artifact due to the poor coverage of the projection space by the bolometer cameras. Since this radiation offset occurs only at the plasma edge, our further investigations will be focused on the plasma core.

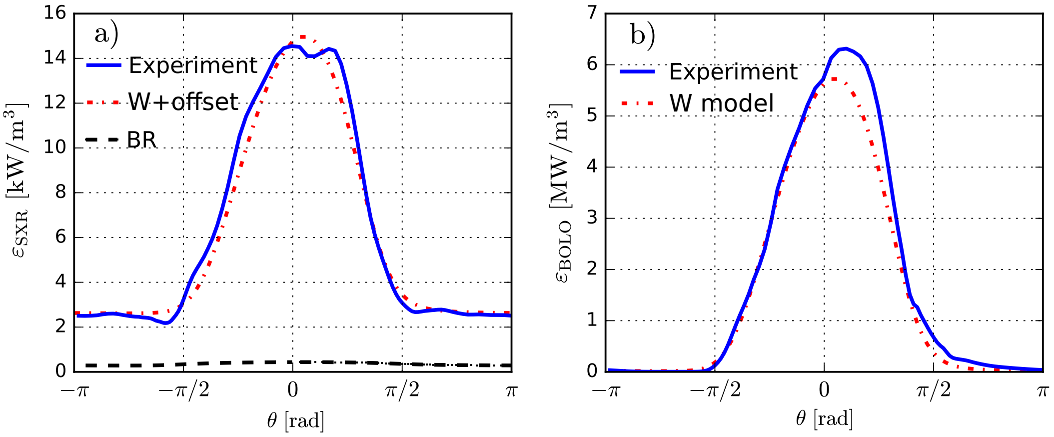

Figure 6.4.: (a) The poloidal profile of SXR emissivity from discharge #30937 at 1.533 s, $\rho_{\mathrm{tor}} = 0.75$ (full blue line), compared with the bremsstrahlung (BR, black dashed line) and the W radiation, shifted up by $2.3\,\mathrm{kW/m^3}$ offset. (b) Poloidal profile of the total radiation from the bolometers (blue) compared with the model (dash-dotted line).

6.1.4. Core Emissivity Profile

In order to verify the centrifugal force model also in the plasma core, we will investigate a radiation profile of the discharge #30937 at $t = 1.28\,\mathrm{s}$. The W density profile at this time point was strongly peaked due to a neoclassical inward convection. The inboard and outboard emissivity profiles are depicted in Fig. 6.5a, where the significant LFS asymmetry can be observed. The emissivity between the center and the pedestal top is varying by two orders of magnitude and by one order of magnitude between LFS and HFS. Therefore the tomographic reconstruction is more challenging than at $t = 1.53\,\mathrm{s}$, investigated before. Between $\rho_{\mathrm{tor}} = 0.2$–$0.6$, the reconstructed HFS emissivity profile match well the calculated HFS bremsstrahlung level, while more outside the radiation offset occurs, as was already reported in the previous section. The poloidal emissivity profile is depicted in Fig. 6.5b for $\rho_{\mathrm{tor}} = 0.4$ and an excellent match between the modeled and measured radiation profile was achieved. Small discrepancy on the right side of the poloidal profile can be a mere reconstruction artifact.

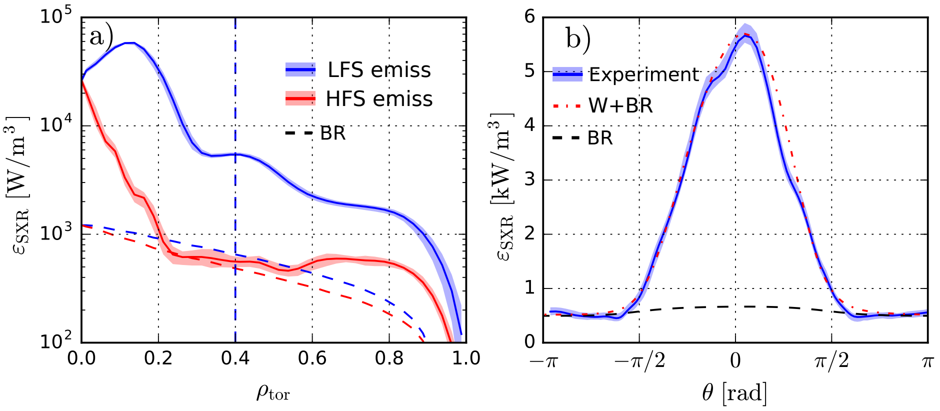

Figure 6.5.: a) Inboard (red) and outboard (blue) SXR emissivity profile depicted for the discharge #30937 at 1.28 s. The dashed lines indicates a inboard and outboard bremsstrahlung profile assuming boron to be the dominant light impurity. b) Poloidal emissivity profile evaluated at $\rho_{\mathrm{tor}} = 0.4$. Full blue line indicates the measured emissivity, dashed black line is bremsstrahlung and dash-dotted line represents tungsten emissivity. The tungsten concentration was fixed to match the emissivity maximum.

6.2. Asymmetry Driven by Fast Particles

Fast particle asymmetry introduce perturbation of the electrostatic potential, which enters the parallel force balance for the tungsten ions density by Eq. 5.41. Here, this effect is experimentally investigated. The previous discharge was chosen to maximize the centrifugal asymmetry, while the experiment described in this section should demonstrate the effect of the fast NBI ions. Only discharges with the highest fraction of the fast particles are suitable for such an analysis. Moreover, in order to investigate the effect of each NBI beam separately, discharges with a single beam only need to be examined. The largest difference is expected between the most tangential beam Q3 and the most perpendicular beam Q4 or Q8 which have a 30 % lower momentum input due to the higher acceleration voltage. Considering also other constraints regarding data quality, diagnostics availability, and discharge stability, only four L-mode discharges in the AUG database were found appropriate for our analysis: #32324, #32325, #32566 and #32569. Since all these shots were performed with the same plasma configuration, we will investigate in detail just the discharge #32566, where the beams Q3, Q4 and Q8 were used (see Fig. 2.2).

6.2.1. Properties of Plasma Discharge

The discharge #32566 was performed with a plasma current of 1.0 MA and $B_T = -2.66\,\mathrm{T}$, resulting in a moderate edge safety factor of $q_{95} = 4.4$ and large sawtooths crashes (sawtooth is a periodic MHD instability in the plasma core, causing flattening of the core profiles) with the inversion radius at $\rho_{\mathrm{pol}} = 0.4$. The discharge was heated by only 2.5 MW of NBI. The heating sequence was started with Q3 from 1.5–3 s, followed by Q4 from 3–4.5 s and Q8 from 4.5 to 6 s. In the first heating phase, the sawtooths period vary between 90–140 ms, when Q4 was switched on, the period has decreased to 60–80 ms, and at last during heating by Q8 the period has increased again to 60–100 ms. The low electron density was gradually increasing from $2.5{\cdot}10^{19}\,\mathrm{m}^{-3}$ to a still rather low value of $3.5{\cdot}10^{19}\,\mathrm{m}^{-3}$, which seemed to be low enough to prevent the transition into H-mode.

The time trace of the ion temperature and the plasma rotation can be found in Fig. 6.6a–b. The ion temperature in the second and the third phase in which Q4 and Q8 heated the plasma, is 25 % lower than in the first phase due to a flatter ion heat deposition profile and a higher density. However, the core plasma rotation is reduced by 50 % in the phase with Q4 and 35 % in the phase with Q8 heating as compared to the Q3 phase. The change in toroidal rotation is caused by a different injection angle of the beams; the most parallel is Q3, while the most perpendicular is Q4. The total injected torque, together with ion and electron heating calculated by TRANSP is depicted in Fig.6.6c. Switching from Q3 to Q4 has reduced the injected torque T_φ by a factor of two, while the ion and electron heating are almost constant. Finally, in Fig. 6.6d the total toroidal angular momentum L_φ of the plasma and the total stored energy W_{MHD} are shown. The periodic reduction of W_{MHD} every 0.5 s is caused by intentionally switching the beam for 20 ms, but the mean value of W_{MHD} is almost unaffected by the variation of the beam sources.

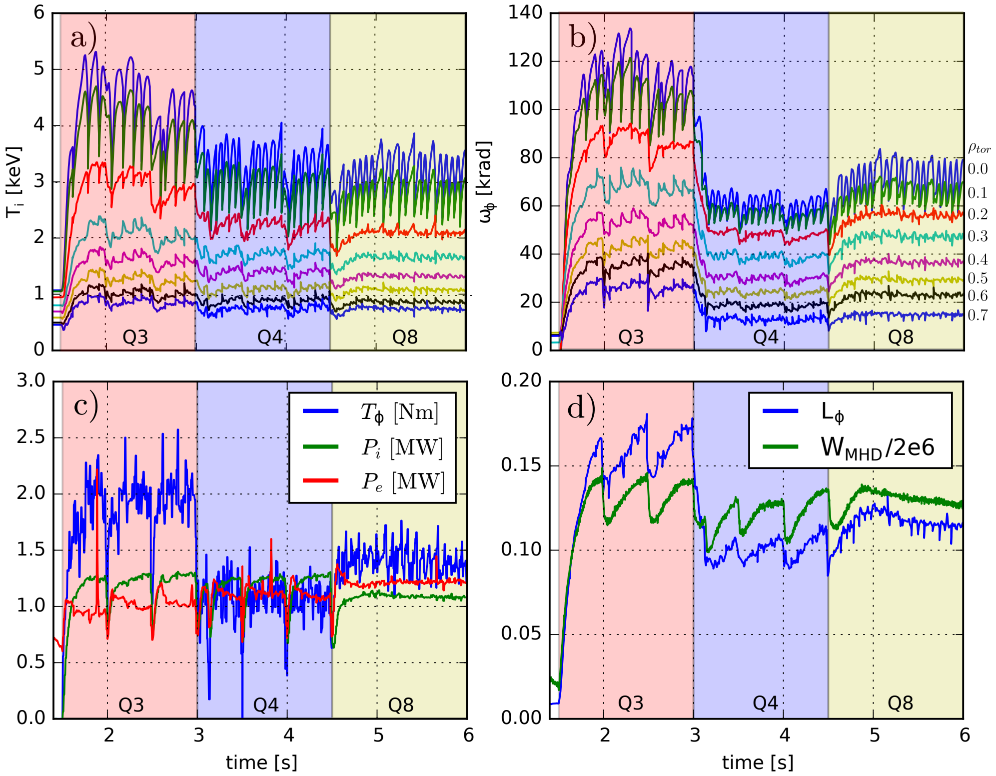

Figure 6.6.: Timetraces of various quantities in discharge #32566 are presented. a) The ion temperature at equally radially spaced positions from the core towards the edge, b) the angular rotation velocity, c) the total NBI torque (blue), the ion heating power (green) and the electron heating (red), d) the toroidal angular momentum of the plasma (blue) and total stored energy (green) are depicted.

6.2.2. Fast Particle Modeling

The fast particle distribution on AUG can be probed directly via the fast ion D-alpha (FIDA) diagnostic [85, 123]. Because FIDA provides only the measurements at the outboard side of the plasma, the fast particle asymmetry cannot be determined directly. Moreover, the conditions in the discharge #32566 were not optimal to measure the distribution function with the necessary accuracy due to the low signal level. The other available option to estimate the fast particle distribution function is the NUBEAM code [98] in TRANSP, which models the time traces of the fast particle density, their perpendicular and parallel pressure and temperature. Moreover, at a few selected time-points, the particle distribution as a function of energy E, the pitch angle $v_{||}/v$, ρ_{tor} and the poloidal angle can be extracted.

The NUBEAM simulation was calculated with $2 \cdot 10^5$ particle clusters, 40 radial bins and 10 ms time resolution. The redistribution of the fast particles by sawtooth crashes

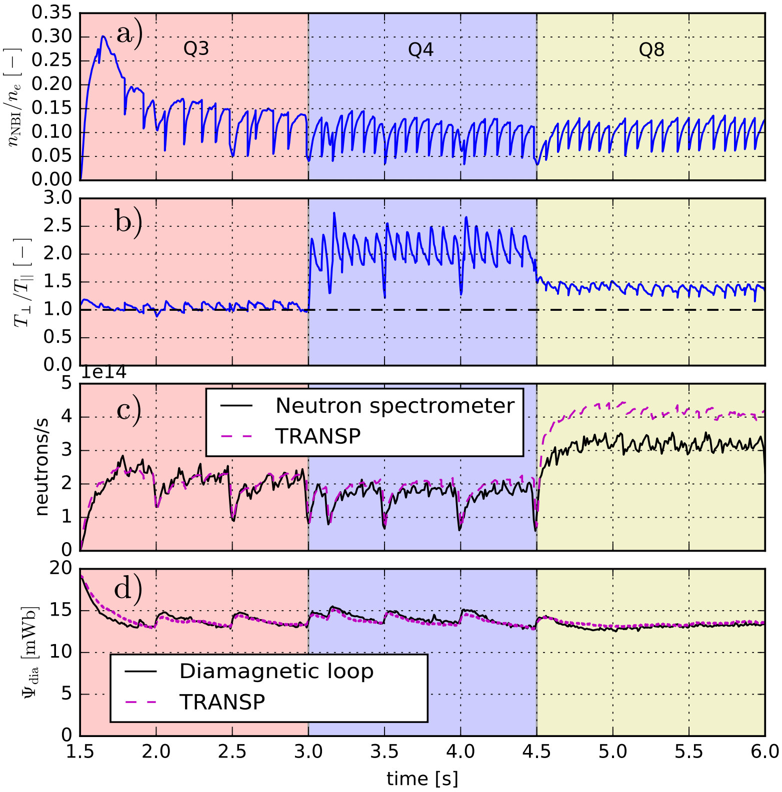

Figure 6.7.: a) Fast particle fraction in the center of the plasma for discharge #32566 calculated by the NUBEAM, b) the temperature anisotropy of the fast ions in the plasma core from NUBEAM, c) neutron flux from the spectrometer [124] and the TRANSP prediction and d) diamagnetic flux modeled by TRANSP compared with the measurement

was included using the simple Kadomtsev model. The effective charge was estimated from the loop voltage to be $Z_{\text{eff}} \approx 1.2$. The basic overview of the results is presented in Fig. 6.7. The central fast particle density decreased from 30 % to 15 % during the Q3 heating phase and then it stayed almost constant at 10 % till the end of the discharge. In Fig. 6.7b, the fast particle temperature anisotropy is shown. In the first phase with the Q3 beam the temperature anisotropy was almost negligible, while in the phase with the more perpendicular beam Q4, the anisotropy increased to $T_\perp/T_{||} \approx 2$ and later during the Q8 phase it dropped again to about 1.4. The neutron rate in Fig. 6.7c depends mostly on the fast particle density and energy. Because the absolute calibration for the neutron spectrometer is unavailable, we have rescaled the number of measured neutrons to the TRANSP results in the Q3 phase. In the Q4 phase, which was also with a 60 keV NBI source, the calculated neutron rate corresponds to the measured rate, however, in the later phase with the 93 keV beam the rate was overestimated by 30 % which implies an over-predicted fast particle density by TRANSP. Nevertheless, the most interesting for this study are beams Q3 and Q4. Finally, in Fig. 6.7d the measured and calculated diamagnetic flux are compared. The diamagnetic flux is sensitive to the perpendicular pressure of the particles and an match between the measured and modeled flux indicates good quality of the fast particle model in TRANSP [125].

6.2.3. Fast Particles Asymmetry

The poloidal distribution of the fast particles was determined using three different methods. At first, the fast particle distribution function from NUBEAM was integrated over the energy and the pitch ($v_{||}/v$) to get the spatial profile of the fast particle density. The background subtracted 2D profile for each of the three NBI heating phases is depicted in Fig. 6.8 for time-points shortly before the flattening by a sawtooth crash. Significant in-out asymmetry is present in each of the profiles, but the largest asymmetry is driven by the Q4 beam due to the larger fast particle anisotropy.

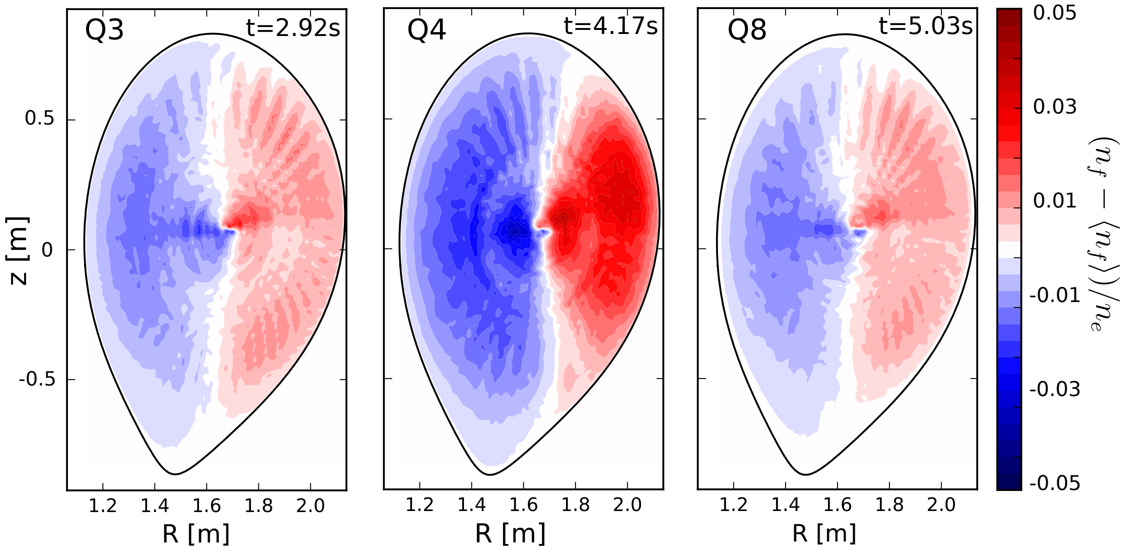

Figure 6.8.: Fast particle asymmetry normalized by the electron density for three beams sources Q3,Q4 and Q8 in discharge #32566 obtained by integration of the distribution function of the pitch angle and the energy and subtracting the flux surface average.

The second method used to estimate the in-out asymmetry is based on the bi-Maxwellian model. The parallel and perpendicular temperatures are stored by TRANSP for each timepoint and therefore, the asymmetry can be evaluated for the whole discharge according to the formula (5.48).

Finally, the third method is based on the analytical model introduced in Sec. 5.2.4. This model depends on the fast particle density computed by NUBEAM, but the pitch

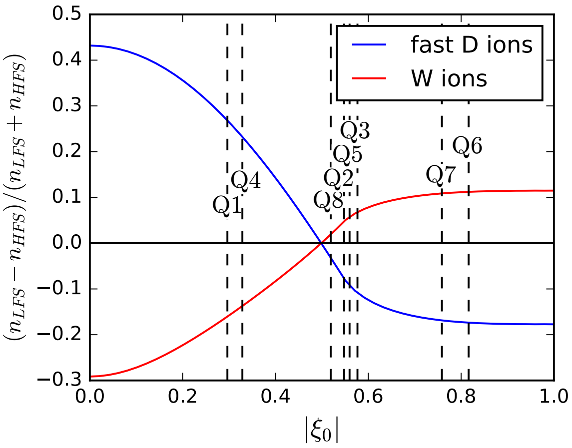

Figure 6.9.: Poloidal asymmetry of the fast particles (blue) and W ions (red) evaluated by the analytical model described in Sec. 5.2.4 at $\rho_{\text{tor}} = 0.3$ assuming 10 % fast particle fraction and using model in Eq. (5.41) for W ions. Dashed vertical lines indicate injection points of the AUG NBI sources.

distribution is estimated independently. The pitch of the injected ions ξ_0 was determined as the cosine between the magnetic field and the vector of the particle beam, and averaged between the LFS and the HFS intersections of the flux surfaces. Fig. 6.9 shows the poloidal asymmetry as a function of ξ_0 and the vertical dashed lines indicate the mean pitch angles of the ions from the NBI sources used in distribution function (5.48). NBI sources Q1 and Q4 should produce a higher tungsten density on HFS, while the others should drive the LFS density accumulation.

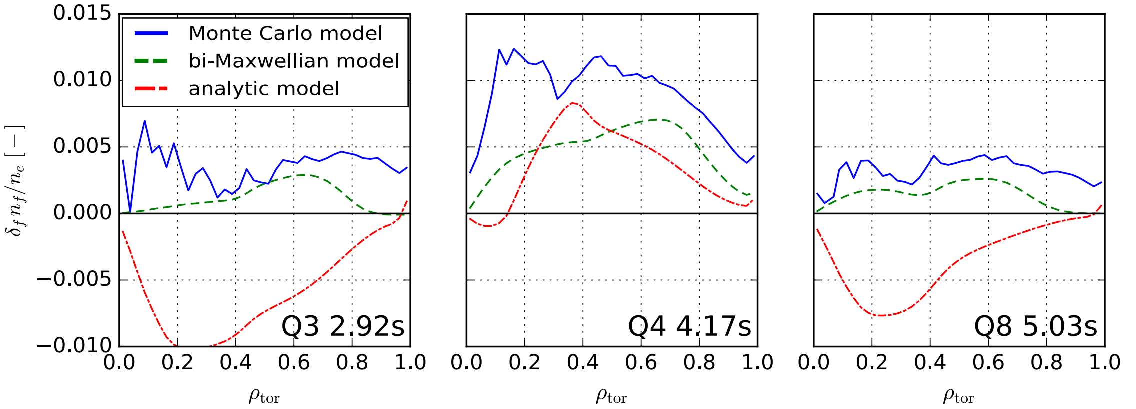

Figure 6.10.: Asymmetry of the fast particles δ_f normalized by their fraction n_f/n_e evaluated for all three heating phases shortly before a sawtooth crash. The full line indicates the asymmetry obtained directly from the 2D distribution of the fast particles in NUBEAM. The dashed line represents the asymmetry assuming a bi-Maxwellian distribution and the analytical model from Sec. 5.2.4 is shown by the dash-dotted line.

All the three methods are compared in the Fig. 6.10. The Monte Carlo model in NUBEAM is predicting for all time-points a surplus of fast particles outboard side, the largest for Q4 and significantly smaller for Q3 and Q8. On the contrary, the analytical model predicts negative asymmetry for this two beams and smaller positive asymmetry for Q4. The deviation is most probably caused by the finite orbit width effect, which are not included in the analytical model. The particles ionized on the LFS of the plasma continue in their trajectories towards the HFS, however, due to the ∇B drift, they are moving closer towards the magnetic axis. On the other hand, particles ionized on the HFS shift more outside when passing the LFS. Due to a large gradient in the fast particle density this effect will cause a surplus of the particles on the LFS and an additional outboard asymmetry.

The bi-Maxwellian model predicts the same sign of the asymmetry because finite orbit width effects are partially included when the temperature profile is evaluated by NUBEAM. However, the disagreement in the core is most probably also a consequence of finite orbit width, because in the core is the deviation of the fast particles from the flux surface the largest.

6.2.4. Comparison with the Experiment

The time evolution of the poloidal asymmetry at $\rho_{\mathrm{pol}} = 0.2$ of discharge #32566 is depicted in Fig. 6.11. During the Q3 phase, the experimental asymmetry (green line) is rather well described by the basic centrifugal model from Eq. (5.35) (red line), and the Monte Carlo model including fast particle effects from Eq. (5.41) (blue line) differ only in the rise up phase between 1.5 and 2.0 s. An apparent mismatch between the centrifugal model and the experimental asymmetry can be observed during the Q4 phase. When the fast particle effect is included, the discrepancy disappears and the inter-sawtooth evolution of the asymmetry is much better described. During the Q8 phase, the experimental asymmetry is slightly overestimated by the model. Since the other fast particle models introduced in the previous section predicts significantly weaker effect for for Q4 and Q8 sources (cf. Fig. 6.10), a large mismatch with the experiment was observed and they can not be used to describe the origin of this asymmetry.

In order to minimize the possibility of the experimental errors, the same investigations were also performed on the rest of the available discharges (#32324, #32325 and #32569). In Fig. 6.12, one can find the overall comparisons between the modeled and the measured asymmetry. Each point is averaged over 0.1 s, i.e. roughly a one sawtooth cycle to reduce the scatter. A clear discrepancy can be observed for centrifugal model of the beam Q4 (open green symbols), while the beam Q3 (open red symbols), while when the fast particles are included (full symbols) the model provides excellent match with the experiment. Only a few points from beam Q3, corresponding to the initial non-stationary phase of the NBI heating underestimate the experiment. It is expected

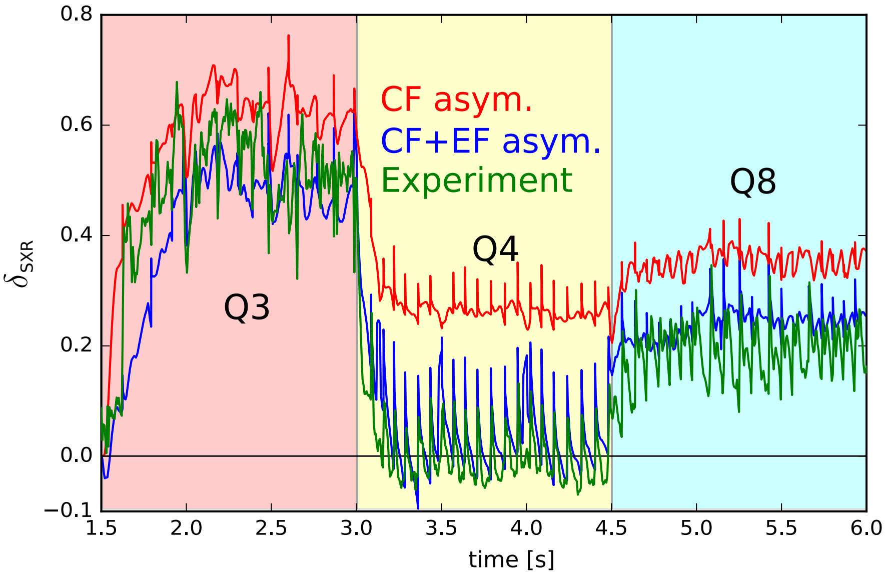

Figure 6.11.: The temporal evolution of the SXR poloidal asymmetry is presented for the discharge #32566 at $\rho_{\mathrm{pol}} = 0.2$ (green), compared with the basic centrifugal model (red) and to a model with the electric force generated by the fast particles (blue).

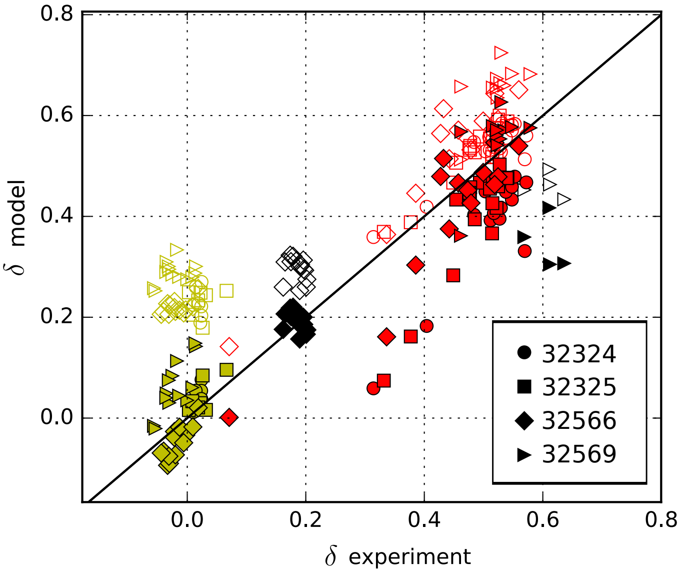

Figure 6.12.: Comparisons of the experimentally measured and modeled asymmetry at $\rho_{\mathrm{pol}} = 0.2$, where the open markers denote the basic centrifugal model and full markers correspond to a model with fast ions. Each point is the averaged over one sawtooth cycle.

that the fast particles distribution function or fast particles density profile used to calculate the rest of the Q3 phase did not match the fast particles distribution in this initial phase.

6.3. Summary

In this chapter, we have demonstrated the capabilities of the SXR diagnostic in combination with our state of the art tomography reconstruction code to measure the poloidal asymmetry of the tungsten density in NBI-only heated discharges. At first, the validity of the centrifugal model was verified on the discharge #30937 with improved confinement. Outboard accumulation of tungsten enabled to investigate the poloidal radiation profile in great detail. In the beginning, a significant discrepancy between the observed asymmetry and the model has been found. Our detailed investigation of the poloidal radiation profile has revealed additional contributions to the SXR radiation caused by light impurities with a small centrifugal asymmetry, exceeding the expected bremsstrahlung level by an order of magnitude. The residual, poloidally varying part of the SXR profile was very well described by the modeled tungsten radiation. The poloidal profile of the tungsten density was also confirmed by comparison with the tomographic reconstruction of foil bolometer signal, where a very good match in the shape and also the magnitude of the radiation profile was achieved.

Further investigations have been devoted to studying the effects of fast NBI particles on the in-out asymmetry of tungsten ions. The fast NBI particles driven asymmetry has never been observed before and therefore, the set of the analyzed discharges represent the first experimental confirmation of this effect. The largest deviation from the basic centrifugal asymmetry was observed during heating by the most perpendicular Q4 NBI source, while the more parallel Q3 beam has not caused any measurable effect.

In order to explain these observations, three models for the fast particle distribution were compared; the model assuming a bi-Maxwellian distribution, the analytical model without the finite orbit width effects and a full Monte Carlo (MC) model from NUBEAM. The MC model has provided an excellent match with the experimentally observed asymmetry including a variation during the sawtooth cycle due to flattening of the fast particles density profile. The other models predicted much weaker effect of the fast particles, because of the neglected finite orbit width effect.

7. ICRF Driven Poloidal Asymmetries

Minority ions accelerated by ion cyclotron range of frequencies (ICRF) heating are expected to play a fundamental role in the parallel impurity force balance via the perturbation of the electrostatic potential driven by magnetic trapping of these ions (see Sec. 5.2.3). In the scheme used here, ICRF couples to the minority ions, i.e. the protons present in a low concentration in the deuterium plasma. Compared to the effect of fast ions injected by NBI, the poloidal asymmetries can be substantially larger because of a higher temperature anisotropy (i.e. $T_\perp \gg T_{||}$) of ICRF accelerated ions.

Despite the significant advances in diagnosing fast ions in plasma, the phase space of the highly energetic ($E > 100\,\mathrm{keV}$) minority protons at their birth location is hardly observable due to their low cross-sections for charge exchange and nuclear reactions. Here, a detailed analysis demonstrates that poloidal asymmetries of tungsten ions can indirectly provide information about the pitch distribution of the fast particles. The measurement of poloidal asymmetries thus provides a unique possibility to analyze these ions. In this chapter, we will investigate the presence of the poloidal tungsten asymmetries in AUG and their possible applications for fast particle studies.

7.1. Low-Field Side Heated Discharge

First, we select discharges, where the magnitude of the poloidal asymmetries is supposed to be the largest. Compared to NBI, where only source could be varied, ICRF provides more flexibility. The parameters of the fast particle distribution function can be varied by scanning the ion cyclotron resonance position. The low-field side (LFS) heating has typically the advantage of producing more anisotropic temperature distributions, leading to a higher fraction of the trapped particles (Sec. 5.2.3). The more central the resonance is, the smaller is the heated volume, and the higher power per particle is available, leading to a larger temperature anisotropy. On the other hand, the perturbation of the electrostatic potential depends on the magnetic mirror effect, which becomes larger when moving away from the magnetic axis. The optimal radial position is a compromise between these two effects. Our experimental observations suggest the location of the IC resonance at $\rho_{\mathrm{tor}} = 0.2$–$0.3$ should maximize the poloidal asymmetry. Moreover, low plasma density is beneficial to achieve high power per particle P_{IC}/n_e and thus a large temperature anisotropy. Too low density, however would result in poor coupling of the ICRF power to the plasma. Finally, sufficiently high electron temperature is necessary to monitor the poloidal distribution of the tungsten by the SXR diagnostic.

7.1.1. Experiment description

These requirements are fulfilled by only a few AUG discharges, like the set #30810–30812. Because these discharges are almost identical, we will investigate in detail only #30812, where the asymmetries could be measured most accurately due to a favorable shape of the radiation profile. In Fig. 7.1 the time traces of relevant parameters of this discharge are depicted.

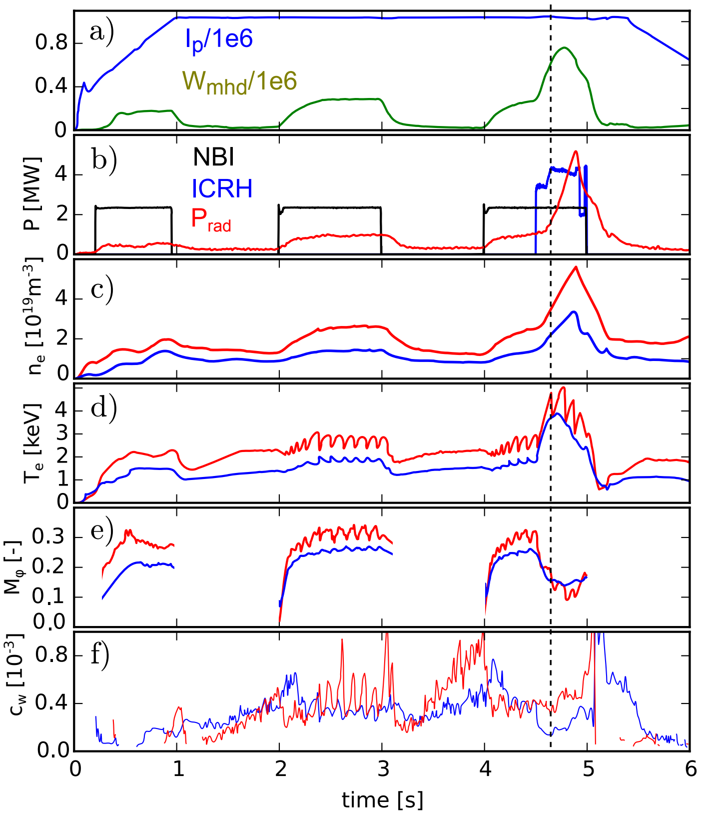

Figure 7.1.: Time traces of the plasma parameters for the discharge #30812: plasma current I_p and total stored energy W_{MHD}, b) NBI and ICRF heating and radiated power, c) core (red) and edge (blue) line-averaged density, d) electron temperature, e) deuterium Mach number f) tungsten concentration. The vertical dashed line indicates the later investigated time point $t = 4.65\,\mathrm{s}$.

During the discharge, the beam Q3 was periodically switched on for an independent investigation of the fast NBI ions. The most interesting tungsten behavior occurred between 4.5 and 5 s, where also ICRF heating was applied with the resonance position $R_{\mathrm{resz}} = 1.82\,\mathrm{m}$ ($\rho_{\mathrm{tor}} = 0.25$ at LFS). Turning on the ICRF leads to the L-H transition and a simultaneous fast increase of the electron density and temperature. Later, in the discharge the tungsten influx from the ICRF antennas caused rise of the W density and consequently also of the radiated power, leading to a sudden drop of the electron temperature in the second half of the ICRF heated phase. During the NBI-only phase (up to 4.4 s), the deuterium Mach number reached values of about 0.3. However, the increase in the ion temperature and the reduction of the momentum confinement [126] during the ICRF heating decreased Mach number down to 0.1.

The snapshot around $t = 4.65\,\mathrm{s}$ was analyzed in detail, since the plasma was not perturbed by sawtooth yet and ICRF was already at full power. Later, the sawtooth crash caused a flattening of the fast particle density, and an asymmetry not reached the same value again due to a subsequent increase in the electron density. The kinetic profiles at $t = 4.65\,\mathrm{s}$ are depicted in Fig. 7.2. Note that the cote $T_e = 4.65\,\mathrm{keV}$ is much lower that core $T_i = 8\,\mathrm{keV}$. The Mach number was equal to 0.21 in the core, indicating a non-negligible centrifugal force. An estimated hydrogen minority fraction was assumed to be 4 % and the effective ionic charge, Z_{eff}, was approximately 2.0, which was determined from the impurity content of the plasma. Since the measured W concentration was of the order of 10^{-3}, more than 90 % of the core SXR radiation was emitted by tungsten ions.

7.1.2. SXR radiation profile

The poloidal asymmetry of the SXR profile started to evolve immediately after switching on the ICRF heating. The largest high-field side (HFS) tungsten accumulation has been reached just before the sawtooth crash at 4.67 s. The corresponding SXR brightness and the reconstructed emissivity profile are depicted in Fig. 7.3. The large in-out asymmetry is well visible already in the line integrated brightnesses measured by the cameras F, G, K, L, and M (for their geometry check Fig. 3.1b). The tomographic reconstruction confirms the location of the tungsten emissivity on the HFS, on the opposite side of the flux surface with respect to the ICRF resonance. An excellent agreement between all SXR cameras observing the plasma and the moderate regularization level of $q_\lambda = 49\,\%$ selected by a generalized cross-validation (GCV) indicates a high fidelity of the reconstruction. Moreover, due to a slightly hollow radiation profile, the asymmetry profile is only weakly affected by the uncertainty in the plasma position.

Even more features are visible in Fig. 7.4, where one can see a horizontal and a vertical cut through the SXR emissivity. Obviously, a significant HFS accumulation is present in the horizontal cut (Fig. 7.4b) from the center up to $\rho_{\mathrm{tor}} = 0.38$, including the position of the ICRF resonance. The emissivity asymmetry in the outer region is caused by the centrifugal force (Fig. 7.4b).

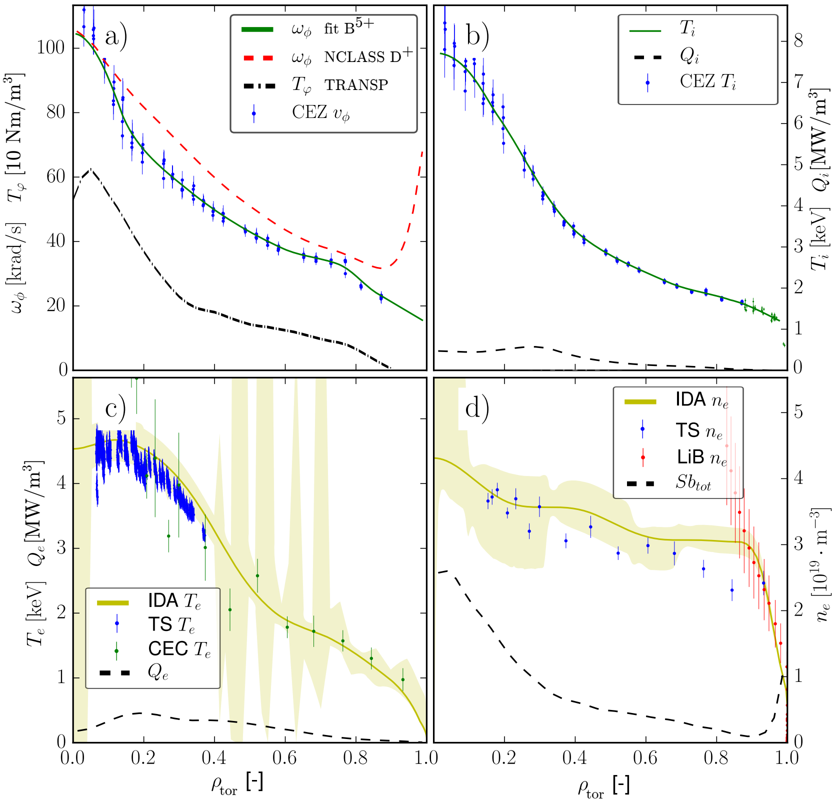

Figure 7.2.: Kinetic profiles of the discharge 30812 at 4.64 s: a) The blue points represent the plasma angular velocity measured on the boron ions, the red dashed line is that of the main ions after application of the neoclassical correction, and the black dashed line indicates the torque density [10 Nm/m^3] as calculated the TRANSP, b) blue dots represent ion temperature and the black dashed line indicates the ion heating profile Q_i [MW/m^3], c) electron temperature from TS (green) and ECE (blue) with a spline fit obtained from IDA, d) electron density calculated by IDA from the combination of the DCN and lithium beam and the neutral particle source term Sb_{tot} [$5\cdot10^{19}$ m^{-3}s^{-1}] from the TRANSP (dashed line)

7.1.3. Fast particle modeling

A realistic modeling of the poloidal density asymmetries relies on an accurate prediction of the ion distribution function in the presence of ICRF heating. This is achieved by simulating the wave propagation and absorption inside the plasma and simultaneously by estimating the impact of the RF wave on the distribution function of the resonating ion species. For the wave propagation and absorption we use the full-wave TORIC code, which solves the wave equation in hot plasmas for arbitrary distribution functions [127]. For the solution of the quasilinear Fokker-Planck equation, which describes the evolution of the distribution function, TORIC is interfaced with SSFPQL solver

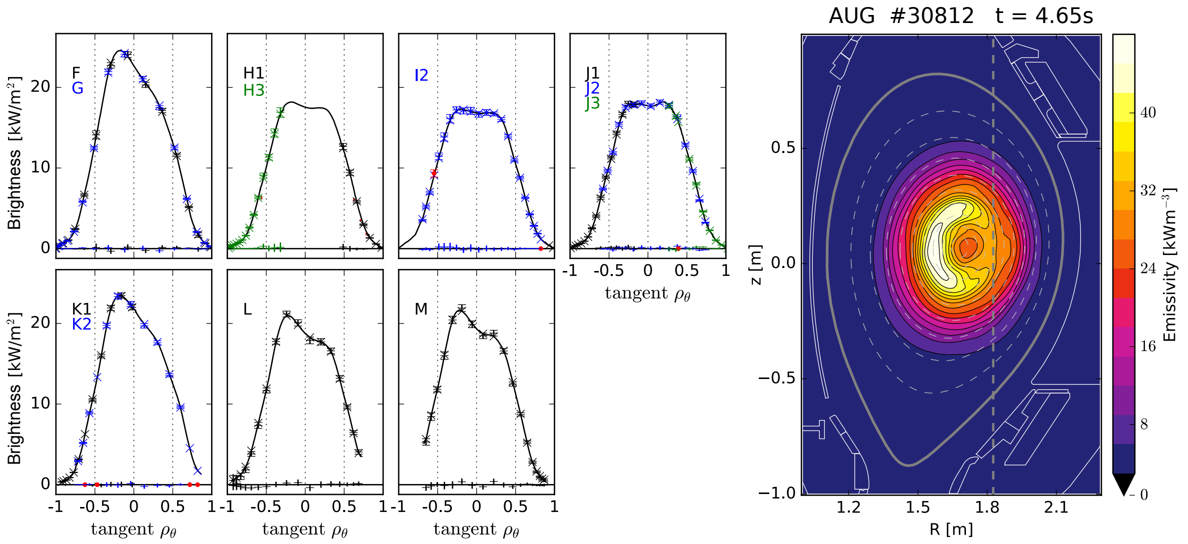

Figure 7.3.: The brightnesses (left) and the reconstructed emissivity profile (right) measured in the discharge #30812 at 4.65 s. The vertical dashed line indicates a resonance surface of the ICRF. The reconstruction was evaluated in the resolution 100×150 px, with the residuum $\chi^2/m = 2.5$ and a regularization level of $q_\lambda = 49\,\%$, indicating a low regularization level.

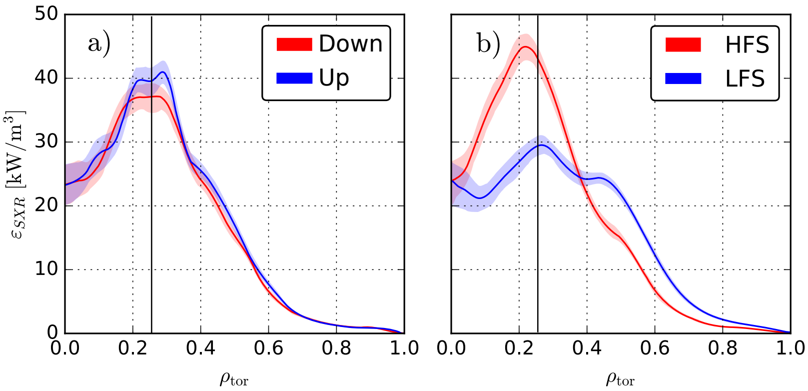

Figure 7.4.: a) Vertical and b) horizontal cut through the SXR emissivity profile in Fig. 7.3 with the confidence intervals determined from the covariance matrix in Eq. 4.11. The horizontal line corresponds to the position of the ICRF resonance surface.

[128], which looks for the steady-state solution of the surface-averaged Fokker-Planck equation in the presence of ICRF and NBI heating [96]. Briefly, TORIC evaluates the power deposition profiles, which are then used by SSFPQL to construct the wave-interaction quasilinear operator in the Fokker-Planck equation, and in turn TORIC employs the distribution functions calculated by SSFPQL for the plasma response in the wave equation. This nonlinear two-step procedure between TORIC and SSFPQL is

repeated until the profiles of the RF deposited power calculated by the two codes agree up to a tolerance threshold decided by the user. Alternatively, TORIC is interfaced with FFPMOD [94] for the Fokker-Planck equation in TRANSP suite for plasma transport studies [95].

The simulation was performed with the kinetic profiles presented in Fig. 7.2, using the magnetic equilibrium and diamagnetic correction for the toroidal magnetic field from TRANSP. The coupled ICRF power (i.e., total power without the reflected power and the power lost in RF lines) was 4.3 MW, assuming a complete absorption of the IC wave. Results of the modeling by the both codes are summarized in Fig. 7.5. The calculated power density profile is rather different between the models; TORIC-SSFPQL is predicting a substantially higher power density in the core for $\rho_{\mathrm{tor}} < 0.25$, while the power from TRANSP-FPPMOD is shifted slightly outside. Consequently, also the minority temperature from TORIC-SSFPQL is higher in the plasma center. Because the temperature in TRANSP is stored as the flux surface averaged value, we have used the Dendy's model (Sec. 5.2.3) to determine the temperature on LFS (Eq. (5.47)).

The resulting temperature anisotropy is shown in the Fig. 7.5c. The TRANSP-FPPMOD predicts the largest anisotropy on a resonance radius, while TORIC-SSFPQL shifts the maximum slightly more inside. The anisotropy of the deuterium ions accelerated by a second harmonic heating has not been accounted for in the model of the poloidal asymmetry because the Dendy's model is not suitable for their description. The Fig. 7.5d, with the measured poloidal asymmetry, will be discussed with the ICRF models in the next section.

7.1.4. Parallel Force Balance

The last step is the evaluation of the poloidal asymmetry. Because of the rather high W concentration of $c_W \approx 5 \cdot 10^{-4}$, i.e. $c_W Z_W^2 \approx 1$, the assumption of tungsten being a trace impurity is not valid anymore. Therefore, the approximation derived in Eq. (5.41) cannot be applied, and differential-algebraic equations of the parallel force balance (cf. Eq. (5.32)) for all species in the plasma need to be solved self-consistently [93]. The direct solution gives about 20 % smaller asymmetry than one would expect from the approximation. We have compared the measured poloidal asymmetry δ_{SXR} with the model of SXR asymmetry in Fig. 7.5d. In the outer region ($\rho_{\mathrm{tor}} > 0.7$) reasonable agreement with the centrifugal force-based model was found, but a significant discrepancy occurs more inside. When the fast particle effects are included in the model, an improvement of the agreement between the experiment and the model can be observed. But still, a significant discrepancy is localized inside of the resonance surface ($\rho_{\mathrm{tor}} > 0.2$), where both codes disagree and the experimental

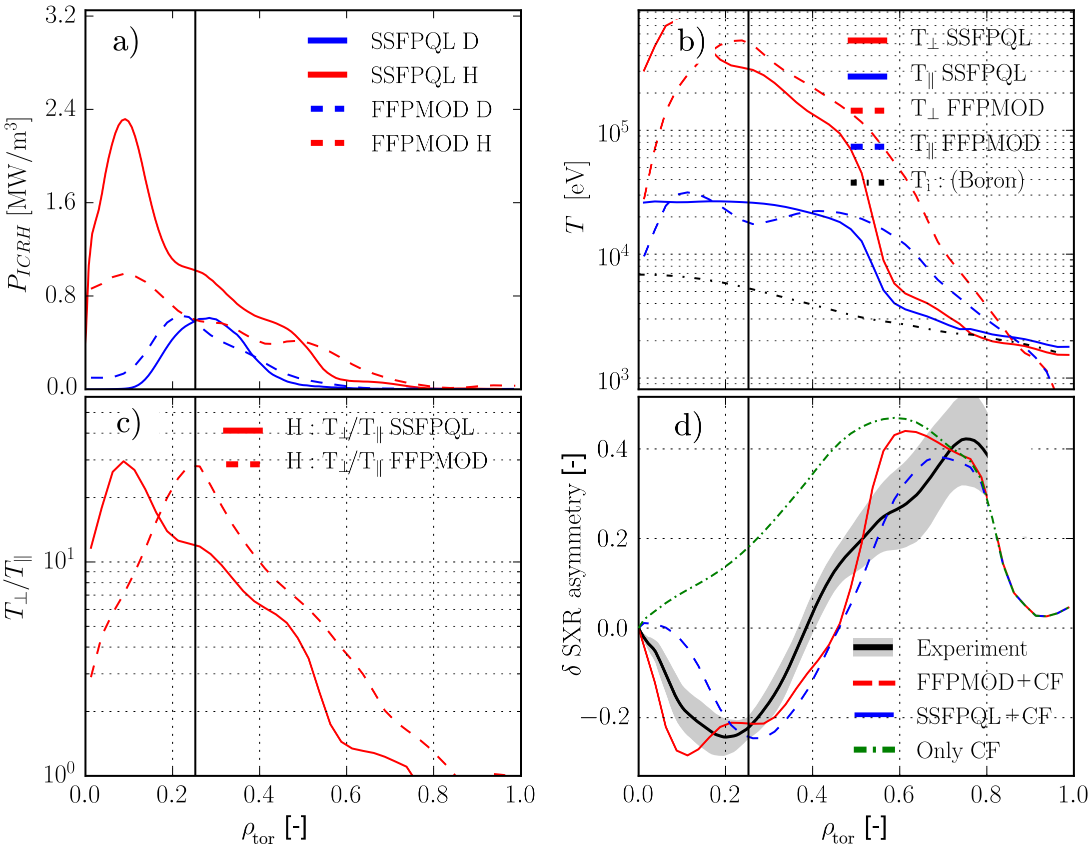

Figure 7.5.: a) Plot illustrates the power density from TORIC-SSFPQL (full line) and TORIC-FPPMOD from TRANSP (dashed line) for hydrogen (red) and deuterium (blue). The vertical line indicates position of the cold ICRF resonance. b) The modeled minority temperatures were evaluated at the LFS for both codes. c) LFS value of the temperature anisotropy d) The modeled poloidal asymmetry of SXR profile compared with the measured value.

value is in between them. The disagreement is a direct consequence of the difference in the temperature anisotropy predicted by both codes. Moreover, the relatively small discrepancy also occurs between $\rho_{\mathrm{tor}} = 0.4 - 0.6$, however it a small difference within an expected uncertainty of the modeling.

Fig. 7.6 illustrates the poloidal variation of the reconstructed SXR emissivity at the resonance surface ($\rho_{\mathrm{tor}} = 0.25$). The TORIC-FPPMOD model shows significantly stronger poloidal dependence which is a consequence of two times higher temperature anisotropy compared to TORIC-SSFPQL. The lower variation of the measured poloidal profile can also be caused by finite Larmor radius ($r_L \approx 3\,\mathrm{cm}$), finite orbit width effects or radial transport, which were not included in the modeling. On the other hand, the fact that the measured and modeled emissivity is almost flat on the HFS and most of the variation occurs on the LFS ($-\pi/2 < \theta < \pi/2$) confirms the Dendy model, since the simple bi-Maxwellian model (5.43) would result in a cosine dependence. Moreover, neither TORIC-SSFPQL nor TORIC-FPPMOD takes into account the poloidal variation in the minority density, changing between LFS and HFS by a factor of 3, which can significantly affect the power absorption profile. Despite of this shortcoming in the modeling of the fast particle distribution, a satisfactory match between the model and experiment was achieved, indicating sufficient quality of the measurements and the tungsten density model. Further investigation of this discharge can be found in [129], where the poloidal asymmetry was unfolded to infer the fast ion distribution function.

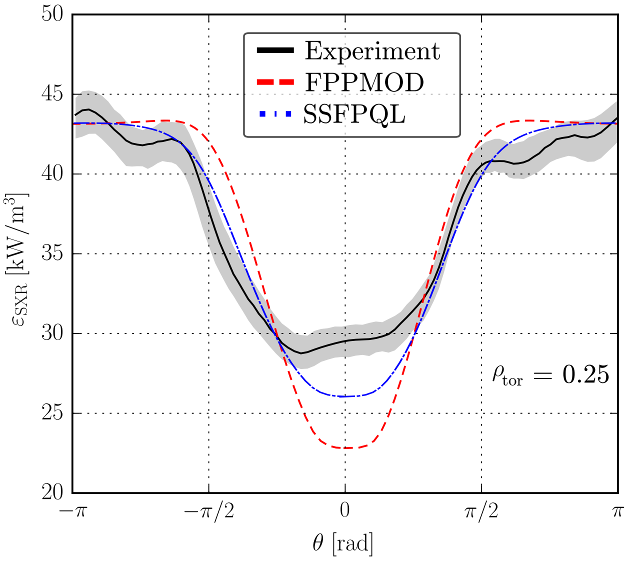

Figure 7.6.: Poloidal variation of the SXR emissivity in discharge #30812 at 4.65 s and $\rho_{\mathrm{tor}} = 0.25$ (full black line) compared with the model based on fast particles from TORIC-FPPMOD (red dashed) and TORIC-SSFPQL (blue dash-dotted line). The modeled profile was normalized with respect to the HFS experimental emissivity.

7.2. ICRH heating on the high-field side

Another interesting case represents the discharges heated on the HFS. The observation from Alcator C-mod [84] indicates zero impurity asymmetry within the experimental uncertainty, while the modeling based on Dendy's model [93] predicts slightly excessive impurity density on the LFS. In order to investigate such effects, we will analyze the discharge #30516 at 4.8 s with the ICRF resonance localized inboard at $\rho_{\mathrm{tor}} = 0.13$.

The plasma was heated by ICRF, with $P_{\mathrm{IC}} = 4.0\,\mathrm{MW}$ and the central ECRH delivering $P_{\mathrm{EC}} = 1.2\,\mathrm{MW}$, while no NBI heating was applied to avoid centrifugal force. The heat flux across the separatrix was sufficient to trigger the L-H transition, leading to an improved particle confinement. The electron density has thus reached value of $n_e = 8 \cdot 10^{-19}\,\mathrm{m}^{-3}$, which is two times more than in the previously studied case.

The SXR radiation profile, depicted in Fig. 7.7, is more peaked compared to that presented in Fig. 7.3. The peaked profile is a consequence of a steeper electron temperature profile in combination with a lower central temperature, ($T_{e0} = 4.2\,\mathrm{keV}$), leading to a peaked SXR radiation profile while the W density is approximately flat. The asymmetry determined from the steeper radiation profile is more sensitive to the inaccuracies in the magnetic equilibrium according to Eq. (4.15).

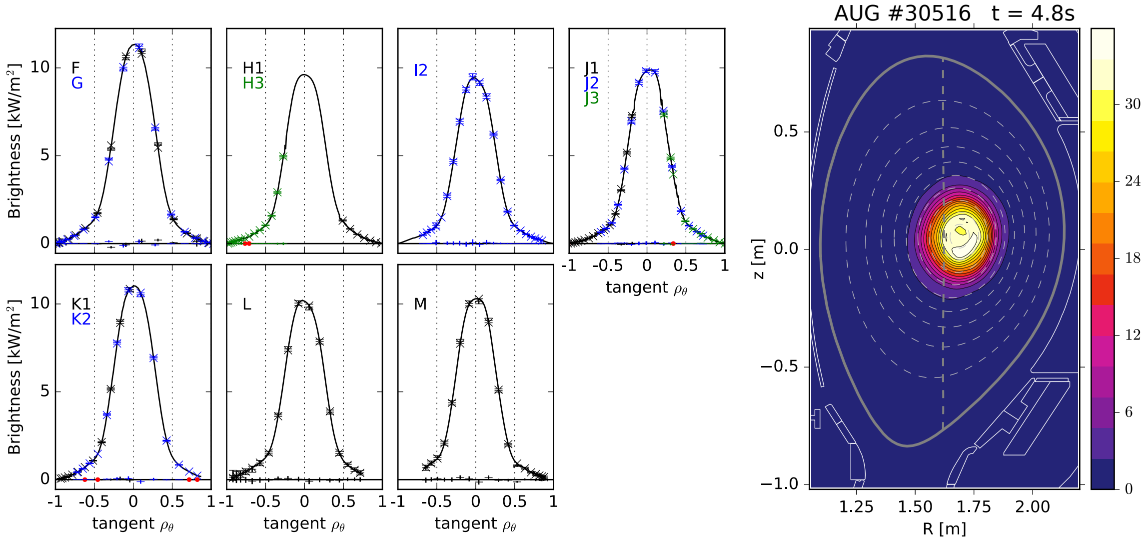

Figure 7.7.: Akin to Fig. 7.3 for discharge #30516 at 4.8 s. The regularization level estimated by GCV was $q_\lambda = 41\,\%$.

The results of the ICRF modeling are summarized in Fig. 7.8. The power deposition profile estimated by TORIC-SSFPQL is slightly higher and more shifted to the HFS than the profile from TORIC-FFPMOD (cf. Fig. 7.8a). The LFS minority temperature profiles in Fig. 7.8b are rather similar, except the core value of the parallel temperature $T_{||}$ which is half in the TORIC-SSFPQL simulation. Because Dendy's model is not valid for $T_\perp/T_{||} \lesssim 1.5$, the minority temperature from TORIC-FFPMOD in such regions was expected to be equal to T_i of bulk ions. Consequently, the LFS temperature anisotropy from SSFPQL exceeds the FFPMOD by a factor of two as one can see in Fig. 7.8c. The temperature anisotropy from TORIC-SSFPQL is certainly overestimated, because assuming a finite value of $\mathcal{T}$ in Dendy's model and ICRF resonance on the HFS, the temperature anisotropy on the LFS calculated from Eq. (5.47) must fulfill:

$$\frac{T_\perp^*}{T_{||}^*} < \frac{1}{2}\frac{B_{\mathrm{ic}}}{B_{\mathrm{ic}} - B^*},$$

where asterisk indicates a quantity on LFS and B_{ic} is magnetic field at ion cyclotron resonance. This limit is shown in Fig. 7.8c by a dash-dotted line. Excessive value could indicate some limitation of the code for HFS code, however a detailed analysis is still in progress. Fig. 7.8c showed the experimentally measured and modeled poloidal asymmetry in the SXR radiation. A small centrifugal asymmetry is caused by the intrinsic plasma rotation. The model predicts the asymmetry driven by the trapped fast particles to occur on the LFS between $\rho_{\mathrm{tor}} = 0.18 - 0.4$, while the HFS asymmetry due to prevailing passing fast ions should be present further inside. The same observation was made, when the Monte Carlo ICRF code SELFO was applied for HFS heated discharge from JET tokamak [130]. Large inconsistencies show up, since TORIC-FFPMOD predicts a small asymmetry below the experimental uncertainty, while the asymmetry based on the TORIC-SSFPQL should be much larger due to the overestimated temperature anisotropy. Therefore, we conclude that the TORIC-FFPMOD model is consistent with our measurements, in contradiction to the TORIC-SSFPQL, which cannot predict realistic pitch distributions in the HFS heated case. A small difference between the centrifugal asymmetry and measurement at $\rho_{\mathrm{tor}} = 0.18 - 0.4$ can be caused by the overestimated plasma rotation measured during a NBI beam blip.

7.3. Parameter Dependence of the ICRF Driven Asymmetry

The impurity asymmetries can be used as a valuable tool to measure small perturbations in the poloidal electric potential and indirectly probe the fast particle distribution function. In order to experimentally investigate the parameter dependence of the observed poloidal asymmetries, a database of 10 AUG discharge was built. The database consists of all IC heated discharges with the clear HFS asymmetry from the years 2011–2016. Discharges were excluded, in which the low density together with LFS ICRF heating led to a locking of the core 1/1 mode, hence, preventing the measurement of the 2D tungsten asymmetry. Moreover, the measurements shortly after switch-on of ICRF and after sawtooth crashes were excluded, because the fast particle distribution requires a couple of tens of milliseconds to reach the stationary state. The largest asymmetries were usually produced only transiently, because the additional ICRF power often triggered the L-H transition, causing a significant increase in the plasma density.

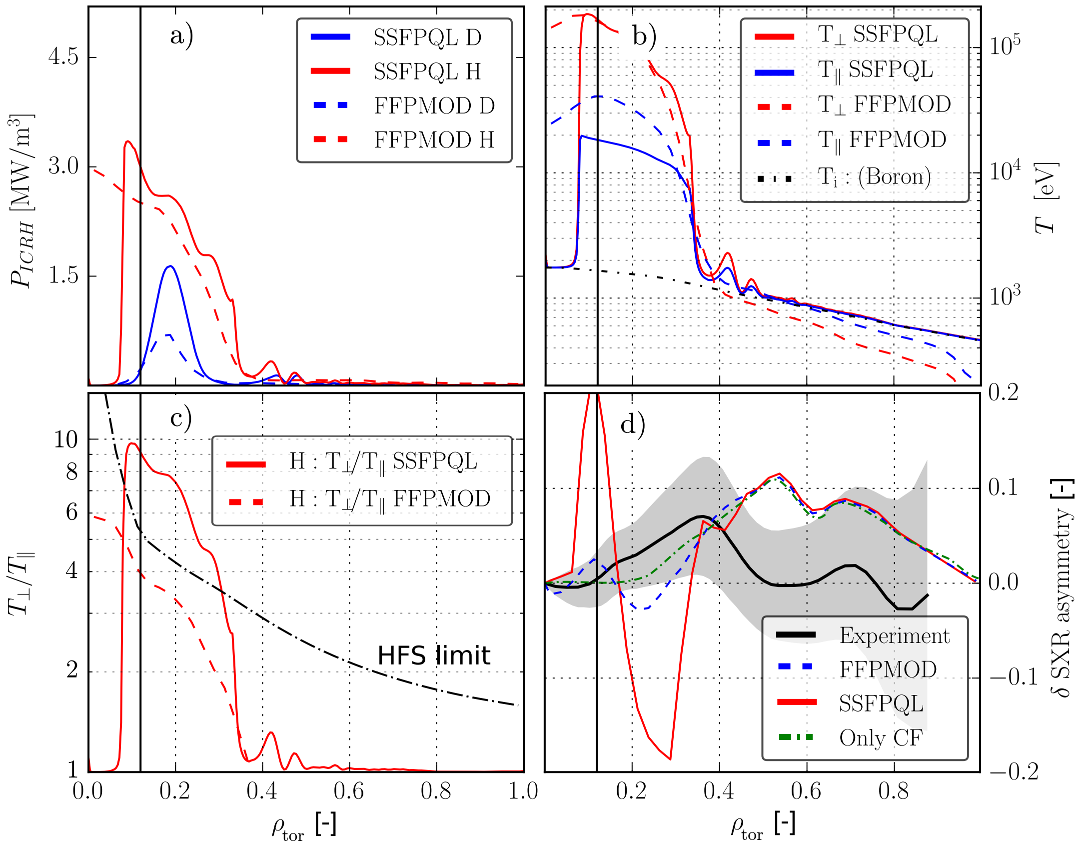

Figure 7.8.: The results of the ICRF modeling from the TORIC-SSFPQL and TORIC-FPPMOD code representing a) the heating power density, b) LFS minority temperature profile, c) LFS temperature anisotropy and d) the model of the W SXR radiation asymmetry, compared with the experimental observation.

Therefore, each discharge was split in 20 ms long sections and the temporal evolution of the background parameters enabled to extend the parameter range of the database. In order to study only the effect of the fast particles, the centrifugal asymmetry was subtracted according to Eq. (5.41).

In the numerical model presented in [131], the most relevant experimental parameters were identified as: $P_{\mathrm{IC}}, n_e, T_e, Z_{\mathrm{eff}}$ and the minority fraction f_m. Since the two last quantities, Z_{eff} and f_m are not routinely measured on AUG, we have to omit them from our study. Moreover, this ICRF modeling predicts an almost linear dependence of temperature anisotropy on the IC power, and thus the measured asymmetry was normalized by the heating power to remove this trivial dependence. The strongest correlation has been found with the electron density as depicted in Fig. 7.9a. The asymmetry is proportional to $\propto n_e^{-2}$ and this trend is well visible when the entire database is considered but even clearer within each group of the discharges. The deviation of discharges #32469 and #32470 (blue points) can be due to rather poor coupling of the IC power at low density and thus overestimated heating power used for the normalization of these discharges.

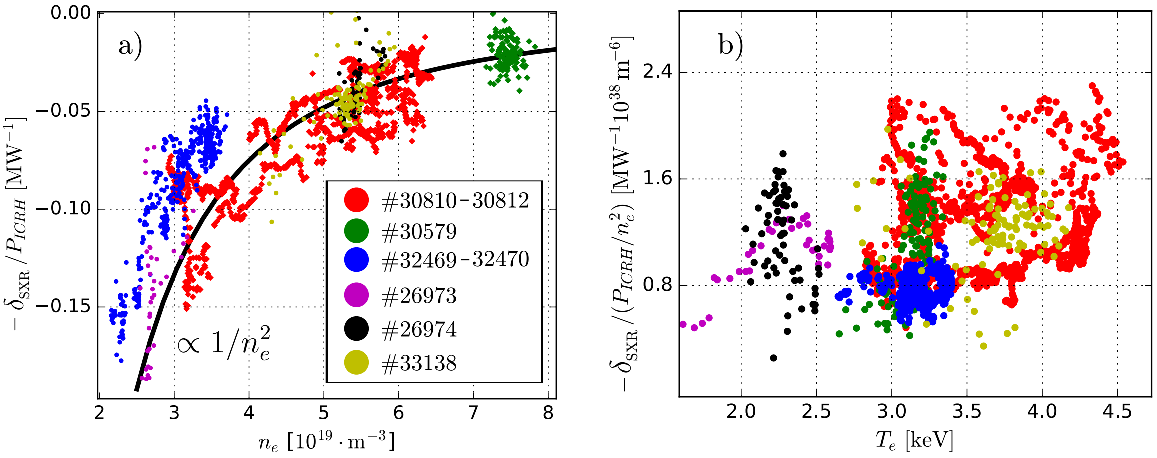

Figure 7.9.: Database analysis of the poloidal asymmetry driven by fast ions on n_e (a) and T_e (b). The black curve indicates the expected scaling $\propto n_e^{-2}$. The discharges from the same experiments with similar parameters are marked by identical colors.

The next quantity, considered in this study, is the electron temperature. The n_e scaling was removed by a further normalization with a factor n_e^{-2} as shown in Fig. 7.9b. However, the observed range of T_e is halve of the n_e range, and the scatter in the data is rather large. Therefore, if any dependence is present, it is a weak positive dependence, which can be explained by an increase of the tungsten ion change with the temperature.

Both these scalings are consistent with TORIC modeling performed in [131], where also a n_e^{-2} scaling and a weak temperature dependence has been predicted. The density dependence is caused by a reduction of the plasma collisionality, proportional to n_e and the simultaneously decreased number of minority ions, increasing the power per particle. Both effects together are responsible for the inverted square dependence on the electron density. The collisionality is also reduced by the increase of temperature since it scales as $T_e^{-3/2}$. However, the critical velocity for the pitch angle scattering is growing with T_e as well, canceling the net temperature dependence of the pitch angle scattering operator in the Fokker-Planck equation [132].

In Fig. 7.10a-d a parameter dependence scan of the tungsten poloidal asymmetry for the discharge #30812 evaluated using TORIC-FFPMOD results for the fast ions is depicted. Unlike the results in [131], where a linear dependence on ICRF power has been demonstrated, the power dependence of the asymmetry saturates for $P_{IC} \gtrsim 4\,\mathrm{MW}$. The dependence on the electron density scales also as $\propto n_e^{-2}$ for $n_e \gg 5\cdot 10^{19}\mathrm{m}^{-3}$, however the experimental dependence (dashed line in Fig. 7.10b) indicates a steeper growth for low density and two times weaker asymmetry for higher density. A similar discrepancy was observed with the TORIC-SSFPQL model as well. Finally, a change of the asymmetry with the minority fraction and Z_{eff} is indicated in Fig. 7.10c-d, and further investigation will be focused on the experimental verification of this dependence.

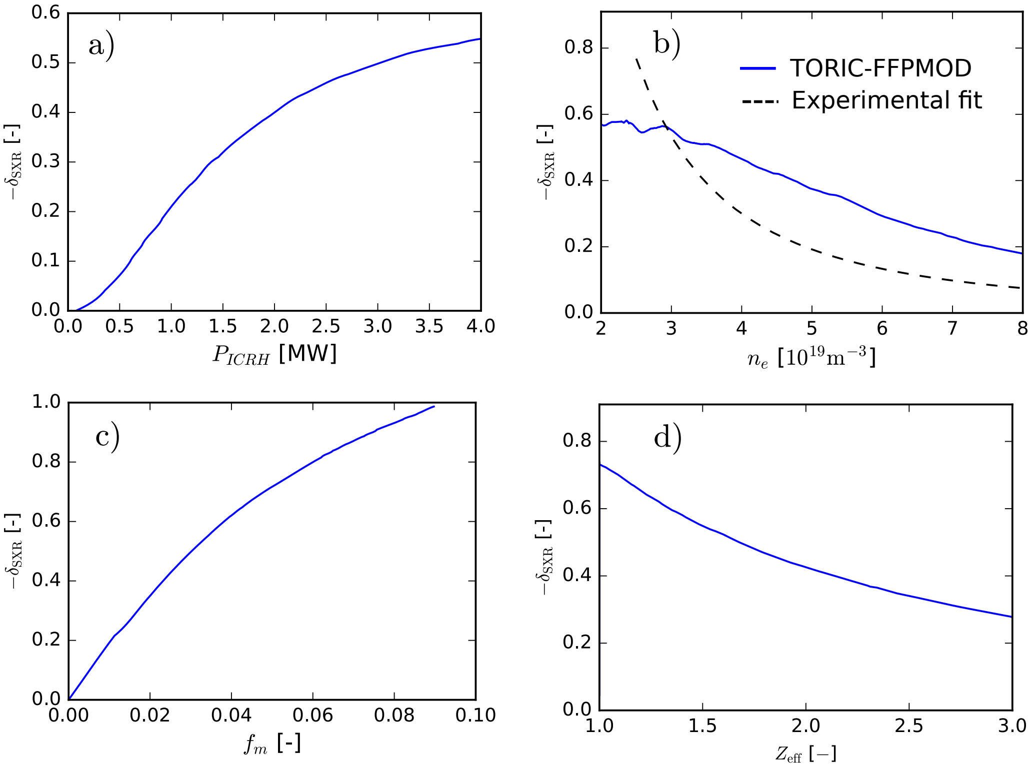

Figure 7.10.: Poloidal asymmetry of the tungsten SXR radiation modeled by TORIC-FFPMOD and Dendy's model as a function of a) ICRF power, b) electron density, c) minority fraction and d) effective charge. The other plasma parameters was set according to the discharge #30812 at 4.65 s (see Fig. 7.2).

7.4. Fast ions transport due to sawtooth crashes

One of pioneering applications of the measured poloidal asymmetries is the investigation of the fast particle redistribution by sawtooth crashes. The fast particle transport in AUG has been analyzed in [85], including the fast NBI deuterium ions further accelerated by ICRF. However, the fast hydrogen ions have a too low charge exchange cross-section to be detected by the fast ion D-alpha (FIDA) diagnostic, and the perturbation of the electrostatic potential is one of the few direct manifestations of these energetic ions in the plasma. Additionally, from the measured poloidal variation of the SXR radiation the poloidal variation of the minority fraction can be inferred from Eq. (5.41), which provide information about the pitch angle distribution [129].

The detailed examination of the asymmetry variation due to sawtooth crashes was performed on a subset of the database examined in the previous section. The subset consists of four discharges with large sawtooth crashes. In the database discharges #30811 and #30812, heated by 2.5 MW of NBI and 4.3 MW of ICRF and discharges #32469 and #32470 heated by a 2.5 MW of ICRF were included. All discharges had the same value of the plasma current $I_p = 1\,\mathrm{MA}$, a moderate value of the edge safety factor $q_{95} = 4.5$, and low electron densities between 2–$6{\cdot}10^{-19}\,\mathrm{m}^{-3}$. The sawtooth crashes had a similar size with their inversion radius estimated from T_e measurements to be about $\rho_{\mathrm{tor}}^{\mathrm{inv}} = 0.4$. The largest difference between the discharges was observed in the sawtooth period duration. The fast rotation and high pressure of the passing fast NBI ions in discharges #30811 and #30812 increased the sawtooth period to 110 ms. The sawtooth period in the discharges #32469 and #32470 was only 30 ms with a 5 ms long precursor and post-cursor phase.

The change in the poloidal asymmetry caused by the sawtooth crash, corrected for the centrifugal asymmetry using Eq. (5.41) is depicted in the upper row of Fig. 7.11 for the first large sawtooth crash after switching on the ICRF. A significant reduction of the asymmetry after the crash can be observed in the discharges #30811 and #30812, while the asymmetry in the discharges #32469 and #32470 is almost unaffected. In the lower row of Fig. 7.11, the FIDA signal normalized to the signal from the beam emission spectroscopy (BES) for the same crash is shown. The FIDA data are available only for discharges #30811 and #30812, where beam Q3 was used and the measurements demonstrate a flattening of the peaked fast NBI ions profile.

The same conclusion can be drawn from Fig. 7.12, where the fast particle asymmetry was evaluated from the SXR asymmetry for each sawtooth crash. While in the discharges #30811 and #30812 a 20–30 % reduction of the poloidal asymmetry was observed, the change in the discharges #32469 and #32470 was below 10 %, despite the large magnitude of the observed asymmetry. The cause of this difference is in the sawtooth activity and lower ICRF power. The long sawtooth period of 110 ms and 4.3 MW of the ICRF power in discharges #30811 and #30812 caused a peaked temperature anisotropy profile close to the IC resonance. The particle distribution was then strongly affected by the enhanced transport during each sawtooth crash. For the discharges #32469 and #32470, the 30 ms long sawtooths period was significantly shorter than the anisotropy relaxation time $\tau_{aniso} \approx 150\,\mathrm{ms}$ estimated using the FFPMOD code. Consequently, the peaked temperature anisotropy profile cannot built- up before the next sawtooth crash and the asymmetry stays almost unaffected.

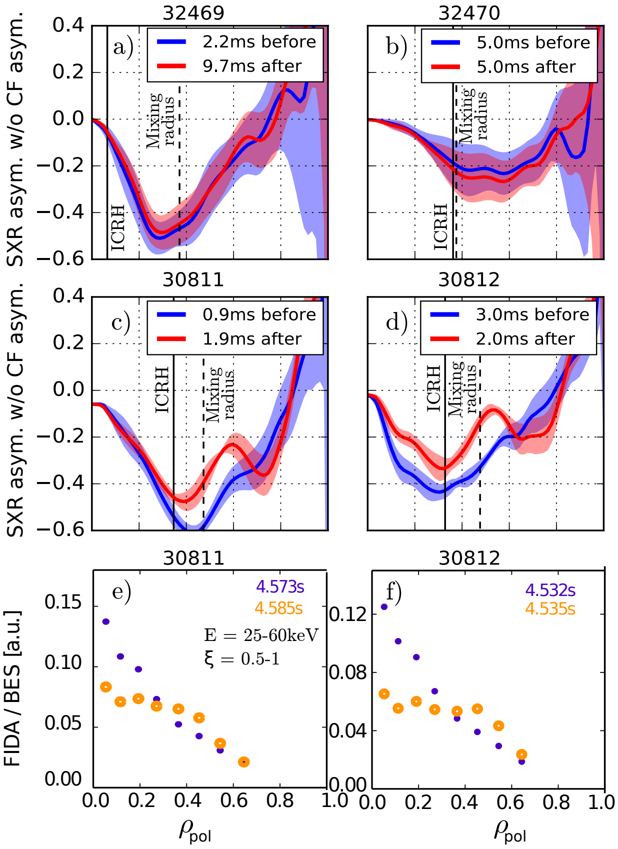

Figure 7.11.: a–d) The change in the asymmetry profile evaluated for the first sawtooth crash after switching of ICRF. The centrifugal asymmetry before and after the crash has been removed according to the Eq. (5.41). e–f) The signal from the fast ion D-alpha diagnostic (FIDA) for the energy range 25–60 keV and pitch range 0.5–1, normalized to the beam emission spectroscopy (BES) signal for each LOS of discharges #30811 and #30812.

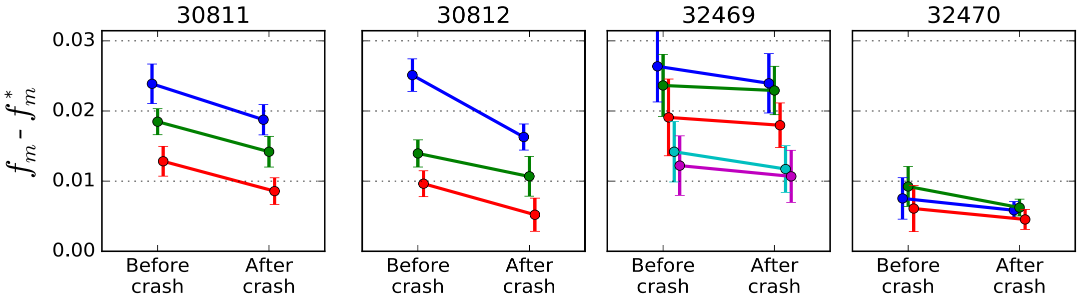

Figure 7.12.: Reduction in the poloidal asymmetry of the minority ions $f_m - f_m^*$ during a sawtooth crash evaluated for all major crashes within ICRF phase of the each discharge. Each crash is depicted by a separate color.

7.5. Conclusions

In this chapter, the first evidences of ICRF driven poloidal asymmetries in the tungsten density on AUG were presented. High-resolution SXR emissivity profiles were employed for detailed validation of the parallel force balance of heavy impurities and the fast minority ions accelerated by ICRF. The response of the accelerated ions was modeled using the the TORIC code coupled with the FFPMOD and the SSFPQL Fokker-Planck solvers, and interpreted using Dendy's model (Eq. (5.45)).

A very good match between the experimentally measured and the modeled asymmetry was found in the detailed investigation of a low-density discharge with ICRF heating on the low-field side. On the contrary, a discrepancy has been observed when a high-field side heated discharge was examined. It was shown that the temperature anisotropy from TORIC-SSFPQL was slightly overestimated, and consequently the modeled poloidal asymmetry exceeded the experimentally measured value. Such a discrepancy could indicates limitation of the particle trapping model in SSFPQL. In the contrary, TORIC-FFPMOD provided results consistent with the measurement.

Further investigations focused on studying the fast particles content in ICRF heated plasmas. A database was analyzed to identify the most relevant parameters determining the poloidal asymmetries. Inverse squared electron density and weak electron temperature scaling was found, consistently with the physical expectation based in the Fokker-Planck equation. The influence of the electron density and temperature was found consistent with the physical expectation. However, the comparison with TORIC-FFPMOD a significant discrepancy for the moderate density cases ($n_e > 4 \cdot 10^{19}\mathrm{m}^{-3}$), where the modeled asymmetry exceeded the experiment by about a factor of two. The cause of this discrepancy is unknown and modeling using alternative ICRF codes will be necessary.

Finally, the poloidal asymmetries were used to examine the fast particle redistribution during sawtooth crashes. Two similar groups of discharges were investigated with a significantly different sawtooth period. When the sawtooth period was much shorter than the typical fast particles relaxation time, the fast particle distribution was kept flat by frequent crashes, and the asymmetry was almost unaffected. On the other hand, slow sawtooth crashes resulted in a periodical peaking of the trapped fast particles close to the ICRF resonance and the crash reduced the asymmetry by 20–30 %, confirming the significant effect of the sawtooths on the fast particles transport.

In conclusion, the measurement of the heavy ions poloidal asymmetries provides a stringent test beneficial for validation of the ICRF heating codes. The discrepancies observed in the high density, and HFS heated case motivates for a further development of these codes. Moreover, the understanding of the poloidal asymmetries is critical for the prediction of neoclassical transport, as will be demonstrated in the next chapter.

8. Influence of Asymmetries on Radial Impurity Transport

This chapter is devoted to the investigation of radial transport in the presence of poloidal asymmetries in the heavy ion density. The experimental evidence of these effects is relatively scarce. Probably the first experimental observation was accomplished in a Z-scaling investigation of R. Dux [117] since the magnitude of the observed transport significantly exceeded the neoclassical values and the largest difference was present for the heaviest ions with a significant centrifugal asymmetry. An alternative approach was applied in [116], where complex modeling of the neoclassical and turbulent transport including the centrifugal effects had provided stationary W density profiles in agreement with the experiment. And finally, the plasma rotation scan in the JT-60U [133–135], MAST [136] and TFTR [137, 138] tokamaks revealed a strong dependence of the core impurity density on the rotation velocity and direction.

In the first part of this chapter, results of the impurity transport analysis are presented, directly demonstrating the change in the magnitude of the particle flux due to the poloidal asymmetry. Further, the neoclassical transport coefficients are evaluated using the NEO code [60] and the parameter dependence is investigated. Finally, the experimentally measured transport coefficients is compared with neoclassical values from NEO, and the results are discussed.

8.1. Transport Enhancement due to In-Out Asymmetry

The experimental verification of the change in the neoclassical transport due to asymmetries is a challenging problem. Despite the expected increase in the magnitude of the neoclassical flux (see Sec. 5.3.2), which may be an order of magnitude, the ratio between diffusion and drift velocity stay almost constant.

The stationary normalized gradient of the impurity density profile is expressed as

$$\frac{\nabla n_z}{n_z} = \frac{V_{neo}}{D_{neo} + D_{turb}}, \tag{8.1}$$

assuming that $V_{turb} \ll V_{neo}$. In the plasma center, where $D_{neo} \gg D_{turb}$, the stationary gradient of the density profile is almost unaffected. Further outside, where $D_{neo} \lesssim D_{turb}$, $\nabla n_z / n_z$ can be affected since D_{turb} is much less enhanced by the asymmetry than the neoclassical coefficients. However, the comparison with the experimental value of the gradient would depend very much on an the quality of the modeling of the turbulent flux close to the core, which has a low fidelity. Moreover, the poloidal asymmetries are generated by heating sources. Therefore, in order to change the asymmetry, the heating profile can be affected, directly modifying the turbulent flux and gradients of the background kinetic profiles. Our first experimental attempts focused on the ICRF driven asymmetries. The transition between the LFS and HFS ICRF resonance was realized by the change of the generator frequency. This should modify the asymmetry without the variation in the heating profile. However, a transient behavior, a variation in the MHD activity and a high fraction of core electron heating destabilizing turbulences [139] made our scenario unsuitable for a measurement of the transport coefficients. Therefore, our next attempt had been aimed at the NBI-only heated discharges without additional core electron heating.

The experiment best suited to such analysis is provided by the set of L-mode discharges investigated in Sec. 6.2. A switching between the NBI sources caused significant changes in the poloidal asymmetries, while the other parameters were almost unaffected. Moreover, large regular sawtooth crashes were present in these discharges, allowing for the evaluation of the central transport parameters by analyzing the temporal and spatial evolution of the tungsten density profile during each sawtooth cycle.

8.1.1. Experiment Description

The most promising discharge from the experiment introduced in Sec. 6.2 is #32324 because the change in the plasma parameters and sawtooths period between the phase with more parallel Q3 and more radial Q4 NBI sources (see Fig. 2.2a) was the smallest. At first, the plasma profiles in this discharge are examined to verify that the switching between Q3 and Q4 beam sources did not influence the other transport mechanisms except the poloidal asymmetry. The main plasma profiles are depicted in Fig. 8.1, where the blue lines correspond to the Q3 phase and the red line to the Q4 phase. The ion and electron temperature T_i and T_e are reduced in the Q4 phase by 25 % and 10 % respectively, but the normalized temperature gradients remain the same inside of $\rho_{\mathrm{tor}} = 0.3$. The electron density n_e is gradually increasing during the whole discharge and therefore it is about 20 % higher in the later Q4 phase than in Q3 phase. Moreover, n_e profile is slightly more peaked in the Q3 phase. Since the n_e measurements inside $\rho_{\mathrm{tor}} = 0.15$ are only an extrapolation due to a broken central DCN interferometer line of sight, a definitive statement about the core electron density gradients cannot be made.

In Fig. 8.1c, the electron and ion heating profiles Q_e, Q_i and the particle source $S_{b,tot}$ are depicted as calculated by TRANSP. The core electron heating Q_e is about 70 % higher in the Q4 phase due to a difference in the electron temperature and collisionality, while the ion heating Q_i is almost the same. The particle source $S_{b,tot}$ in the Q3 phase is more peaked with 20 % higher central value which could be a reason for the slightly higher density gradients in the core. The ion heat diffusion coefficient χ_i^{PB} in Fig. 8.1d calculated from the power balance and its neoclassical values χ_i^{neo} are almost unaffected, indicating a negligible change in the heat transport. The shape of the tungsten density profiles in Fig. 8.1e is very similar in each phase, however, the magnitude is 50 % higher in the Q3 phase. This difference can be a consequence of the reduced W influx inferred from the intensity of the W I line [140]. We have observed a decrease by 50 % possibly caused by an increased edge electron density reducing W sputtering at the wall. The profiles in Fig. 8.1f correspond to the poloidal asymmetry, which was reduced from highly asymmetric to almost symmetric by switching from the parallel Q3 source to the more perpendicular Q4. The MHD activity was almost unaffected. The average sawtooths period in the Q3 phase was about 100 ms and 80 ms in the Q4 phase. In conclusion, the change of the investigated plasma parameters is relatively small with weak impact on the radial transport except for the major variation of the poloidal asymmetry.

Since the temporal evolution of the plasma parameters is essential for the transport analysis, it is necessary to investigate the time-traces during the buildup phase of a sawtooth oscillation. The average sawtooth period was about 100 ms in the Q3 phase, while in the Q4 phase it was about 80 ms. The ion and electron temperature, electron and tungsten density and MHD activity are depicted for a single sawtooth cycle in the Q3 and the Q4 phases in Fig. 8.2. The sawtooth crash caused almost a complete flattening of all profiles due to an increase in the central transport. During the sawtooth period, the central electron temperature is raised by 30 %, T_i by 40 %, the electron density by 20 % and the tungsten density by almost two orders of magnitude. Consequently, during the sawtooth cycle very steep radial gradients in the W density are building up. Moreover, time evolution of the n_i and T_i gradients have a significant impact on the neoclassical pinch. The tungsten evolution is significantly affected by the sawtooth post-cursor visible in the spectrograms of the core SXR LOS in Fig. 8.2. Therefore, the first 20–40 % of the sawtooth cycle had to be omitted from the further analysis. The post-cursor activity was stronger in the Q3 phase, causing transient negative radial gradients in n_W close to the $q = 1$ surface. Further, at the very end of each sawtooth cycle, the sawtooth pre-cursor occurred, affecting the measured tungsten emissivity profile by displacing the magnetic axis and smearing the sharp radiation peak via fast oscillation. The effect of the fishbone instability driven by the fast NBI ions was negligible.

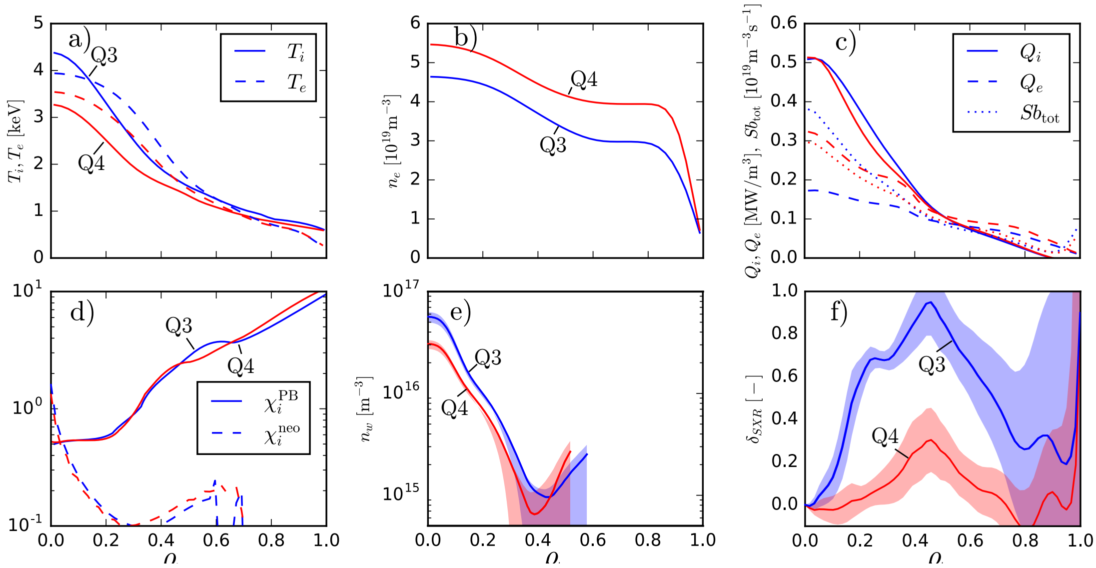

Figure 8.1.: The profiles of various plasma quantities for the Q3 heated phase (blue) and the Q4 heated phase (red): a) the average ion and electron temperature before the sawtooth crash, b) average electron density before the crash, c) average ion (full line) and electron (dashed line) heating profile and particle source (dotted line), d) ion diffusion coefficient from power balance (full line) and the neoclassical value (dashed line) e) poloidally average tungsten density before the crash derived from the SXR profile, f) poloidal asymmetry profile as derived from SXR emissivity.

8.1.2. Methods for Transport Analysis

The transport coefficients are often estimated using three methods: the gradient-flux (GF) method [142], the least-squares (LSQ) optimization method [143] and matricial approach derived in [144] searching for a solution in the Fourier domain. Since a determination of the transport coefficients v and D is a rather difficult task which may strongly depend on the used methodology, two of these methods, GF and LSQ, were utilized to improve the fidelity of our results. Both methods were newly developed and carefully tested for the purpose of this study and a brief description follows.

Gradient-flux (GF) method

The transport equation (5.12) expresses a linear relation between the normalized flux Γ_z/n_z and the normalized impurity gradient

$$\frac{\Gamma_z(r,t)}{n_z(r,t)} = -D(r)\frac{1}{n_z}\frac{\partial n_z(r,t)}{\partial r} + v(r) \qquad \forall r,t. \tag{8.2}$$

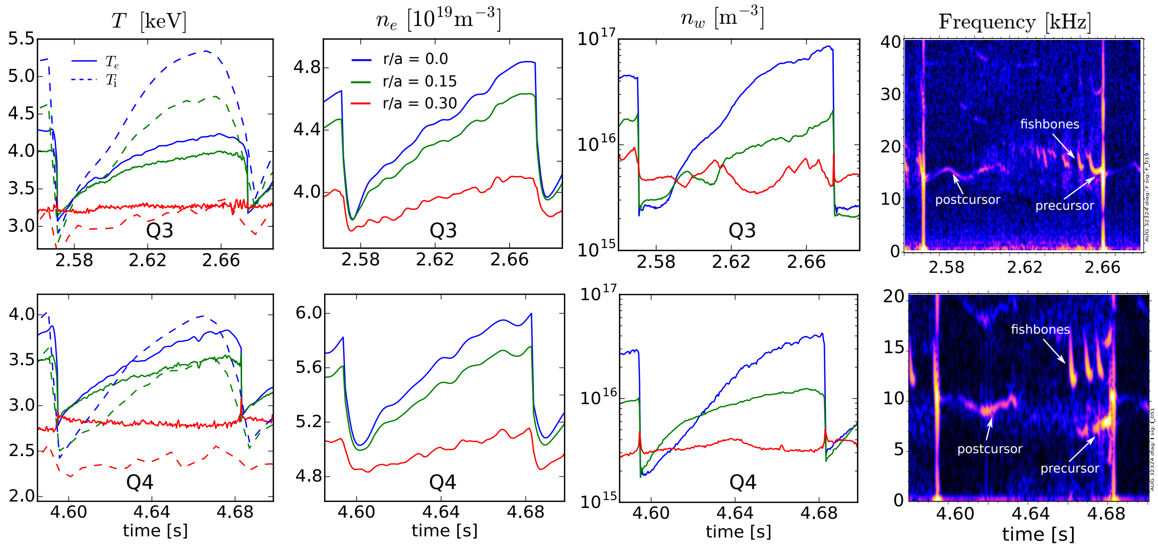

Figure 8.2.: The temporal evolution of the ion and electron temperature, electron density, tungsten density and MHD activity spectrogram for a single sawtooth cycle from the Q3 phase (up) and Q4 phase (bottom) depicted for discharge #32324. The measured profiles were fitted by smooth 2D spline with breaks at the time of the sawtooth crash [141].

The linear fit of flux vs. gradient using orthogonal regression then provides the diffusion coefficient $D(r)$ and the drift velocity $v(r)$. The fidelity of the fit is low because experimental determination of the D depends on the second time derivative of the measured impurity density and the first time derivative of the normalized density gradient. Due to the ill-possed nature of this task, additional regularization is necessary. Therefore, we have parametrized D using a two-knot cubic spline designed to be even and positive and v/D by an odd four-knot cubic spline, where positions and values of the knots were considered as free variables. This constrained linear fits of the transport coefficients were thus optimized for all positions simultaneously in order to maximize the likelihood of the fit of the flux and gradient for all radial positions at once. The uncertainty of the splines was estimated by propagation of the covariance matrix of the knot values to the final profiles of v and v/D.

Least squares (LSQ) method

The LSQ method is based on a direct solution of the equation (5.12) and comparison with the measured impurity density. The solution of the diffusion-convection equation was found by the Crank-Nicolson scheme using the discretization method adopted from STRAHL [62]. The initial condition is defined by the density profile shortly after the sawtooth crash, while the impurity density at $\rho_{\mathrm{tor}} = 0.3$ served as boundary condition. In order to find D and v/D compatible with the experiments, these coefficients need to be modified until a solution $n_z(r,t)$ matching the measurements is found. This is achieved via χ^2 minimizing procedure, where χ^2 is defined as

$$\chi^2 = \sum_r \sum_t \left(\frac{n_{t,r}^{exp} - n_{t,r}^{model}}{n_{t,r}^{err}} \right)^2 ,$$

$n_{t,r}^{exp}$ is the W density derived from SXR, $n_{t,r}^{model}$ is the solution of the diffusion equation and $n_{t,r}^{err}$ is the uncertainty of the experimental data. Since the optimization requires a large number of model evaluations, a short computing time is critical. Our implementation was able to evaluate n^{model} in 4 ms, while STRAHL, which also solves the ionization and recombination balance for each W ion, requires at least several seconds. The D and v/D coefficients were described by spline curves as for the GF method, and the values best matching the experimental density profiles were searched by the Levenberg-Marquardt algorithm. This optimization task is highly nonlinear and non-convex and finding the global optimum is a highly non-trivial problem. Therefore, the parameters of the spline were constrained in order to avoid nonphysical solutions and to reduce the dimensionality of the parameter space. Moreover, to avoid being trapped in local minima, a good initial guess was necessary.

The LSQ based method is more robust with respect to the experimental uncertainties than the GF method because the solution intrinsically fulfills the particle conservation law. On the other hand, it is more sensitive to the assumption of constant transport coefficients during the investigated period and also the uncertainty of the boundary and the initial condition.

8.2. Impurity Perturbations by Sawtooth Crashes

In order to estimate the transport coefficient by the LSQ and GF methods, it is necessary to produce a substantial perturbation in the impurity flux Γ_z and study the dynamic response of the impurity density profiles. Such perturbation can be generated externally by a laser blow-off [145], gas puff injection [146] or continuous harmonic source like ICRF [13]. The other option is to investigate perturbations in the intrinsic or injected impurity density generated by the sawtooth crashes [117] or a hybrid approach, where the external and internal perturbations are employed to improve accuracy over the whole plasma radius [147].

The discharge #32324 presented in Sec. 8.1.1 is well suited for the transport analysis during sawtooths cycles. The flattening by sawtooth crash and the following build-up phase, increasing the core W density by almost two orders of magnitude, generates sufficient variation in the impurity flux to estimate transport coefficients with reasonable accuracy. Additionally, a large number of the sawteeth provides the necessary statistics to assess the significance of the measured changes in the transport. On the other hand, this method cannot be used to infer the W transport coefficients outside of the sawtooth inversion radius ($\rho_{tor} \approx 0.26$), because there the change of the flux is too small, while the uncertainty in the W density is significantly increased.

The interpretation of the inferred transport coefficients must be made with caution because the assumption of temporally constant transport coefficients applied in the transport analysis methods is not necessarily fulfilled. Since the gradients of T_i and n_i are evolving during a sawtooth cycle, the transport coefficients will evolve as well. The impurity pinch (Eq. (5.25b)) will increase from zero after the crash when all the profiles are flattened to the largest value at the end of the sawtooth cycle when the profiles are the most peaked. As D can be interpreted as a^2/τ, for the same characteristic length a, D is proportional to an inverted timescale τ of the transport process. We can describe a sawtooth crash by two coupled recovery processes. The first applies to the background and the second to the impurity density. The effective diffusion coefficient of this coupled process is given by

$$D_{\mathrm{eff}}^{-1} \approx D_W^{-1} + D_0^{-1}, \tag{8.3}$$

where D_0 is diffusion coefficient of the background. If the tungsten diffusion coefficient D_W is significantly smaller than the background diffusion coefficient D_0, i.e. $D_W \ll D_0$, the measured diffusion coefficient D_{eff} will correspond to the average of D_W during the investigated period. However, if $D_W \gg D_0$, the tungsten density profile will be in the equilibrium with the background and the timescale of the tungsten evolution will depend solely on D_0 and therefore D_{eff} will underestimate the real value of D_W. Unfortunately, D_0 cannot be properly measured, due to the lack of core electron density measurements. We have to accept that the largest measured values of D_{eff} can underestimate the real D_W. On the other hand, the equilibrium value of the drift coefficient v/D will be unaffected.

8.2.1. Evaluation of the Transport Coefficient

The transport analysis was performed for each sawtooth within the constant phase of the current flattop in the discharge #32324. The beginning of the sawtooth cycle, influenced by the post-cursor was removed, and the quality of the data fits by the GF and the LSQ methods were carefully verified for each build-up phase. Fig. 8.3 shows the transport coefficients evaluated from the two sawtooth cycles presented in Fig. 8.2. The radial profiles obtained from the GF and the LSQ methods are rather similar, demonstrating the consistency between the results obtained with these two methods.

Apparently, the diffusion coefficient for the sawtooth crash during the Q3 phase (cf. Fig. 8.3a) is significantly larger than the coefficient estimated in the Q4 phase (Fig. 8.3d). On the other hand, the drift coefficients v/D in Fig. 8.3d,e have a similar shape and magnitude. This is consistent with the previous observation of the self-similar tungsten density profiles in both phases (cf. Fig. 8.1f).

The transport coefficients for each sawtooth cycle are depicted in Fig. 8.4. The values were evaluated close to the minima of the drift coefficient at $\rho_{\mathrm{tor}} = 0.12$, because there was also the largest change in the normalized particle flux and thus higher credibility of the results. The diffusion coefficient is significantly reduced from about $D_W = 0.2$–$0.4\,\mathrm{m}^2/\mathrm{s}$ in the Q3 phase to $D_W = 0.03$–$0.08\,\mathrm{m}^2/\mathrm{s}$ in the Q4 phase indicating a substantial impact of the poloidal asymmetry on the radial transport. Moreover, the LSQ method predicts slightly lower values of D_W in the Q4 phase than GF method. The drift coefficient v/D is in both phases between -20 and $-40\,\mathrm{m}^{-1}$ as is depicted in Fig. 8.4b. Also, in this case, a few points in the Q4 phase estimated by the LSQ method significantly deviate from others, which is a consequence of an underestimated D_W since D_W and v/D are correlated for small values of D_W. Otherwise, both methods typically match within the error bars.

8.2.2. Uncertainty Analysis

The estimation of the uncertainty in the transport parameters is not a trivial task due to the error propagation from the SXR tomography, the T_e, n_e profiles and the atomic data to n_w and further propagation to the strongly regularized transport coefficients. The tungsten cooling factor L_W grows almost linearly with T_e in the relevant temperature range between 2.7–4 keV (cf. Fig. 8.2). Since T_e was changing in the examined regions by about 30 %, the uncertainty in L_W should not significantly affect the W density varying by two orders of magnitude. Moreover, the transport coefficients are independent of the error in the scaling factor of the impurity density. The same argument is valid for n_e, changing by only 20 % during the sawtooth cycle. The main uncertainty in n_W thus comes from the SXR tomography. The radial resolution of the tomography is limited by the width of the LOS. A typical value for the LOS width in the plasma core is $\Delta\rho_{\mathrm{tor}} \approx 0.1$ (cf. Fig. 4.1), resulting in the resolution of the radial gradients down to $\Delta\rho_{\mathrm{tor}} \approx 0.2$, which is a rough guess of the maximal spatial resolution of the transport coefficients. The expected uncertainty in the W density estimated from all previous contributions is about 20 %.

The optimization problem solved by the LSQ and the GF method is in principle highly overdetermined because 12 free parameters of the transport coefficients are determined from $n_r \times n_t \sim 30 \times 200$ measurements. However, the dependence on the temporal and spatial gradients and a correlation of v/D and D makes this problem also very

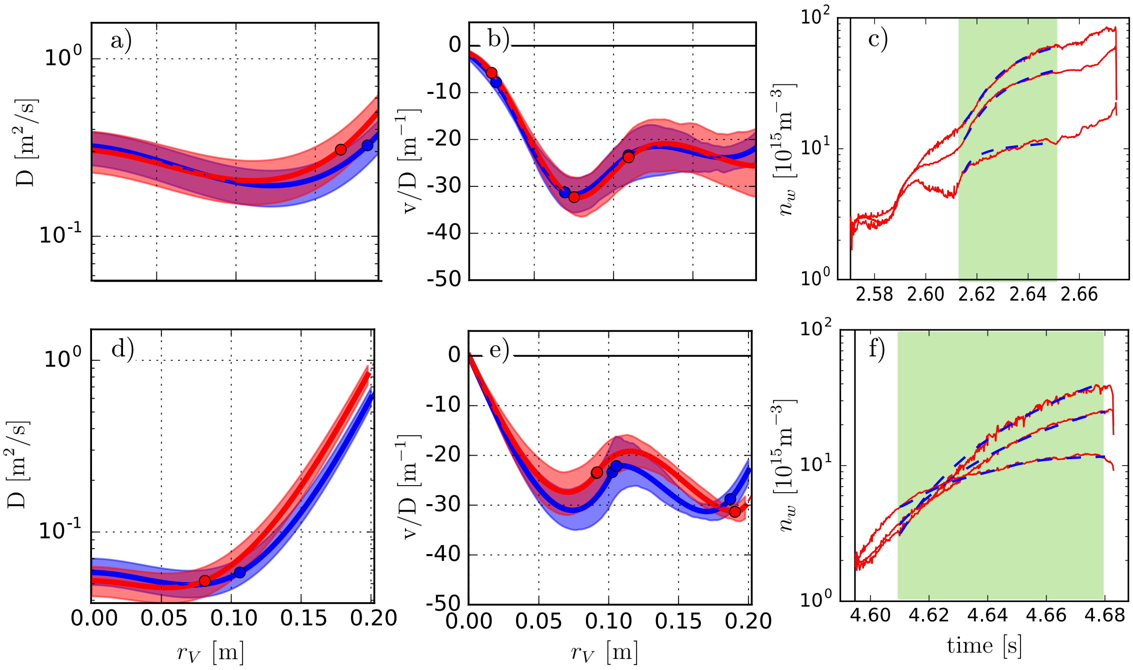

Figure 8.3.: The transport coefficients estimated from the discharge #32324. The plots a–c) describe the sawtooth at 2.6 s and d–f) represent profiles for a sawtooth at 4.6 s. The diffusion coefficient D_{eff} is depicted in a, d, the drift coefficient v/D in d, e and the W density n_w in plots c,f). The blue profiles corresponds to the LSQ method, while the red ones to the GF method. The dots are the spline knots. The green area in plots c) and f) indicate the region selected for the analysis, the blue lines show the measured W densities at $r_V = 0,\ 0.1,\ 0.2\,\text{m}$ (r_V defined at (5.5)) and the blue dashed line correspond to fits by the LSQ method.

ill-conditioned. The confidence intervals of the transport parameters were determined by propagation of the uncertainty described by the covariance matrix of the spline knots to the final profiles. The confidence intervals, therefore, represent only the statistical error, but the bias and other non-statistical errors also play a substantial role.

8.3. Neoclassical Transport Modeling

In the following, it is investigated, whether the measured transport can be explained by the neoclassical theory extended for the poloidal asymmetries using the NEO code. The analytical formulas introduced in Sec. 5.3.2 are valid for trace impurities deep in the Pfirsch-Schlüter regime and bulk ions in the banana regime. However, such conditions cannot be reached in AUG plasmas; therefore, the results of NEO will be used instead. The output of NEO is a radial particle flux Γ_z which for a trace impurity z represents a linear function of n_z, n_i and T_i gradients (see Eq. (5.25)). The transport

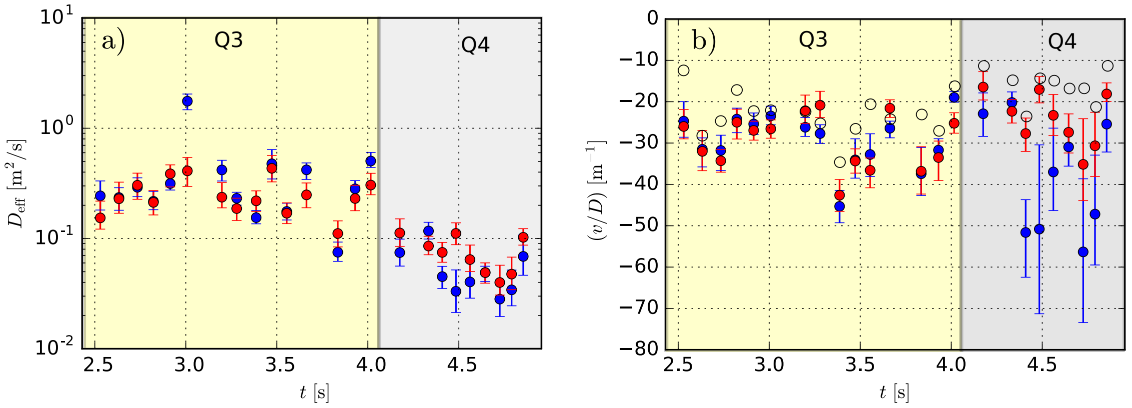

Figure 8.4.: Temporal evolution of a) D_W and b) v/D in the discharge #32324 at $\rho_{\mathrm{tor}} = 0.12$. Blue points correspond to the LSQ method, red to the GF method, open black circles to evaluated $\nabla n_w / n_w$ shortly before before sawtooth crash. The yellow shaded area was heated by the beam source Q3 and the gray shaded area by the beam source Q4.

coefficients are thus calculated in the following way

$$D_z = \frac{\partial \Gamma_z}{\partial \nabla \langle n_z \rangle} \qquad v_z = \frac{\Gamma_z|_{\nabla n_z = 0}}{\langle n_z \rangle} \tag{8.4}$$

Additionally, the T_i and n_i peaking factors called P_T and P_n will be defined by the following decomposition:

$$\frac{R\Gamma_z}{\langle n_z \rangle} = D_z \left(\frac{R}{L_{\langle n_z \rangle}} + Z P_n \frac{R}{L_{n_i}} + Z P_T \frac{R}{L_{T_i}} \right) \tag{8.5}$$

and the peaking factors are evaluated from NEO flux as:

$$P_n = \frac{1}{Z D_z} \frac{\partial v_z}{\partial \nabla \ln n_i} \qquad P_T = \frac{1}{Z D_z} \frac{\partial v_z}{\partial \nabla \ln T_i}. \tag{8.6}$$

8.3.1. Influence of the Poloidal Asymmetry

The simulations were evaluated for the plasma parameters of the discharge #30812 at $\rho_{\mathrm{tor}} = 0.3$ (cf. Fig. 7.2) and an asymmetry scan was performed by varying the centrifugal force via the Mach number, while the counteracting electric force from the fast particle asymmetry was kept constant. The results of this asymmetry scan are represented by the D_W coefficient (cf. Fig. 8.5a). The stationary profile is determined by the peaking coefficients P_n and P_T which are shown in Fig. 8.5b. P_n can be interpreted as n_i peaking efficiency and the negative value of P_T describing the T_i screening efficiency. The diffusion coefficient and thus also the magnitude of the neoclassical flux reaches a minimum for a slightly negative poloidal asymmetry δ equal to $\delta/\varepsilon \approx -1$, where ϵ is the local inverse aspect ratio. Around the minimum, the value of D_W grows linearly with the asymmetry. Such dependence can be described by an empirical approximation valid for low collisionality of the form

$$D_W(\delta) = D_c + (D_W(0) - D_c)|1 + \delta/\varepsilon|, \tag{8.7}$$

where D_c is the classical diffusion coefficient. Finally, the dashed line in Fig. 8.5a indicates the analytical solution in Pfirsch-Schlüter regime Eq. (5.53). The minimum is reached at $\delta/\varepsilon \approx -2$ and the neoclassical flux is growing quadratically, with a much steeper dependence than that calculated by NEO.

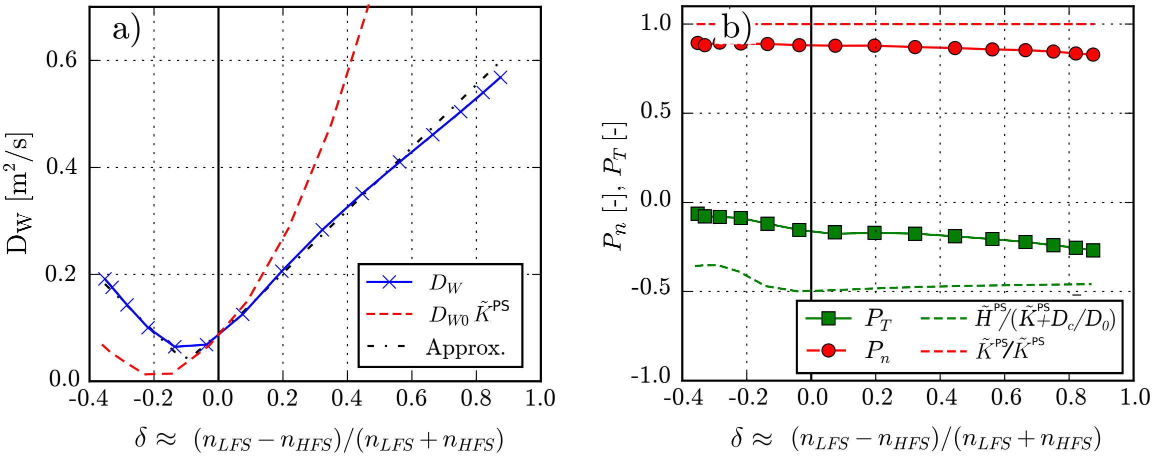

Figure 8.5.: a) Values of the tungsten diffusion coefficient D_W evaluated by NEO for various values of the poloidal asymmetry. Full line corresponds to the NEO calculation for discharge #30812 at $\rho_{\mathrm{tor}} = 0.3$ ($\varepsilon = 0.1$), the dashed line is based on the analytical solution for the Pfirsch-Schlüter (PS) regime and the dash-dotted line is a simple approximation (Eq. (8.7)). b) Red points correspond to the density peaking coefficient P_n and green to the temperature peaking coefficient P_T, while the dashed lines are a approximation based on factors $\tilde{H}^{PS}$ and $\tilde{K}^{PS}$ introduced in Eq. (5.53). To avoid the singularity of $\tilde{H}/\tilde{K}$ at $\delta/\varepsilon = -2$, classical diffusion D_c was added.

In Fig. 8.5b, the impact of the tungsten poloidal asymmetry on P_n is almost negligible. On the contrary, P_T shows a significant change for $\delta/\varepsilon <$ -1, causing a substantial reduction of the T_i screening efficiency as due to a change of the sign in the contribution of the trapped bulk ions. Also, in this case, the analytic approximation (5.53) matches the shape, but the magnitude is too large.

8.3.2. Influence of Collisionality

The collisional regime of the bulk ions represents an important parameter in neoclassical theory. Therefore, a collisionality (ν^*) scan was performed to investigate the change in particle flux. The D_W coefficient grows monotonously with the collisionality for the case of non-negative asymmetry as it is shown in Fig. 8.6a. However, a clearly different trend is present for a negative asymmetry. It is caused by a shift of the D_W minimum from value $\delta_{min}/\varepsilon \approx -1$ for W ions in the plateau regime to the value $\delta_{min}/\varepsilon \approx -2$ for W ions in the Pfirsch-Schlüter regime ($\nu^* \gg 1$). Large changes can be observed also in the P_T coefficient (cf. Fig. 8.6b). When the bulk ions are deep in the banana regime ($\nu^* \ll 0.03$), P_T is about $-1/3$, independently of the asymmetry. The increase of the Pfirsch-Schlüter flow fraction towards higher collisionality enhances the T_i screening in the case without asymmetry, and P_T converges to $-1/2$ [68]. The presence of positive asymmetry reduces the T_i screening, and negative asymmetry can even reverse the flow direction. Then both, n_i and T_i gradients will drive inward impurity convection. Such conditions can occur at the edge of the plasma as it was discussed in [148].

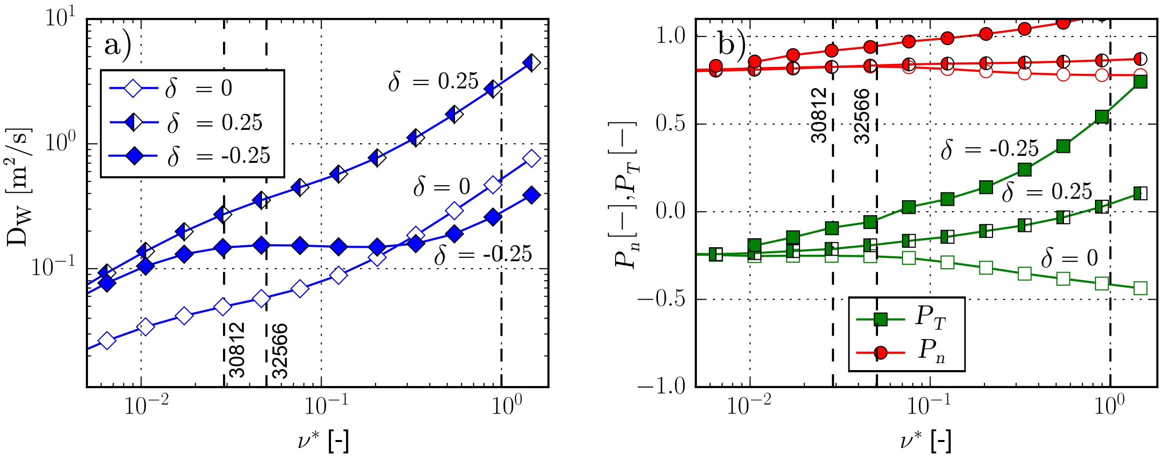

Figure 8.6.: The collisionality scan of the neoclassical transport coefficients calculated in presence of the poloidal asymmetries. a) The tungsten diffusion coefficient D_W evaluated without asymmetry (open markers), with positive asymmetry (half open markers), and negative asymmetry (full markers). b) Ion density (red) and temperature (green) peaking coefficient evaluated for various values of the asymmetry using identical marking as in a).

8.3.3. Comparison with the Experiment

The NEO code was applied to model the transport coefficients in the previously investigated discharge #32324. For the modeling we used time averaged kinetic profiles and the asymmetry was varied in the range $\delta = -0.15$ to 0.4. The missing core measurements of n_e causes a substantial uncertainty in the core n_i gradient, resulting in a possible underestimation of the neoclassical pinch. Since we would like to analyze at least the trend of v/D versus the poloidal asymmetry, the core value of $\nabla \ln n_i$ obtained from IDA was increased by 50 % to match our v/D measurements.

As shown in Fig. 8.7a, the neoclassical value of D_W increases from $D_W = 0.04$ for zero asymmetry to $D_W = 0.8$ at $\delta = 0.25$. At low asymmetry, the measured D_W match well D_{neo}. However, during the Q3 phase with high asymmetry, the value of D_{neo} overestimates the measurements by factor 2–4. In other words, the timescale of the transport process should be 2–4 times faster. It could indicate limitations of our measurement method as was discussed in Sec. 8.2. The negative asymmetry region was not covered by this experiment, and further investigation should focus on the combination of ICRF and NBI to verify the neoclassical prediction also for $\delta < -\varepsilon$. The neoclassical drift coefficient v/D depicted in Fig. 8.7b, depends only weakly on the asymmetry, mainly due to the variation of the T_i screening (cf. 8.5b). This trend is confirmed by experimental values, which stay unchanged within the uncertainty. In conclusion, within the limitation of our method and the experimental uncertainty, the extended neoclassical theory has been validated.

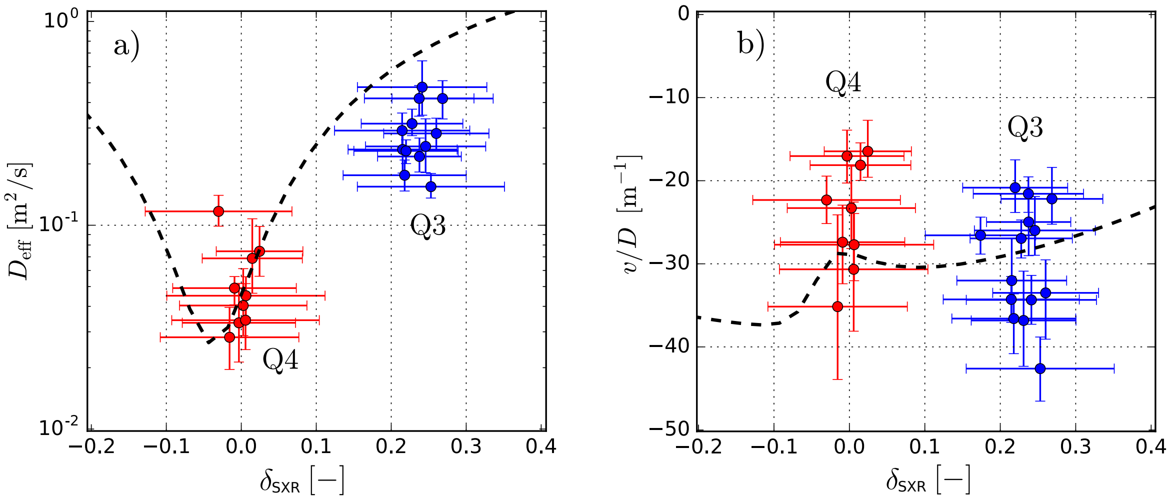

Figure 8.7.: The neoclassical value of the transport coefficient (dashed lines) for the discharge #32324 at $\rho_{\mathrm{tor}} = 0.12$ compared with the experimentally measured values (dots) in the Q3 phase (blue) and the Q4 phase (red) for the effective diffusion coefficient D_{eff} Eq. (8.3) a) and the drift coefficient v/D b).

8.4. Conclusions

This chapter was dedicated to the validation of the neoclassical theory extended for the poloidal variation of the impurities density. The investigated discharge #32324 was chosen for it's two almost identical phases different only in the W asymmetry level, induced by a change in the NBI source. A low variation between these two phases is critical to minimize an influence of the other transport mechanisms unrelated to the poloidal asymmetry. Our investigation was focused on the most central region of plasma dominated by neoclassical transport, where the largest effects were expected. Proper measurements of the core tungsten density and its asymmetry were achieved using high-resolution SXR tomography of the W emissivity. In order to disentangle the diffusive and the convective contribution to the impurity transport, perturbations in the core impurity flux caused by the sawtooth crashes were analyzed. The investigation was performed utilizing two independent techniques, i.e. the gradient flux method and the least squares method, to minimize the error introduced by our methodology. The measurements resolved the reduction of the diffusion coefficient D_W by a factor of five when the asymmetry was reduced from $\delta = 0.25$ to zero. At the same time, no significant change in the drift coefficient v/D was observed.

The neoclassical modeling of tungsten transport was performed using the NEO code. The influence of the poloidal asymmetry on the impurity density was illustrated by a scan over the Mach number. The minimum in the impurity flux occurs at $\delta_{\mathrm{min}}/\varepsilon = -1$, which is a factor of 2 weaker asymmetry then expected from the analytical theory. Additionally, a significant reduction of the T_i screening was found for $\delta/\varepsilon < -1$. The collisionality scan indicated a huge impact of the poloidal asymmetries on the T_i screening in the Pfirsch-Schlüter regime, while in the very low collisionality regime the screening was almost unaffected.

Finally, a comparison of the simulated D_W with the experimental values matches well with the low asymmetry case, while the measured D_W in the high asymmetry case is underestimated by factor of 2–4. However, this might merely be a consequence of the limitations of the applied experimental technique.

These findings are expected to have a direct impact on optimization of AUG plasma scenarios. A proper combination of the perpendicular beams and the position of ICRF heating can keep the asymmetry between $-1 < \delta/\varepsilon < 0$. In such a case, we can expect the reduction of the neoclassical flux by an order of magnitude, while the T_i screening is still significant. Also, a simple replacement of the parallel beams by more perpendicular ones should stabilize NBI-only discharges, which are prone to W accumulation. Finally, the proper choice of NBI beams can be an efficient method for avoiding tungsten accumulation in real-time, since less additional core electron heating will be required to suppress the neoclassical impurity influx.

9. Summary and Outlook

Impurities are inevitably present in tokamak plasmas due to plasma wall interaction. A thorough understanding of impurity transport is crucial for the success of fusion reactors because the radiation losses caused by them significantly degrade the fusion gain. Moreover, accumulation of impurities has a detrimental effect on the discharges and can lead to a plasma disruption. The impact of poloidal asymmetries in the impurity density on the radial transport was neglected in the experiments until recently and therefore, this thesis focuses on their detailed investigation. To that end, an experimental validation of the existing theoretical models is presented.

The core impurity density depends on a whole chain of processes. First, the impurities are sputtered from plasma facing components, then transported across the plasma edge, and the bulk plasma to the plasma center. Each of these regions is characterized by different transport mechanisms, i.e. neoclassical and turbulent transport or transport induced by MHD instabilities. To predict the high-Z impurity profiles in future devices, an understanding of all these steps is needed. The effect of the parallel force balance on the poloidal density profile of high-Z impurities represents a small but critical piece needed to understand the impurity transport, which was neglected until recently [114–116]. The most common cause of poloidal asymmetries in the plasma core is the centrifugal force driven by the fast plasma rotation and the perturbation of the electrostatic potential due to non-thermal particles. In this thesis, we present both, new theoretical models adressing the parallel and radial impurity transport in the plasma and experiments for their benchmarking.

In order to investigate the poloidal asymmetries in the impurity density, a tomographic reconstruction code optimized for the soft X-ray (SXR) diagnostics was developed (Chapter 4 and Appendix A). A reliable measurement of the SXR radiation profiles of tungsten featuring steep gradients requires unprecedented accuracy of the reconstruction and the highest possible spatial resolution. Therefore, the new tomographic code utilizes a detailed model of the SXR geometry including the real width of the lines of sight and a virtual curvature due to the toroidal shape of the plasma. The optimal corrections of the SXR geometry and the cross-calibration factors between the cameras were found self-consistently, which helped to reduce the reconstruction residua by an order of magnitude and suppress tomographic artifacts. The newly developed inversion techniques reduced the complexity of the inversion from cubic to linear and greatly reduced the computing time to less than a minute per discharge at $\tilde{1}$ cm spatial resolution in excellent quality. And finally, a detailed analysis of the reconstruction bias and statistical errors was performed in Sec. 4.2 to estimate the uncertainty in the emissivity profiles. The possibilities of this tomography code are multifaceted, including the reconstruction of the emissivity profiles from SXR and bolometers diagnostics, observations of the poloidal asymmetry in the SXR radiation, or an analysis of the MHD activity.

Utilizing the developed tomography, the poloidal impurity asymmetries due to the centrifugal force have been investigated. The detailed study of the poloidal radiation profiles shown in Sec. 6.1 has demonstrated an excellent match of the reconstructed profiles with those predicted by a theoretical model in the plasma core. Discrepancies observed at the plasma edge may be explained by SXR radiation from light impurities.

Further investigations of poloidal asymmetries focused on effects of non-thermal ions. For this purpose, a set of low-density neutral beam injection (NBI) heated discharges was investigated. In these discharges, a tangential beam was replaced by a radially injected beam, reducing the calculated centrifugal asymmetry by 50 %, while the observed asymmetry was reduced to about zero. Three independent models for the description of the spatial distribution of the fast particles were developed to explain the behavior of the poloidaly asymmetric tungsten density. The best match with the experimental data was achieved with the Monte Carlo model in TRANSP, which is the only one including ∇B-drift effects acting on the particles orbits. The orbit effects are critical for the NBI geometry on ASDEX Upgrade. For instance, the increase of the inboard side density due to the passing ions from the most frequently used beam Q3 is almost entirely canceled by this orbit effects. The measurements presented in this thesis are the first observations of the NBI ions affecting the poloidal asymmetry of impurities and therefore, a further exploration on tokamaks with a wider flexibility in the beam configuration would be beneficial.

Another heating method producing a significant population of fast ions is ion cyclotron range of frequencies (ICRF) heating, which increases the perpendicular momentum of the hydrogen ions causing a large temperature anisotropy and trapping due to the magnetic mirror effect. The trapped ions produce perturbations in the poloidal electric potential, affecting the parallel transport of highly charged impurities such as tungsten. The poloidal tungsten density profile was modeled by a combination of the parallel force balance and Dendy's model to describe the fast hydrogen ions, providing a more accurate poloidal profile than in a previous experimental study [121]. The asymmetry model is first verified on a low-density discharge with an outboard ICRF resonance. A match of the radial asymmetry profile and also a detailed poloidal dependence of the SXR emissivity with the experiment was found for both tested ICRF codes, i.e. TORIC-FFPMOD and TORIC-SSFPQL. However, the modeling of an inboard side heated discharge revealed differences between the FPPMOD and the SSFPQL model.

The temperature anisotropy calculated by TORIC-SSFPQL exceeded the upper limit given by Dendy's model, and the modeled poloidal tungsten asymmetry was therefore overestimated. TORIC-FPPMOD predicted a much smaller asymmetry, in agreement with our experimental measurement.

Further, a database consisting of all suitable discharges with the ICRF asymmetry was build in order to probe the properties of the fast hydrogen ions. The investigation revealed a significant scaling of the asymmetry with one over density squared and a weak electron temperature dependence. This observation is in agreement with the basic theoretical model since the pitch angle scattering operator in the Fokker-Planck equation shows such a scaling as well. However, a comparison of this empirical scaling with parameter scans performed using TORIC-FFPMOD indicated a substantial discrepancy in the dependence of the asymmetry on the electron density $n_e \gtrsim 4 \cdot 10^{19}\,\mathrm{m}^{-3}$, i.e. the densities of the typical AUG discharges. Finally, the pioneering study of the fast ion transport was performed in Sec. 7.4. A clear effect of the sawtooth crashes (i.e. a MHD plasma instability) on the asymmetry caused by a flattening of the fast particle distribution profiles was observed. In summary, the measurements of the poloidal asymmetries served for the first time as a diagnostic tool to investigate fast particles. Also, these measurements provide a valuable benchmark for certain aspects of the ICRF modeling codes.

The last chapter is dedicated to radial impurity transport including the effect of the poloidal asymmetries. The neoclassical transport theory extended for the poloidal asymmetries predicts an immense impact of the poloidal asymmetry on the radial impurity flux. However, despite the importance of this influence, an unambiguous experimental verification was not accomplished up to now. The main challenge is the disentanglement of the poloidal asymmetry and the transport changes due to the variation in the heating sources used to modify this asymmetry. Moreover, the modification of the asymmetry must be large enough to be detected, given the substantial uncertainty of the measured transport coefficients. To resolve this issue, we have investigated in Sec. 8.1.1 a discharge, where switching between two NBI beams caused a substantial variation in the poloidal asymmetry, while the rest of the discharge parameters stayed almost constant. The core transport coefficients, D for diffusion and v for convection, were disentangled by the investigation of the phase between large sawtooth crashes, which yielded regular perturbations of the radial W-density profile. The transport was studied very close to the plasma core, where the turbulent contribution to the flux was expected to be negligible. By switching from a more tangential beam to a more radial one, the poloidal asymmetry was removed, and the tungsten diffusion coefficients decreased by a factor of 5, while the drift coefficient v/D stayed roughly unchanged. Both observations are in agreement with neoclassical theory modelled by the NEO code.

In order to further investigate this plasma behavior, scans of the asymmetry and the collisionality were performed by NEO. In these scans, the diffusion coefficient and thus also the magnitude of the neoclassical flux reached a minimum for a poloidal asymmetry $\delta/\varepsilon = -1$ (where ε is the local inverse aspect ratio), i.e. slighly more impurities at the inboard side. In the close vicinity of the minimum, D increases linearly with δ. The effect of T_i screening, which leads to a possible outward convection, is reduced by a factor of 2 for in-out asymmetries $\delta/\varepsilon < 1$ due to a changed sign of the trapped ion contribution to the impurity convection.

It is expected that our findings will have a direct impact on the strategies for the avoidance of tungsten accumulation because as is demonstrated within the present work, a mere switching of two almost equivalent neutral beams can reduce the unfavorable neoclassical transport by nearly an order of magnitude. In such a case, less additional core electron heating power would be required to prevent the tungsten accumulation.

Outlook

Although our work represents a quite comprehensive investigation of the high-Z parallel and perpendicular impurity transport, there are topics which remain to be revisited. Firstly, the observed change of the poloidal asymmetry driven by fast NBI ions exceeded the predicted values by a factor of two. The possibility of a systematical error in the measurement could not be rejected, but the examination of a future discharge with a flatter SXR radiation profile could resolve the doubts. A further investigation of the fast NBI ions is limited by the geometry of the NBI available at AUG, and therefore, additional experiments on other machines would be beneficial.

The ICRF driven asymmetries open up new possibilities to benchmark the codes modeling ICRF heating. The mismatch between the experiment and the model should motivate a further development of these codes. For instance, the code SELFO [149] includes the finite orbit width effects and the self-consistent response of the heated ion profile on its temperature anisotropy could improve the agreement with the experiment. The poloidal asymmetries in high-Z impurities density present a rare opportunity to verify the importance of such effects experimentally. Along the same lines, the observed discrepancy in the scaling of the asymmetry with the electron density requires further investigation. A database study of data from Alcator C-Mod could shed light on this problem, because of their excellent toroidal bolometers [150], the intrinsic molybdenum content, the large ICRF power and the lack of neutral beams and ELMs makes this tokamak ideal for such studies [71].

In order to strengthen the findings on radial impurity transport, further investigations are advised. A combination of the radial/tangential NBI and outboard ICRF heating could help to extend the measurements also for the HFS asymmetries if a way how to maintain a low electron density is found. Alternatively, further investigations on tokamaks with a larger variation in the NBI geometry could extend the range of the accessible poloidal asymmetries as well.

Finally, the problem requiring further investigation beyond the scope of this thesis is the impurity transport driven by MHD modes. A hollow W density profile is found in almost every AUG discharge with core ECRH heating, and a connection between the hollowness and the presence of the saturated 1/1 mode has been shown [151, 152]. However, we have discovered a small up-down asymmetry (5–10 %) in the time averaged core SXR radiation of these discharges, which are a consequence of a significant asymmetry inside of the displaced plasma core as shown in Fig. 9.1. Such a density variation can drive a significant outward drift as was pointed out in Sec. 5.3.3. Even if the up-down asymmetries are relatively common, they have not been diagnosed until now due to their small magnitude that is often cloaked by the large centrifugal asymmetry. Due to the 3D nature of the MHD modes and the complex behavior, the explanation of the asymmetry has not been found yet, and it is a subject of ongoing research. The investigation of transport in 3D structures such as MHD modes can benefit from high-Z impurity studies in stellarators, where the up-down asymmetries were also observed [80] and the theoretical examination using the EUTERPE code has already started [78].

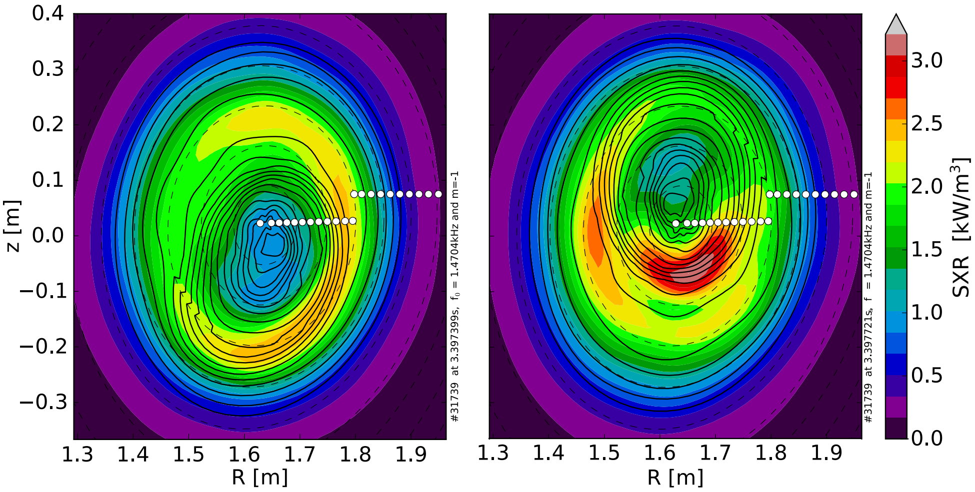

Figure 9.1.: Tomographic reconstruction of the SXR radiation from discharge #31739 at 3.397 s for the 1/1 mode on the top (left) and bottom (right) compared with the black contours of the electron temperature obtained by mapping of the LFS profile using the rigid body assumption [153]. When the mode is on the top, SXR contours follow the T_e contours, however, when the mode is at the bottom, a huge up-down asymmetry arises.

Appendix

A. Optimized tomography inversion algorithms

Essential part of our tomographic algorithm in Chapter 4 are new methods for the fast solution of the inversion problem and methods for the selection of the proper regularization level. All methods used up to now for the solution of Eq. 4.7 suffers by a high computation cost, because the inversion time scales as $\mathcal{O}(n^3)$, where n is number of pixels $\sim 10^4$. The inversion methods introduced in this chapter enables much faster inversions of $\mathcal{O}(nm^2 + m^3)$, where m is number of detectors $\sim 10^2$. Additionally, this inversion methods can be used together with sophisticated methods for the selection of the optimization level with a mere $\mathcal{O}(m^2)$ complexity, and much higher quality as will be shown at the end of this chapter.

A.1. Sparse Diagonalization Methods

A large variety of methods were developed to solve the Tikhonov problem, for instance the generalized eigenvalues (GEV) [154, 155] method, the singular value decomposition (SVD) method [156], the generalized SVD (GSVD) [45, 157] method, bidiagonalization [158], and the most common is the direct inversion [46, 47, 57, 159]. However, in the current implementation, none of these methods are able to efficiently take advantage of all of the aspects specific to the Tikhonov regularized SXR tomography. First of all, the projection matrix $\mathbf{T}$ has a small numerical rank $r \leq m \ll n$, with typical values of $r = m \sim 10^2$ and $n \sim 10^4$. The regularization operator $\mathbf{H}$ is a full rank positive definite matrix. Further, both matrices are sparse; the $\mathbf{T}$ matrix for the AUG SXR system has roughly only 5 % non-zero elements and the matrix $\mathbf{H}$ has a regular sparsity pattern and approximately 0.01 % fill-in.

In this section, we present modifications of the SVD and QR algorithms for the solution of the Tikhonov regularization that allows for taking full advantage of these conditions.

A.1.1. Generalized Eigenvalues (GEV) Decomposition

The first algorithm is based on the generalized eigenvalue decomposition (GEV) of the matrix $\mathbf{T}^T\mathbf{T}$ and the regularization matrix $\mathbf{H}$. The solution of the GEV is a matrix $\mathbf{X} \in \mathbb{R}^{n,m}$ with eigen-vectors fulfilling the conditions

$$(\mathbf{T}^T\mathbf{T})\mathbf{X} = \mathbf{\Lambda}\mathbf{H}\mathbf{X} \qquad \mathbf{X}^T\mathbf{H}\mathbf{X} = \mathbf{I} \tag{A.1}$$

where $\mathbf{\Lambda} \in \mathbb{R}^{m,m}$ is a diagonal matrix with positive eigenvalues on the diagonal sorted in descending order. Additionally, the generalized eigenvectors are orthonormal in the scalar product generated by the positive definite matrix $\mathbf{H}$. Consequence of the relations in Eq. (A.1) is following identity for matrix $\mathbf{T}^T\mathbf{T}$

$$\mathbf{X}^T(\mathbf{T}^T\mathbf{T})\mathbf{T} = \mathbf{\Lambda} \tag{A.2}$$

The Tikhonov regularization is transformed into a more convenient form using Eqs. (A.1) and (A.2)

$$\left(\mathbf{T}^T\mathbf{T} + \lambda\mathbf{H}\right)^{-1}\mathbf{T}^T = \mathbf{X}(\mathbf{\Lambda} + \lambda\mathbf{I})^{-1}\mathbf{X}^T\mathbf{T}^T. \tag{A.3}$$

The decomposition in this form can be already solved efficiently because solution $\mathbf{g}(\lambda)$ can be found in $\mathcal{O}(n)$ operations. The computationally most expensive step is now GEV itself. Full GEV can be computed with $\mathcal{O}(n^3)$ operations in the case of dense matrices $\mathbf{T}$ and $\mathbf{H}$. However, numerical tests of the GEV routine for sparse Hermite matrices from the ARPACK library [160] show quadratic dependence on the number of pixels n as it will be demonstrated in Section A.1.4.

If the regularization matrix $\mathbf{H}$ is defined in the form of a product $\mathbf{L}^T\mathbf{L}$, a suitable decomposition of the Eq. (4.7) can be found by the generalized singular value decomposition technique (GSVD) [161] as well. This method is based on simultaneous decomposition of the matrices $\mathbf{T}$ and $\mathbf{L}$. The GSVD computes two orthonormal matrices $\mathbf{U} \in \mathbb{R}^{m,m}$, $\mathbf{V} \in \mathbb{R}^{n,n}$, a positive diagonal matrix $\mathbf{C} \in \mathbb{R}^{m,m}$, $\mathbf{S} \in \mathbb{R}^{m,m}$ and a full rank matrix $\tilde{\mathbf{X}} \in \mathbb{R}^{n,m}$ with following properties

$$\mathbf{U}^T\mathbf{T}\tilde{\mathbf{X}} = \mathbf{S} \qquad \mathbf{V}^T\mathbf{L}\tilde{\mathbf{X}} = \mathbf{C} \qquad \mathbf{C}^2 + \mathbf{S}^2 = \mathbf{I} \tag{A.4}$$

The following identity can be obtained from the Eq. (4.7),

$$\left(\mathbf{T}^T\mathbf{T} + \lambda\mathbf{L}^T\mathbf{L}\right)^{-1}\mathbf{T}^T = \tilde{\mathbf{X}}(\mathbf{S}^2 + \lambda\mathbf{C}^2)^{-1}\tilde{\mathbf{X}}^T\mathbf{T}^T. \tag{A.5}$$

The relation to the GEV decomposition can be easily verified, since $\mathbf{X} = \tilde{\mathbf{X}}\mathbf{S}^{-1}$ and $\mathbf{\Lambda} = \mathbf{C}\mathbf{S}^{-1}$.

A.1.2. Sparse SVD Decomposition (sSVD)

Singular value decomposition is a common tool for the solution of the Tikhonov regularization in the standard form, i.e. when the regularization operator is an identity matrix $\mathbf{I}_n$ [162]. Hence, it is necessary to transform Eq. (4.6) into the standard form, before the SVD method can be applied. In the case of $\mathbf{H} = \mathbf{L}^T\mathbf{L}$ and if $\mathbf{L}$ is an invertible operator, the transformation is straightforward:

$$\bar{\mathbf{T}} = \mathbf{T}\mathbf{L}^{-1} \qquad \bar{\mathbf{g}} = \mathbf{L}\mathbf{g}$$

and then substitution into Eq. (4.6) we get

$$\|\mathbf{T}\mathbf{g} - \mathbf{b}\|_2^2 + \lambda\|\mathbf{L}\mathbf{g}\|_2^2 = \|\bar{\mathbf{T}}\bar{\mathbf{g}} - \mathbf{b}\|_2^2 + \lambda\|\bar{\mathbf{g}}\|_2^2,$$

where $\|\cdot\|_2^2$ denotes the Euclidean norm. This transformation method was proposed by Tarasaki [156] for the discretized Laplace operator. Let's consider a more general case of a sparse and positive definite, but otherwise arbitrary, matrix $\mathbf{H}$. The transformation to the standard form can be performed very effectively by the sparse Cholesky decomposition [163] of $\mathbf{H}$. A regularized solution is found via the following steps:

1. The sparse Cholesky decomposition of the matrix $\mathbf{H}$ is evaluated through

$$\mathbf{P}\mathbf{H}\mathbf{P}^T = \mathbf{L}\mathbf{L}^T, \tag{A.6}$$

where $\mathbf{L}$ is a sparse lower triangular matrix and $\mathbf{P}$ is a fill-reducing permutation.

2. In the next step, Eq. (4.7) is transformed into the standard form

$$\left(\mathbf{T}^T\mathbf{T} + \lambda\mathbf{P}^T\mathbf{L}\mathbf{L}^T\mathbf{P}\right)^{-1}\mathbf{T}^T = \mathbf{P}^T\mathbf{L}^{-T}\left(\mathbf{A}^T\mathbf{A} + \lambda\mathbf{I}_n\right)\mathbf{A}^T \tag{A.7}$$

defining the integrated projection matrix $\mathbf{L}^{-1}\mathbf{P}\mathbf{T}^T$ as $\mathbf{A}$. Exploiting the sparsity of the $\mathbf{H}$ and $\mathbf{T}$ matrices, such an inversion can be evaluated with $\mathcal{O}(nm)$ complexity. The matrix $\mathbf{A}$ is not sparse anymore, except for the empty rows corresponding to the pixels outside of the plasma boundary. For this reason, the SVD in the following step will be evaluated for non-zero rows only.

3. After the standard form is obtained, the solution can be found by the SVD decomposition of the matrix $\mathbf{A}$, i.e. $\mathbf{A} = \mathbf{U}\mathbf{D}\mathbf{V}^T$. The columns of the matrices $\mathbf{U} \in \mathbb{R}^{m,r}$ and $\mathbf{V} \in \mathbb{R}^{n,r}$ are left-singular and right-singular vectors of $\mathbf{A}$, and $\mathbf{D} \in \mathbb{R}^{r,r}$ is a matrix with singular values on the diagonal in descending order. Substituting the obtained SVD of $\mathbf{A}$ into Eq. (A.7) results in a decomposition of

a form that is already appropriate for the numerical solution

$$\mathbf{P}^T\mathbf{L}^{-T}\Big(\mathbf{A}^T\mathbf{A}+\lambda\mathbf{I}_n\Big)\mathbf{A}^T=\tilde{\mathbf{V}}(\mathbf{D}^2+\lambda\mathbf{I}_r)^{-1}\mathbf{D}\mathbf{U}^T$$

where matrix $\tilde{\mathbf{V}}\in\mathbb{R}^{n,r}$ of the reconstruction basis is defined as $\tilde{\mathbf{V}}\equiv\mathbf{P}^T\mathbf{L}^{-T}\mathbf{V}$. Nevertheless, since the matrix $\mathbf{A}$ is "tall-and-slim", it is usually more economical to calculate an eigen-decomposition of the smaller Hermitian matrix $\mathbf{A}\mathbf{A}^T=\mathbf{X}\mathbf{\Lambda}\mathbf{X}^T$ instead of a proper SVD. In such a case $\mathbf{D}=\mathbf{\Lambda}^{1/2}$, $\mathbf{U}$ corresponds to the eigenvectors $\mathbf{X}$ and $\mathbf{V}=\mathbf{A}^T\mathbf{U}\mathbf{D}^{-1}$. Since the matrix $\mathbf{A}\mathbf{A}^T$ has a squared condition number compared to $\mathbf{A}$, one could expect a reduced numerical accuracy. But the regularization is suppressing the least significant eigenvalues and no impact on the reconstruction accuracy was observed.

4. The regularized solution $\mathbf{g}_\lambda$ is obtained in the form of a series expansion

$$\mathbf{g}_\lambda=\sum_{i=1}^{r}f_{i,\lambda}\frac{(\mathbf{U}_i^T\mathbf{b})}{D_i}\tilde{\mathbf{V}}_i. \tag{A.8}$$

Here $\mathbf{U}_i$ and $\tilde{\mathbf{V}}_i$ denote columns of matrices $\mathbf{U}$ and $\tilde{\mathbf{V}}$, respectively. The filtering factors are defined as $f_{i,\lambda}=(1+\lambda/D_i^2)^{-1}$, monotonously decreasing with λ and i.

The first step, when the Cholesky decomposition of the $\mathbf{H}$ matrix is performed, has linear complexity because of the regular sparsity pattern and the small number of non-zero elements proportional to n. The time spent in this step is negligible. The second step is done by back-substitution of the sparse lower triangular matrix $\mathbf{L}$ with $\mathcal{O}(nm)$ complexity. When SVD is replaced by the eigenvector decomposition (EV), then the required number of operations scales as $\mathcal{O}(m^3+nm^2)$, while if the thin SVD is applied, the number of flops will increase to $2nm^2+11\,m^3$ as was shown in Ref. [164], and the measured computing time was increased by a factor of five. The other steps also do not affect the final linear complexity. Moreover, our analysis indicates a cubic dependence of the decomposition time on the number of detectors m in the EV.

A.1.3. Sparse QR Decomposition (sQR)

An alternative method based on a triple application of the QR decomposition was proposed in Ref. [165] by Hosoda. This method does not provide a perfect solution of Eq. (4.7), however, the solution is a very close approximation, the difference is usually lower than 0.1 %. Previous comparisons of the original algorithms [156] have shown ten times lower computation cost than the former SVD method.

The description of the optimized algorithm for the decomposition of the sparse matrices is summarized below:

1. The first step is identical to the sSVD method; the matrix $\mathbf{A}$ is obtained via the integration of the projection matrix.

2. In the next step, the pivoted rank-revealing QR decomposition is applied on $\mathbf{A}$
$$\mathbf{Q}_1\hat{\mathbf{D}}\mathbf{S} \overset{RRQR}{=} \mathbf{A}\mathbf{\Pi}, \tag{A.9}$$
where $\mathbf{Q}_1 \in \mathbb{R}^{n,r}$ is a unitary matrix, $\hat{\mathbf{D}} \in \mathbb{R}^{r,r}$ is a diagonal matrix with positive diagonal values sorted in non-increasing order, $\mathbf{S}$ is an upper triangular matrix with a unitary diagonal and $\mathbf{\Pi}$ is a permutation matrix. The Q-less QR decomposition can be employed, because $\mathbf{Q}_1$ is not required explicitly in the following steps.

3. The ordinary QR decomposition is applied to the matrix $\mathbf{\Pi}\mathbf{S}^T$
$$\mathbf{Q}_2\mathbf{R}_2 \overset{QR}{=} \mathbf{\Pi}\mathbf{S}^T$$
where $\mathbf{R}_2 \in \mathbb{R}^{r,r}$ is an upper triangular matrix and $\mathbf{Q}_2 \in \mathbb{R}^{m,r}$ is a unitary matrix.

4. Now the diagonal matrix $\mathbf{D}$ is swapped with the $\mathbf{R_2}$ matrix
$$\mathbf{M} = \hat{\mathbf{D}}R_2^T\hat{\mathbf{D}}^{-1}$$
and the third QR decomposition of the matrix M is computed
$$\mathbf{R}_3\mathbf{D}_R\mathbf{Q}_3 \overset{QR}{=} \mathbf{M}$$
Just like in the second step, the Q-less QR decomposition can be used. $\mathbf{R}_3 \in \mathbb{R}^{r,r}$ is an upper triangular matrix with a unitary diagonal and $\mathbf{D}_R \in \mathbb{R}^{r,r}$ is a diagonal matrix.

5. In the last step, the final integration by the $\mathbf{L}$ operator is performed and the decomposition is transformed to the form analogous to the preceding method
$$\begin{aligned}
&\mathbf{R} = \hat{\mathbf{D}}\mathbf{R}_3^T(\mathbf{D}\mathbf{D}_R)^{-1}\\
&\mathbf{D} = \hat{\mathbf{D}}\mathbf{D}_R\\
&\mathbf{U} = \left(\mathbf{R}_3^{-1}\mathbf{Q}_2^T\right)^T \quad \text{(Forward-substitution)}\\
&\mathbf{V} = \mathbf{A}\mathbf{U}\mathbf{D}^{-1}\\
&\hat{\mathbf{V}} = (\mathbf{P}\mathbf{L}^{-T}\mathbf{V})^T \quad \text{(Back-substitution).}
\end{aligned}$$

Since the definitions of the matrices $\mathbf{U}$, $\mathbf{D}$ and $\hat{\mathbf{V}}$ are now consistent with the notation in the sSVD algorithms, the regularized solution can be estimated by formula (A.8). The arguments used for the analysis of the computational complexity of the sSVD method are valid here as well. In the sQR algorithm the most expensive step is the first RRQR decomposition requiring $\mathcal{O}(nm^2 + m^3)$ operations [164]. The other steps have a $\mathcal{O}(nm)$ complexity or even lower. Since the asymptotic complexities of both algorithms are identical, it is necessary to assess these algorithms by a direct comparison of the computation time.

A.1.4. Computational Effort

In addition to the algorithms introduced in the previous section, also the GEV method [154] based on the GEV routine for sparse Hermitian matrices from the ARPACK library [160] and GSVD [157] were included in the investigation in this section, because both are regularly used for the solution of the generalized Tikhonov problem. The comparison was performed for a variable number of pixels n and with a fixed number of $m = k = 200$ detectors. The number of the non-zero elements in the projection matrix was about 5 % and the anisotropic regularization operator used had all non-zero elements regularly aligned in nine diagonals. All computation tests were run in a single thread on an Intel Core i5-2540M processor to allow a fair comparison of these methods. An algorithm based on the direct inversion of the Tikhonov problem by the sparse Cholesky solver [47] was used as reference method. The measured computation times are shown in Fig. A.1 with dashed lines indicating the asymptotic complexity.

The fastest method is based on the sQR decomposition and it takes about 34 ms for a moderate resolution 40×60 pixels. sQR is followed by the sSVD algorithm, which is 30 % slower. Both algorithms show a linear time complexity in the number of pixels n, which tails off for $n \lesssim 5m$. Other algorithms based on the GEV and the GSVD are, for a reasonable range of n, significantly slower than the direct inversion. The time measured for the algorithm based on the sparse GEV are have a quadratic complexity in n, but with a rather large multiplication factor. Finally, GSVD based on sine-cosine decomposition [161] is not able to efficiently take advantage of the matrix sparsity and, thus the computing time scales as $\mathcal{O}(n^3)$. The decomposition methods even further outperform the direct solvers because at least $3 - 10$ inversions are necessary to solve the inner loop of the MFI algorithm and find the optimal regularization parameter. But, once the decomposition is available, the inner loop can be solved almost instantaneously in ≈ 1 ms with $\mathcal{O}(mk)$ complexity. The numerical accuracy of all algorithms solving Eq. (4.7) was better than 10^{-12}, except for sQR, which provides inversion with a difference of 10^{-3}. This is still well below the experimental uncertainties.

The sSVD and sQR decomposition methods are very efficient especially in the case

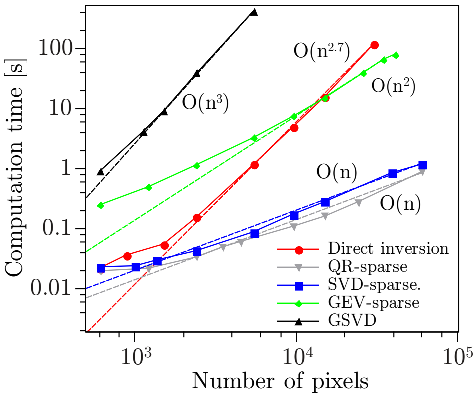

Figure A.1.: Computation times of different decomposition methods were compared to the direct inversion algorithm based on the sparse Cholesky decomposition [47]. The asymptotic complexity is indicated by the dashed lines.

of a low-rank projection matrix. The direct inversion is faster only if the rank r is comparable with n or at very low resolution $n \ll 10^3$ as was shown in Refs. [166, 167]. Since the large scale changes in the emissivity profile usually evolve on much slower timescales than the sampling frequency, it is not necessary to evaluate a decomposition for each time frame separately, but instead the discharge can be divided into short blocks reconstructed at once. In such cases, it is possible to compute roughly 200 frames/s at a moderate resolution of 40×60 px.

A.2. The Optimal Choice of the Regularization Parameter

One of the key issues related to the Tikhonov regularization is the proper selection of the regularization parameter. The optimal parameter λ_{opt} minimizes the difference between the reconstructed and the original profile. Since the original radiation distribution is not available in the experiment, this parameter must be determined purely from the measurements and a priori knowledge. Moreover, the optimal estimator of λ_{opt} should be robust, reliable, and the computation complexity should be polynomial in m, independent of the number of pixels n. Hence, the optimal solution must be found without the explicit evaluation of $\mathbf{g}_\lambda$.

Many different methods have been proposed for the choice of the regularization level. Commonly used methods include the Morozov's discrepancy principle (DP) [23, 168], the curvature of the L-curve
[169], the generalized cross-validation (GCV) [44, 156], the predicted sum of squares

(PRESS) [170], the corrected Akaike information criterion ($\mathrm{AIC_C}$) [171] and the quasi-optimality criterion [172, 173]. However, with the exception of DP, these methods are not regularly used in SXR plasma tomography. Since the behavior of these methods significantly depends on the investigated problem, the only way to identify the most suitable one is to perform a comparison on artificial and experimental measurements. Tests of these methods on the artificial radiation profiles allowed for identification of the most promising methods, namely PRESS, $\mathrm{AIC_C}$, GCV, and DP. Due to the highly ill-posed character of SXR tomography, the corner of the L-curve is insignificant or missing on real measurements. The quasi-optimality criterion is not able to provide a single, reliable and unique optimum even for simple artificial profiles. Finally, the compatibility of the remaining methods with the nonlinear MFI needs to be investigated.

The *regularization level* in the following section will be quantified by the quantile q_λ in the set $\{D_i^2\}$ equal to λ. Compared to the regularization coefficient λ itself, whose value does not have a direct meaning and depends on the normalization of the $\mathbf{H}$ and $\mathbf{T}$ matrices, q_λ roughly corresponds to the fraction of degrees of freedom removed by the regularization. A value close to one results in very high regularization, almost completely ignoring the measurements, while a value of about zero causes negligible regularization.

A.2.1. Discrepancy Principle

For the choice of the optimal regularization parameter, the Morozov's discrepancy principle (DP) is the most common method used by plasma physicists [47, 48, 57, 166, 168]. The regularization parameter is chosen such that the residual norm for the solution $\mathbf{g}_\lambda$ satisfies

$$\|\mathbf{T}\mathbf{g}_\lambda - \mathbf{b}\|_2^2 - \|\boldsymbol{\epsilon}\|_2^2 = 0, \tag{A.10}$$

where $\boldsymbol{\epsilon}$ is the estimated noise level. This condition together with the minimization of the regularization functional leads to a constrained quadratic optimization problem, easily solvable by an iterative root-solver. A unique solution satisfying the condition (A.10) exists if $\|\mathbf{b} - \mathbf{U}\mathbf{U}^T\mathbf{b}\|_2 < \|\boldsymbol{\epsilon}\|_2^2$ and $\|\mathbf{b}\|_2^2 > \|\boldsymbol{\epsilon}\|_2^2$, which is always fulfilled if the projection matrix $\mathbf{T}$ has full rank and the measurements exceed the noise level. For the decomposition methods introduced earlier, the residuum can be expressed in the following form

$$\|\mathbf{T}\mathbf{g}_\lambda - \mathbf{b}\|_2^2 = \sum_{i=1}^{m} \Big((1 - f_{i,\lambda})\mathbf{U}_i^T\mathbf{b}\Big)^2, \tag{A.11}$$

where $f_{i,\lambda}$ are the filtering factors introduced in Eq. (A.8), $f_{i,\lambda} = 0$ for $i \geq r$ and $\mathbf{U}$ must be multiplied by the matrix $\mathbf{R}$ from the right for the sQR method. The root in λ can be found with a mere $\mathcal{O}(mk)$ complexity. The choice of Eq. (A.10) was motivated by the fact that if the Tikhonov regularization is correctly weighted by the statistical uncertainties, while an approximately normal noise distribution is assumed, then the residuum will have a χ^2 distribution with p degrees of freedom. The expected value of χ^2 is also p and it can easily be checked that $p = m - k + \sum_{i=1}^{k}(1 - f_i)^2$. Since the existence of the root is not generally guaranteed, we assume $p \equiv m$, which leads to Eq. (A.10) and tends to a slight overestimation of the regularization parameter.

The discrepancy principle strongly depends on a reliable estimate of the uncertainty level for each signal and time frame and such knowledge is usually not directly available. We have estimated the statistical variance from the temporal and spatial characteristics of the measured signals. However, the systematic errors are unknown, and they can also depend on the profile or the energy spectrum of the radiation. For these reasons, different methods depending solely on the measured data must be considered as well.

A.2.2. Predicted Residual Error Sum of Squares

The method called predicted residual error sum of squares (PRESS) [174] is based on the basic leave-one-out cross-validation. The model minimizing the PRESS score should have the best predictive capability. Over-fitted models tend to fit noisy features in the data, reducing their predictive capability. On the other hand an over-regularized model is not able to follow real features in the measurements, leading to an increase of the PRESS as well. The value of the PRESS score can be expressed by the following formula

$$\mathcal{P}(\lambda) = m^{-1} \sum_{l=1}^{m} \left[\left(\mathbf{T}\mathbf{g}_\lambda^{(l)} \right)_l - b_l \right]^2$$

where $\mathbf{g}_\lambda^{(l)}$ is the solution in which the l-th detector was removed. A simplified solution was found for the decomposition based methods [175]

$$\mathcal{P}(\lambda) = \frac{1}{m} \sum_{k=1}^{m} \left(\frac{\sum_{j=1}^{r} \sum_{l=1}^{m} (1 - f_j) U_{kj} U_{lj} b_l}{\sum_{j=1}^{r} (1 - f_j) U_{kj}^2} \right)^2 \tag{A.12}$$

and the optimum can be found with $\mathcal{O}(mr)$ complexity. The first comparison of the PRESS method and the GCV method, presented by Iwama [170], showed the superiority of the GCV, because if the *hat matrix*

$$\hat{\mathbf{A}}_\lambda \equiv \mathbf{T}(\mathbf{T}^T\mathbf{T} + \lambda\mathbf{H})^{-1}\mathbf{T}^T, \tag{A.13}$$

is close to diagonal, the PRESS method is not able to provide a reliable estimate due to a lack of redundancy in the model. But this is not the case for SXR tomography, where the assumption of smoothness and a large number of overlapping LOSs guarantee sufficient redundancy.

A.2.3. Generalized Cross-validation

The underlying principle in the generalized cross-validation (GCV) is very similar to the PRESS method. GCV was first introduced by Wahba [176] and further developed by Golub [177] for the ridge regression and used for plasma tomography by Iwama [44, 178] later. The GCV score is defined as

$$\mathcal{G}(\lambda) \equiv \frac{\|(\mathbf{I}_m - \hat{\mathbf{A}}_\lambda)\mathbf{b}\|_2^2}{\mathrm{Tr}(\mathbf{I}_m - \hat{\mathbf{A}}_\lambda)^2}.$$

Using a decomposition (A.8) we obtain

$$\mathcal{G}(\lambda) = \frac{\|\mathbf{T}\mathbf{g}_\lambda - \mathbf{b}\|_2^2}{\left(r - \sum_{i=1}^r f_i\right)^2} \tag{A.14}$$

and the residuum in the numerator is evaluated from Eq. (A.11). The existence of a global and unique optimum of the GCV curve is not guaranteed. Consequently, we have observed on real measurements that the proper minimum is not the global one, but, if it was present at all, the local minimum with the highest regularization.

A.2.4. Corrected Akaike Information Criterion

An alternative way of selecting the optimal regularization parameter is a negative entropy minimizing principle called the corrected Akaike information criterion ($\mathrm{AIC_C}$), originally proposed by Hurvich in Ref. [171]. $\mathrm{AIC_C}$ is a modification of the well known AIC [179] method corrected for finite size samples. $\mathrm{AIC_C}$ is defined by the following formula:

$$\mathcal{A}_c(\lambda) = \|\mathbf{T}\mathbf{g}_\lambda - \mathbf{b}\|_2^2 + m(\ln(2\pi) + 1) + \frac{2(p+1)m}{m-p-2}$$

where p denotes the number of parameters. The effective number of parameters of the Tikhonov regularization is determined as [180]

$$p = \mathrm{Tr}(\hat{\mathbf{A}}_\lambda) = \sum f_i.$$

Because $\mathcal{A}_c(\lambda)$ is not a homogeneous function of the residuum, the position of the minimum will depend on the estimated absolute level of the noise. This means that under real experimental conditions a systematic error may be introduced.

A.2.5. Effect of the Nonlinear MFI Iterations

Since the quality of the sQR and the sSVD method is almost the same, all further reconstructions will be performed only by the sSVD method. The convergence and the final solution of the MFI depend also on the choice of the regularization parameter in

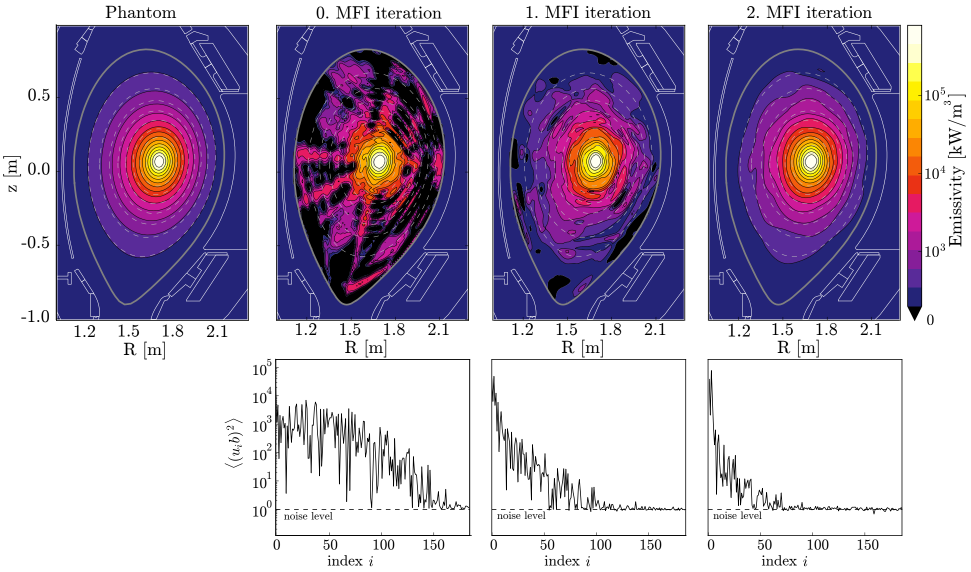

Figure A.2.: A tomographic reconstruction of a peaked radiation profile illustrating the effect of the anisotropic MFI iterations on the reconstruction quality. In the upper row the phantom profile and the reconstruction for 0-th to 2-th MFI iterations in a nonlinear color-scale are shown. In the lower row the corresponding energy spectrum $(\mathbf{U}^T\mathbf{b})_i^2$ is presented.

the intermediate steps. The decomposition $\{\mathbf{U^{(i)}}, \mathbf{D^{(i)}}, \mathbf{V^{(i)}}\}$, obtained in each iteration by the sSVD or the sQR method, is better adapted to describe the solution than the previous one. This is illustrated by the reconstruction of a rather peaked phantom (artificial profile) in Fig. A.2, where the optimal GCV reconstruction is shown in the upper row and the *energy spectrum* of the i-th iteration defined as $(\mathbf{U^{(i)}b})_j^2$ is in the lower row. In the 0-th MFI iteration, equivalent to the 1st order Tikhonov regularization, the energy spectrum is broad, the signal is mixed with the noise and separation of the dimensions dominated by the random variability is possible only for $i > 150$. However, in the first and the second iteration the spectrum is significantly compressed, and the dimensions dominated by the noise can now be clearly separated for $i > 70$.

The effects of the MFI iteration on different regularization selection methods is summarized in Tab. A.1. The first column contains the regularization level for each iteration described by q_λ and the second column is the relative deviation of the tomogram $\mathbf{g}_\lambda$ from the known phantom $\mathbf{g}$:

$$\delta = \|\mathbf{g}_\lambda - \mathbf{g}\|_2 / \|\mathbf{g}\|_2. \tag{A.15}$$

Clearly, the optimal regularization level increases with each iteration, while δ decreases for all methods. At the same time, the optima for the GCV, PRESS, and AIC$_\mathrm{C}$ methods becomes more pronounced and easier to distinguish due to the better signal/noise separation in the energy spectrum (Fig. A.2). The GCV and the PRESS methods provide the best estimates of the regularization level with the final relative deviation δ only higher than the optimum by 1%. The discrepancy principle and the AIC$_\mathrm{C}$ method have both selected slightly over-regularized solutions.

Moreover, we have observed that using all of the methods described above in the intermediate iteration steps leads to a significant increase in the failure rate of the tomography on the experimental signals and the convergence is slowed down. Therefore, we have set the regularization to a fixed value $q_\lambda = 75\%$, which is above the typical regularization level in AUG and the optimal regularization is selected only in the last iteration.

Table A.1.: The performance of different regularization selecting methods on the peaked radiation phantom shown in Fig. A.2 during MFI iterations. Artificial noise of 5% was added to the measurements. The value of the *optimum* regularization was determined as the position of the minimum deviation between reconstruction and the phantom. The regularization level is described by q_λ defined as a quantile of the set $\{D_i^2\}$ being equal to λ.

	0. step		1. step		2. step	
Method	q_λ(%)	δ(%)	q_λ(%)	δ(%)	q_λ(%)	δ(%)
optimum	4	(12)	15	(8)	37	(7)
GCV	13	13	37	10	56	**8**
PRESS	28	21	38	10	52	**8**
DP	22	18	54	14	76	12
AIC$_\mathrm{C}$	12	22	56	14	71	11

A.2.6. Comparison of the Regularization Methods Using Artificial Data

A common way to assess the performance of a tomography method is to reconstruct phantom profiles. We have prepared a set of phantoms with increasing complexity, changing from a simple Gaussian function to a very peaked one, sharply hollow one and finally to a complex hollow-peaked asymmetric profile.The reconstructions were evaluated with a resolution of 100×150 using the anisotropic MFI regularization. The added noise level, based on real discharge noise, was on average equal to 2 % of the signals in each LOS.

The performance of the methods are summarized in Tab. A.2 The differences between the various regularization methods, applying them to all of the artificial profiles, were

Table A.2.: Performance comparison of different regularization methods on various artificial SXR profiles. The score was measured as a relative deviation [%] with respect to the phantom (Eq. (A.15)). The first line corresponds to the *ideal* choice of regularization parameters that minimize the difference to the phantom.

	Gaussian	Peaked	Hollow	Complex
Method	δ (%)			
optimum	(1.3)	(3.6)	(4.6)	(10.7)
GCV	1.4	5.9	**5.2**	**11.2**
PRESS	1.9	**5.8**	5.8	11.6
DP	**1.3**	6.7	8.9	12.8
$\mathrm{AIC_C}$	**1.3**	6.9	7.5	12.7

insignificant, because each regularization was always close to the optimal value. Generally, DP and $\mathrm{AIC_C}$ provide slightly over-smoothed solutions with a higher residuum. The diversity of the methods on the real measurements is substantially larger then on the presented phantoms as will be shown in Sec. A.2.7.

A.2.7. Robustness of the Regularization Methods for Real Datasets

The crucial criterion for the choice of the optimal regularization method is their reliability and robustness for the real measurements. All regularization methods have shown an excellent performance on the artificial profiles; the failure rate was zero, and the estimated regularization had never been far from the optimal value minimizing MSE. However, the real data present additional challenges. We have performed a test on 100 randomly chosen discharges representing together 130 000 time-points. In contrast to the phantom based tests the original emissivity, called also *ground truth*, is unknown. Therefore, our investigation aims to identify the number of clearly over- or under-regularized tomograms, where the regularization method has failed to identify a meaningful solution. The comparison between the regularization methods is presented in Tab. A.3. The most robust is the PRESS method, working in 99.85 % of the analyzed time-points. Since the GCV regularization is less conservative, the regularization level is usually lower and suffers from a higher number of under-regularized time-points. Most of the failures occurred in time-points with a low signal to noise ratio (SNR), while a performance similar to the PRESS method was observed in the hotter plasmas with a better SNR, which are usually considered for the SXR tomographic reconstructions. Finally, the DC and $\mathrm{AIC_C}$ methods provides a comparable level of regularization that is even higher than the estimate from PRESS. The advantage of $\mathrm{AIC_C}$ is higher stability and lower predisposition for extreme values of the regularization parameter than DC. Nevertheless, both these methods are still limited by considerable uncertainty in the estimation of the real level of the noise in the signal.

Table A.3.: The results of the stability test performed with various regularization methods on 130 000 frames corresponding to 100 real plasma discharges. The first two columns contain the fraction of over- and under-regularized frames and the last column is the average difference of the regularization level q_λ with respect to the PRESS method.

Method	over-fitted	over-smoothed	$\langle \Delta q_\lambda \rangle$
GCV	6%	0.1%	-15%
PRESS	**0.1**%	**0.05**%	—%
DC	3%	19%	13%
$\mathrm{AIC_C}$	0.4%	10%	13%

A.3. Conclusion

To access the full potential of this diagnostic, a new reconstruction algorithm was developed that performs a fast tomographic reconstruction with an excellent reconstruction quality. Therefore, multiple methods for the solution of this optimization problem were compared. The fastest reconstructions were obtained by the improved sparse QR method, followed closely by the sparse singular value decomposition (sSVD) method. Both algorithms have linear complexity in the number of pixels of the reconstruction, but the advantage of the sSVD method is the less complicated algorithm, more suitable for further development. The direct inversion, sparse generalized eigenvalues method, and generalized singular value method were substantially slower.

A critical issue of the Tikhonov regularization is the selection of the best regularization parameter. We have compared four methods – PRESS, $\mathrm{AIC_C}$, GCV, and DP, that are the most suitable for our problem. At first, the performance of these methods was investigated using artificial profiles where all methods provided an excellent estimate of the regularization parameter. However, tests on real data revealed significant differences. The most stable and reliable was the method based on the minimization of the predicted residual error sum of squares (PRESS). The stability of the generalized cross-validation (GCV) is comparable to that of PRESS only for discharges with high signal to noise ratio (SNR). Occasionally the GCV minimum was not present, which led to significant over-fitting of the low SNR discharges.

Bibliography

[1] W. Lutz et al. “The end of world population growth”, *Nature* 412, 6846 (2001), pp. 543–545.

[2] E. Commission. *China’s economic and energy situation.* 2012.

[3] OECD. *Uranium 2011:Resources, Production and Demand.* Tech. rep. A Joint Report by the OECD Nuclear Energy Agency and the International Atomic Energy Agency 2012, 2011.

[4] G. W. C. Kaye et al. *Tables of physical and chemical constants: and some mathematical functions.* Longmans, Green and Company, 1921.

[5] V. Shafranov. “Plasma equilibrium in a magnetic field”, *Reviews of Plasma Physics* 2, (1966), p. 103.

[6] F. Wagner. “A quarter-century of H-mode studies”, *Plasma Phys. Controlled Fusion* 49, 12B (2007), B1.

[7] M. Keilhacker et al. “High fusion performance from deuterium-tritium plasmas in JET”, *Nucl. Fusion* 39, 2 (1999), p. 209.

[8] R. Aymar et al. “The ITER design”, *Plasma Phys. Controlled Fusion* 44, 5 (2002), p. 519.

[9] R. Neu et al. “The tungsten experiment in ASDEX Upgrade”, *Journal of nuclear materials* 241, (1997), pp. 678–683.

[10] R. Neu et al. “Ten years of W programme in ASDEX Upgrade—challenges and conclusions”, *Physica Scripta* 2009, T138 (2009), p. 014038.

[11] A. Kallenbach et al. “Optimized tokamak power exhaust with double radiative feedback in ASDEX Upgrade”, *Nucl. Fusion* 52, 12 (2012), p. 122003.

[12] V. Bobkov et al. “First results with 3-strap ICRF antennas in ASDEX Upgrade”, *Nucl. Fusion* 56, 8 (2016), p. 084001.

[13] M. A. Janzer. “Tungsten transport in the plasma edge at ASDEX upgrade.” PhD thesis. lmu, 2015.

[14] A. Mlynek. “Real-time control of the plasma density profile on ASDEX Upgrade.” PhD thesis. LMU, 2010.

[15] R. Fischer et al. “Integrated data analysis of profile diagnostics at ASDEX Upgrade”, *Fusion science and technology* 58, 2 (2010), pp. 675–684.

[16] H. Murmann et al. “The Thomson scattering systems of the ASDEX Upgrade tokamak”, *Rev. Sci. Instrum.* 63, 10 (1992), pp. 4941–4943.

[17] N. Salmon. “First electron temperature edge measurements on the ASDEX Upgrade tokamak using a heterodyne radiometer”, *International journal of infrared and millimeter waves* 15, 1 (1994), pp. 53–60.

[18] S. Denk. Planned to be publish in PPCF.

[19] B. Kurzan et al. “Edge and core Thomson scattering systems and their calibration on the ASDEX Upgrade tokamak”, *Rev. Sci. Instrum.* 82, 10 (2011), p. 103501.

[20] Y. Kim et al. “Neoclassical poloidal and toroidal rotation in tokamaks”, *Physics of Fluids B: Plasma Physics (1989-1993)* 3, 8 (1991), pp. 2050–2060.

[21] E. Viezzer et al. “High-resolution charge exchange measurements at ASDEX Upgrade”, *Rev. Sci. Instrum.* 83, 10 (2012), pp. 103501–103501.

[22] H. Meister et al. “Optimization of a bolometer detector for ITER based on Pt absorber on SiN membrane”, *Rev. Sci. Instrum.* 81, (2010).

[23] L. Ingesson et al. “Tomography diagnostics: Bolometry and soft-X-ray detection”, *Fusion Sci. Technol.* 53, 2 (2008), pp. 528–576.

[24] M. Bernert. “Analysis of the H-mode density limit in the ASDEX Upgrade tokamak using bolometry”, (2013).

[25] J. Fuchs et al. “Twodimensional reconstruction of the radiation power density in ASDEX Upgrade,” *21st EPS Conference on Controlled Fusion and Plasma Physics*. European Physical Society. 1994, pp. 1308–1311.

[26] D. Vezinet. “Soft X-Ray measurements and analysis on Tokamaks in view of real-time control.” PhD thesis. Universite de Provence Aix-Marseille, 2013.

[27] T. Putterich. “Investigations of spectroscopic diagnostic of high-Z elements in fusion plasmas.” PhD thesis. Universitat Augsburg, 2006.

[28] T. Putterich et al. “Calculation and experimental test of the cooling factor of tungsten”, *Nucl. Fusion* 50, 2 (2010), p. 025012.

[29] I. Murakami et al. “Development of quantitative atomic modeling for tungsten transport study using LHD plasma with tungsten pellet injection”, *Nucl. Fusion* 55, 9 (2015), p. 093016.

[30] H. P. Summers. *The ADAS User Manual, version 2.6.* 2004.

[31] T. Putterich et al. “Impurity Limits in a Reactor Grade Fusion Device,” *42nd EPS Conference on Plasma Physics*. European Physical Society. 2015.

[32] T. Odstrcil et al. “Optimized tomography methods for plasma emissivity reconstruction at the ASDEX Upgrade tokamak”, *Rev. Sci. Instrum.* 87, 12 (2016), p. 123505.

[33] V. Igochine et al. *Hotlink based Soft X-ray Diagnostic on ASDEX Upgrade (IPP 1/338)*. Tech. rep. Max-Planck-Institut fur Plasmaphysik, 2010.

[34] B. L. Henke et al. “X-ray interactions: photoabsorption, scattering, transmission, and reflection at E= 50-30,000 eV, Z= 1-92”, *Atomic data and nuclear data tables* 54, 2 (1993), pp. 181–342.

[35] M. Anton et al. “Relative calibration of photodiodes in the soft- X-ray spectral range”, *Rev. Sci. Instrum.* 66, 7 (1995), pp. 3762–3769.

[36] M. Weiland et al. “Investigation of 3D tungsten distributions in (1,1) kink modes induced by toroidal plasma rotation”, *Plasma Phys. Controlled Fusion* 57, 8 (2015), p. 085002.

[37] D. Vezinet et al. “Non-monotonic growth rates of sawtooth precursors evidenced with a new method on ASDEX Upgrade”, *Nucl. Fusion* 56, 8 (2016), p. 086001.

[38] F. Scholze et al. “Mean energy required to produce an electron-hole pair in silicon for photons of energies between 50 and 1500 eV”, *Journal of Applied Physics* 84, 5 (1998), pp. 2926–2939.

[39] D. Vezinet et al. “Absolute spectral characterization of silicon barrier diode: Application to soft X-ray fusion diagnostics at Tore Supra”, *J. appl. Phys.* 114, 2 (2013), p. 023104.

[40] E. Unger. “Untersuchungen zur Absolutkalibration eines Grazing-Incidence-Spektrometers fur Verunreinigungstransport an einem Fusionsexperiment”, *IPP III/187, Max-Planck-Institut fur Plasmaphysik, Garching* (1992).

[41] R. Neu. “Tungsten as a plasma facing material in fusion devices.” PhD thesis. Universitat Tubingen, 2003.

[42] K. Asmussen et al. “Spectroscopic investigations of tungsten in the EUV region and the determination of its concentration in tokamaks”, *Nucl. Fusion* 38, 7 (1998), p. 967.

[43] A. Tikhonov. “Solution of incorrectly formulated problems and the regularization method,” *Soviet Math. Dokl.* Vol. 5. 1963, pp. 1035–1038.

[44] N. Iwama et al. "GCV-aided linear image regularizations in sparse-data computed tomography and their applications to plasma imaging," *Image Processing: Theory and Applications*. Elsevier Amsterdam, 1993, pp. 377–380.

[45] A. Wingen et al. "Regularization of soft-X-ray imaging in the DIII-D tokamak", *Journal of Computational Physics* 289, (2015), pp. 83–95.

[46] M. Anton et al. "X-ray tomography on the TCV tokamak", *Plasma Phys. Controlled Fusion* 38, 11 (1996), p. 1849.

[47] M. Odstrcil et al. "Modern numerical methods for plasma tomography optimisation", *Nucl. Instr. Meth. Phys. Res. A* 686, (2012), pp. 156–161.

[48] L. Ingesson et al. "Soft X ray tomography during ELMs and impurity injection in JET", *Nucl. Fusion* 38, 11 (1998), p. 1675.

[49] E. Lyadina et al. "A space-time tomography algorithm for the five-camera soft X-ray diagnostic at RTP," *EPS, 17C(Part III)*. 1993.

[50] C. Gorner. "Tomographische Untersuchung von globalen Alfven-Eigenmoden am Stellarator Wendelstein 7-AS." PhD thesis. Max-Planck-Institut fur Plasmaphysic, 1998.

[51] R. Korde et al. "The effect of neutron irradiation on silicon photodiodes", *IEEE Trans. Nucl. Sci.* 36, 6 (1989), pp. 2169–2175.

[52] P. McCarthy et al. *The CLISTE interpretive equilibrium code*. Tech. rep. Max-Planck-Institut fur Plasmaphysik, 1999.

[53] J. DeLucia et al. "An iterative metric method for solving the inverse tokamak equilibrium problem", *Journal of Computational Physics* 37, 2 (1980), pp. 183–204.

[54] T. Odstrcil et al. "SXR tomography of tungsten radiation patterns with and without MHD," *42nd EPS Conference on Plasma Physics*. European Physical Society. 2015.

[55] R. Fischer et al. "Coupling of the Flux Diffusion Equation with the Equilibrium Reconstruction at ASDEX Upgrade", *Fusion Sci. Technol.* 69, 2 (2016), pp. 526–536.

[56] R. Fischer et al. "Upgraded equilibrium reconstruction by coupling of an extended set of measurements with current diffusion modelling at ASDEX Upgrade," *43rd EPS Conference on Plasma Physics*. EPS. 2016.

[57] J. Mlynar et al. "Investigation of the consistency of magnetic and soft x-ray plasma position measurements on TCV by means of a rapid tomographic inversion algorithm", *Plasma Phys. Controlled Fusion* 45, 2 (2003), p. 169.

[58] L. Onsager. “Reciprocal relations in irreversible processes. I.”, *Physical review* 37, 4 (1931), p. 405.

[59] R. Dux. “Impurity Transport in Tokamak Plasmas.” Habilitationsschrift. PhD thesis. Universität at Augsburg, 2004.

[60] E. Belli et al. “Kinetic calculation of neoclassical transport including self-consistent electron and impurity dynamics”, *Plasma Phys. Controlled Fusion* 50, 9 (2008), p. 095010.

[61] A. Peeters et al. “The nonlinear gyro-kinetic flux tube code GKW”, *Computer Physics Communications* 180, 12 (2009), pp. 2650–2672.

[62] R. Dux. *STRAHL User Manual.* 2014.

[63] F. L. Hinton. “Collisional transport in plasma”, *Handbook of Plasma Physics* 1, (1983), p. 147.

[64] P. Helander et al. *Collisional transport in magnetized plasmas.* Vol. 4. Cambridge University Press, 2005.

[65] J. D. Huba. *NRL: Plasma formulary.* Tech. rep. DTIC Document, 2009.

[66] S. Hirshman et al. “Neoclassical transport of impurities in tokamak plasmas”, *Nucl. Fusion* 21, 9 (1981), p. 1079.

[67] T. Fulop et al. “Effect of poloidal asymmetry on the impurity density profile in tokamak plasmas”, *Physics of Plasmas* 18, 3 (2011), p. 030703.

[68] C. Angioni et al. “Neoclassical transport of heavy impurities with poloidally asymmetric density distribution in tokamaks”, *Plasma Phys. Controlled Fusion* 56, 12 (2014), p. 124001.

[69] K. W. Wenzel et al. “Neoclassical analysis of impurity transport following transition to improved particle confinement”, *Nucl. Fusion* 30, 6 (1990), p. 1117.

[70] A. Guthrie et al. *The Characteristics of electrical discharge in magnetic fields.* Vol. 5. McGraw-Hill, 1949.

[71] M. L. Reinke. “Experimental tests of parallel impurity transport theory in tokamak plasmas.” PhD thesis. MIT, 2011.

[72] R. Hazeltine et al. “Effects of electrostatic trapping on neoclassical transport in an impure plasma”, *Physics of Fluids (1958-1988)* 19, 8 (1976), pp. 1163–1176.

[73] F. Hinton et al. “Neoclassical ion transport in rotating axisymmetric plasmas”, *Physics of Fluids (1958-1988)* 28, 10 (1985), pp. 3082–3098.

[74] J. Wesson. “Poloidal distribution of impurities in a rotating tokamak plasma”, *Nucl. Fusion* 37, 5 (1997), p. 577.

[75] P. Smeulders. “Tomography of quasi-static deformations of constant-emission surfaces of high-beta plasmas in ASDEX”, *Nucl. Fusion* 26, 3 (1986), p. 267.

[76] S. Hirshman. “Transport of a multiple-ion species plasma in the Pfirsch–Schluter regime”, *Physics of Fluids (1958-1988)* 20, 4 (1977), pp. 589–598.

[77] T. Stringer. “Inclusion of poloidal potential variation in neoclassical transport”, *Physics of Fluids B: Plasma Physics (1989-1993)* 3, 4 (1991), pp. 981–988.

[78] J. Garcia-Regana et al. “Electrostatic potential variation on the flux surface and its impact on impurity transport”, *Nucl. Fusion* 57, 5 (2017), p. 056004.

[79] M. Pedrosa et al. “Electrostatic potential variations along flux surfaces in stellarators”, *Nucl. Fusion* 55, 5 (2015), p. 052001.

[80] S. Klose et al. “Asymmetries of impurity radiation in the W7-AS observed with soft- X-ray tomography”, (2002).

[81] C. Chang et al. “Generation of poloidal electric field in a neutral-beam heated tokamak”, *Nucl. Fusion* 23, 7 (1983), p. 935.

[82] W. Choe et al. “Temperature anisotropy in a cyclotron resonance heated tokamak plasma and the generation of poloidal electric field”, *Physics of Plasmas (1994-present)* 2, 6 (1995), pp. 2044–2054.

[83] L. Ingesson et al. “Comparison of basis functions in soft X-ray tomography and observation of poloidal asymmetries in impurity density”, *Plasma Phys. Controlled Fusion* 42, 2 (2000), p. 161.

[84] M. Reinke et al. “Poloidal variation of high-Z impurity density due to hydrogen minority ion cyclotron resonance heating on Alcator C-Mod”, *Plasma Phys. Controlled Fusion* 54, 4 (2012), p. 045004.

[85] M. Weiland. “Influence of RF heating and MHD instabilities on the fast-ion distribution in ASDEX Upgrade.” PhD thesis. LMU, 2016.

[86] M. Porkolab. “Plasma heating by fast magnetosonic waves in tokamaks,” *AIP Conference Proceedings*. IOP INSTITUTE OF PHYSICS PUBLISHING LTD. 1994, pp. 99–99.

[87] M. Mantsinen et al. “Third harmonic ICRF heating of deuterium beam ions on ASDEX Upgrade,” *Proceedings of the 43rd EPS Conference on Plasma Physics*. European Physical Society (EPS). 2016.

[88] Y. O. Kazakov et al. “On resonant ICRF absorption in three-ion component plasmas: a new promising tool for fast ion generation”, *Nucl. Fusion* 55, 3 (2015), p. 032001.

[89] Y. O. Kazakov et al. “A new ion cyclotron range of frequency scenario for bulk ion heating in deuterium-tritium plasmas: How to utilize intrinsic impurities in our favour”, *Physics of Plasmas* 22, 8 (2015), p. 082511.

[90] R. Bilato et al. “Modelling the influence of temperature anisotropies on poloidal asymmetries of density in the core of rotating plasmas”, *Nucl. Fusion* 54, 7 (2014), p. 072003.

[91] R. Dendy et al. “A model for ideal m= 1 internal kink stabilization by minority ion cyclotron resonant heating”, *Physics of Plasmas (1994-present)* 2, 5 (1995), pp. 1623–1636.

[92] J. Graves et al. “Modelling ICCD Experiments for Sawtooth Control in JET,” *Theory of Fusion Plasmas.* CRPP-CONF-2006-093. 2006.

[93] R. Bilato et al. “The impact of the ion-cyclotron-resonance location on the poloidal asymmetries of impurity density in an ICRF-heated rotating plasma”, *Nucl. Fusion* 57, 5 (2017), p. 056020.

[94] G. W. Hammett. “Fast ion studies of ion cyclotron heating in the PLT tokamak.” PhD thesis. Princeton University, 1986.

[95] *TRANSP REFERENCES.* http://w3.pppl.gov/transp/refs. 1998.

[96] R. Bilato et al. “Simulations of combined neutral beam injection and ion cyclotron heating with the TORIC-SSFPQL package”, *Nucl. Fusion* 51, 10 (2011), p. 103034.

[97] W. Core. “A note on the calculation of NBI fast ion distribution functions”, *Nucl. Fusion* 33, 5 (1993), p. 829.

[98] A. Pankin et al. “The tokamak Monte Carlo fast ion module NUBEAM in the National Transport Code Collaboration library”, *Computer Physics Communications* 159, 3 (2004), pp. 157–184.

[99] E. Westerhof et al. *RELAX: A Computer Code for the Study of Collisional and Wave Driven Relaxation of the Electron Distribution Function in Toroidal Geometry.* Rijnhuizen report. FOM-Instituut voor Plasmafysica, 1992.

[100] S. K. Wong. “Transport of impure plasma with arbitrary toroidal rotation”, *Physics of Fluids (1958-1988)* 30, 3 (1987), pp. 818–829.

[101] C. Chang. “Enhancement of neoclassical transport coefficients by a poloidal electric field in tokamaks”, *The Physics of fluids* 26, 8 (1983), pp. 2140–2149.

[102] K. Indireshkumar et al. “Effect of a poloidal electric field on neoclassical transport in a multispecies tokamak plasma”, *Physics of Fluids B: Plasma Physics* 5, 6 (1993), pp. 1850–1868.

[103] T. Fulop et al. “Nonlinear neoclassical transport in a rotating impure plasma with large gradients”, *Physics of Plasmas (1994-present)* 6, 8 (1999), pp. 3066–3075.

[104] M. Romanelli et al. “Effects of density asymmetries on heavy impurity transport in a rotating tokamak plasma”, *Plasma Phys. Controlled Fusion* 40, 10 (1998), p. 1767.

[105] M. Romanelli et al. “Enhancement of the Conventional Pfirsch-Schlueter Flux of Heavy Ions in a Rotating Plasma due to the Poloidal Asymmetry of the Particle Density”, *25th EPS Conf. on Contr. Fusion and Plasma Physics, Praha,* (1998), pp. 1955–1958.

[106] E. Belli et al. “Pfirsch– Schluter neoclassical heavy impurity transport in a rotating plasma”, *Plasma Phys. Controlled Fusion* 56, 12 (2014), p. 124002.

[107] A. Bergmann. “Effect of islands and rotation on neoclassical tungsten impurity transport,” *43rd EPS Conference on Plasma Physics*. 2016.

[108] F. J. Casson et al. “Gyrokinetic simulations including the centrifugal force in a rotating tokamak plasma”, *Physics of Plasmas (1994-present)* 17, 10 (2010), p. 102305.

[109] M. R. Fahey et al. “GYRO: A 5-d gyrokinetic-maxwell solver,” *Proceedings of the 2004 ACM/IEEE conference on Supercomputing*. IEEE Computer Society. 2004, p. 26.

[110] C. Angioni et al. “Analytic formulae for centrifugal effects on turbulent transport of trace impurities in tokamak plasmas”, *Physics of Plasmas (1994-present)* 19, 12 (2012), p. 122311.

[111] S. Moradi et al. “A possible mechanism responsible for generating impurity outward flow under radio frequency heating”, *Plasma Phys. Controlled Fusion* 53, 11 (2011), p. 115008.

[112] A. Mollen et al. “Effect of poloidal asymmetries on impurity peaking in tokamaks”, *Physics of plasmas* 19, 5 (2012).

[113] A. Mollen et al. “Impurity transport in Alcator C-Mod in the presence of poloidal density variation induced by ion cyclotron resonance heating”, *Plasma Phys. Controlled Fusion* 56, 12 (2014), p. 124005.

[114] F. Casson et al. “Theoretical description of heavy impurity transport and its application to the modelling of tungsten in JET and ASDEX upgrade”, *Plasma Phys. Controlled Fusion* 57, 1 (2015), p. 014031.

[115] C. Angioni et al. “Tungsten transport in JET H-mode plasmas in hybrid scenario, experimental observations and modelling”, *Nucl. Fusion* 54, 8 (2014), p. 083028.

[116] C. Angioni et al. “The impact of poloidal asymmetries on tungsten transport in the core of JET H-mode plasmas”, *Physics of Plasmas* 22, 5 (2015), p. 055902.

[117] R. Dux et al. “Z dependence of the core impurity transport in ASDEX Upgrade H-mode discharges”, *Nucl. Fusion* 39, 11 (1999), p. 1509.

[118] H. Chen et al. “Poloidally asymmetric distribution of impurities in Joint European Torus plasmas”, *Physics of Plasmas (1994-present)* 7, 11 (2000), pp. 4567–4572.

[119] R. Gianella et al. “Poloidal asymmetry of impurity in co-and counter-injection experiment at JET,” *Europhysics Conference Abstracts.* Vol. 16. Part I. 1992, pp. I–279.

[120] B. Alper et al. “Strong asymmetries in impurity distributions of JET plasmas,” *Europhysics Conference Abstracts (Proc. of the 23rd EPS Conference on Controlled Fusion and Plasma Physics, Kiev, 1996), edited by D. Gresillon, A. Sitenko, and A. Zagorodny.* Vol. 20. part I. 1996, pp. 163–166.

[121] M. Reinke et al. “Parallel transport studies of high-Z impurities in the core of Alcator C-Mod plasmas”, (2013).

[122] I. EDA et al. “Overview and summary”, *Nucl. Fusion* 39, 12 ITER physics basis (1999), pp. 2137–2174.

[123] M. Weiland et al. “Enhancement of the FIDA diagnostic at ASDEX Upgrade for velocity space tomography”, *Plasma Phys. Controlled Fusion* 58, 2 (2016), p. 025012.

[124] G. Tardini et al. “First neutron spectrometry measurements in the ASDEX Upgrade tokamak”, *Journal of Instrumentation* 7, 03 (2012), p. C03004.

[125] L. Giannone et al. “Real-time diamagnetic flux measurements on ASDEX Upgrade”, *Rev. Sci. Instrum.* 87, 5 (2016), p. 053509.

[126] R. McDermott et al. “Core momentum and particle transport studies in the ASDEX Upgrade tokamak”, *Plasma Physics and Controlled Fusion* 53, 12 (2011), p. 124013.

[127] M. Brambilla et al. “Advances in numerical simulations of ion cyclotron heating of non-Maxwellian plasmas”, *Nucl. Fusion* 49, 8 (2009), p. 085004.

[128] M. Brambilla. “Quasi-linear ion distribution function during ion cyclotron heating in tokamaks”, *Nucl. Fusion* 34, 8 (1994), pp. 1121–43.

[129] T. Odstrcil et al. “Investigation the fast particle velocity space by poloidal asymmetries of heavy ions,” *43nd EPS Conference on Plasma Physics*. European Physical Society. 2016.

[130] H. Sandven. “Evaluation of Distribution Function Models for ICRH-induced Impurity Transport in Tokamaks.” MA thesis. EXAMENSARBETE ELECTRICAL ENGINEERING, 2016.

[131] Y. O. Kazakov et al. “Poloidal asymmetries due to ion cyclotron resonance heating”, *Plasma Phys. Controlled Fusion* 54, 10 (2012), p. 105010.

[132] R. Goldston et al. “New techniques for calculating heat and particle source rates due to neutral beam injection in axisymmetric tokamaks”, *Journal of computational physics* 43, 1 (1981), pp. 61–78.

[133] T. Nakano et al. “Tungsten accumulation in H-mode plasmas of JT-60U”, *Nucl. Fusion* 49, 11 (2009), p. 115024.

[134] T. Nakano et al. “Tungsten transport and accumulation in JT-60U”, *Journal of Nuclear Materials* 415, 1 (2011), S327–S333.

[135] K. Hoshino et al. “Accumulation Process of High-Z Impurity in Toroidal Rotating Tokamak Plasma”, *Contributions to Plasma Physics* 50, 3-5 (2010), pp. 386–391.

[136] K. McClements et al. “The orbital dynamics and collisional transport of trace massive impurity ions in rotating tokamaks”, *Plasma Phys. Controlled Fusion* 51, 11 (2009), p. 115009.

[137] K. Wong et al. “xxx,” *Proceedings of the 14rd EPS Conference on Plasma Physics*. European Physical Society (EPS). 1987, p. 121.

[138] K. Wong et al. “Orbit effects on impurity transport in a rotating tokamak plasma”, *Physics of Fluids B: Plasma Physics* 1, 3 (1989), pp. 545–554.

[139] C. Angioni et al. “A comparison of the impact of central ECRH and central ICRH on the tungsten behaviour in ASDEX Upgrade H-mode plasmas”, *Nucl. Fusion* (2017). accepted.

[140] R. Dux et al. “Plasma-wall interaction and plasma behaviour in the non-boronised all tungsten ASDEX Upgrade”, *Journal of Nuclear Materials* 390, (2009), pp. 858–863.

[141] T. Odstrcil. “Development and analysis of a database of rotation of ASDEX Upgrade H-modes.” MA thesis. University of Stuttgart, 2013.

[142] M. Sertoli et al. “Local effects of ECRH on argon transport in L-mode discharges at ASDEX Upgrade”, *Plasma Phys. Controlled Fusion* 53, 3 (2011), p. 035024.

[143] R. Dux. “Impurity transport in ASDEX Upgrade”, *Fusion Sci. Technol.* 44, 3 (2003), pp. 708–715.

[144] D. Escande et al. “Calculation of transport coefficient profiles in modulation experiments as an inverse problem”, *Phys. Rev. Lett.* 108, 12 (2012), p. 125007.

[145] N. T. Howard. “Experimental and gyrokinetic studies of impurity transport in the core of Alcator C-Mod plasmas.” PhD thesis. MIT, 2012.

[146] D. Wagner. “Electron and Impurity Transport Studies in the TCV Tokamak.” PhD thesis. EPFL, 2013.

[147] R. Dux et al. “Influence of the heating profile on impurity transport in ASDEX Upgrade”, *Plasma Phys. Controlled Fusion* 45, 9 (2003), p. 1815.

[148] E. Viezzer et al. “Collisionality dependence of edge rotation and in–out impurity asymmetries in ASDEX Upgrade H-mode plasmas”, *Nucl. Fusion* 55, 12 (2015), p. 123002.

[149] J. Hedin et al. “Parasitic absorption by fusion born-particles in ICRF heated plasmas”, *Plasma Phys. Controlled Fusion* 40, 6 (1998), p. 1085.

[150] M. Reinke et al. “Two dimensional radiated power diagnostics on Alcator C-Mod)”, *Rev. Sci. Instrum.* 79, 10 (2008), 10F306.

[151] A. Gude et al. “Hollow central radiation profiles and inverse sawtooth-like crashes in ASDEX Upgrade plasmas with central wave heating,” *Europhysics Conf. Abstracts CD-ROM, Proc. of the 37th EPS Conf. on Plasma Physics.* 2010.

[152] M. Sertoli et al. “Interplay between central ECRH and saturated (m, n)=(1, 1) MHD activity in mitigating tungsten accumulation at ASDEX Upgrade”, *Nucl. Fusion* 55, 11 (2015), p. 113029.

[153] M. Sertoli et al. “Characterization of saturated MHD instabilities through 2D electron temperature profile reconstruction from 1D ECE measurements”, *Nucl. Fusion* 53, 5 (2013), p. 053015.

[154] G. Fehmers et al. “An algorithm for quadratic optimization with one quadratic constraint and bounds on the variables”, *Inverse problems* 14, 4 (1998), p. 893.

[155] L. Ingesson. *The Mathematics of some Tomography Algorithms used at JET*. Tech. rep. Commission of the European Communities, Abingdon (United Kingdom). JET Joint Undertaking, 2000.

[156] N. Terasaki et al. “Linear algebraic algorithms for high speed and stable reconstruction of plasma image”, *Fusion Eng. Des.* 34, (1997), pp. 801–804.

[157] J. Bielecki et al. “Phillips- Tikhonov regularization with a priori information for neutron emission tomographic reconstruction on Joint European Torus”, *Rev. Sci. Instrum.* 86, 9 (2015), p. 093505.

[158] P. Hansen. “Regularization tools: A Matlab package for analysis and solution of discrete ill-posed problems”, *NUMER ALGORITHMS* 6, 1 (1994), pp. 1–35.

[159] D. Mazon et al. “Soft X-ray imaging techniques on Tore Supra: Present status and possible future developments”, *Nuclear Instruments and Methods in Physics Research Section A: Accelerators, Spectrometers, Detectors and Associated Equipment* 720, (2013), pp. 78–82.

[160] R. Lehoucq et al. *ARPACK users’ guide: solution of large-scale eigenvalue problems with implicitly restarted Arnoldi methods*. Vol. 6. Siam, 1998.

[161] C. Van Loan. “Computing the CS and the generalized singular value decompositions”, *Numerische Mathematik* 46, 4 (1985), pp. 479–491.

[162] P. Hansen. “Numerical tools for analysis and solution of Fredholm integral equations of the first kind”, *Inverse problems* 8, 6 (1992), p. 849.

[163] Y. Chen et al. “Algorithm 887: CHOLMOD, supernodal sparse Cholesky factorization and update/downdate”, *ACM Transactions on Mathematical Software (TOMS)* 35, 3 (2008), p. 22.

[164] G. H. Golub et al. *Matrix computations*. Vol. 3. JHU Press, 2012.

[165] Y. Hosoda et al. “A direct method for ill-posed linear operator equations: truncated least-square least-norm solutions”, *Jpn. J. appl. Math.* 4, (1994), pp. 287–298.

[166] D. Mazon et al. “Soft x-ray tomography for real-time applications: present status at Tore Supra and possible future developments”, *Rev. Sci. Instrum.* 83, 6 (2012), p. 063505.

[167] V. Loffelmann et al. “Minimum Fisher Tikhonov Regularization Adapted to Real-Time Tomography”, *Fusion Sci. Technol.* 69, 2 (2016).

[168] M. Bertero et al. “Linear inverse problems with discrete data: II. Stability and regularisation”, *Inverse problems* 4, 3 (1988), p. 573.

[169] P. Hansen. “Analysis of discrete ill-posed problems by means of the L-curve”, *SIAM review* 34, 4 (1992), pp. 561–580.

[170] N. Iwama et al. “Phillips–Tikhonov regularization of plasma image reconstruction with the generalized cross validation”, *Applied Physics Letters* 54, 6 (1989), pp. 502–504.

[171] C. Hurvich et al. “Regression and time series model selection in small samples”, *Biometrika* 76, 2 (1989), pp. 297–307.

[172] T. Kitagawa. “A deterministic approach to optimal regularization—The finite dimensional case—”, *Jpn. J. Appl. Math.* 4, 3 (1987), pp. 371–391.

[173] A. Tikhonov et al. “Use of the regularization method in non-linear problems”, *USSR Comput. Math. & Math. Phys.* 5, 3 (1965), pp. 93–107.

[174] D. Girard. “Optimal regularized reconstruction in computerized tomography”, *SIAM J SCI STAT COMP.* 8, 6 (1987), pp. 934–950.

[175] N. Iwama. “Numerical optimizations of plasma image reconstructions with sparse-data computer tomography”, *IAEA Technical Committee Meeting* (1990).

[176] G. Wahba. “Practical approximate solutions to linear operator equations when the data are noisy”, *SIAM Journal on Numerical Analysis* 14, 4 (1977), pp. 651–667.

[177] G. Golub et al. “Generalized cross-validation as a method for choosing a good ridge parameter”, *Technometrics* 21, 2 (1979), pp. 215–223.

[178] N. Iwama et al. “Image Reconstruction by Double Use of QR Decomposition with Minimum GCV Criterion for Sparse-Data Computed Tomography”, *A bulletin of Daido Technical College* 42, (2006), pp. 93–101.

[179] H. Akaike. “A new look at the statistical model identification”, *Automatic Control, IEEE Transactions on* 19, 6 (1974), pp. 716–723.

[180] C. Hurvich et al. “Smoothing parameter selection in nonparametric regression using an improved Akaike information criterion”, *Journal of the Royal Statistical Society: Series B (Statistical Methodology)* 60, 2 (1998), pp. 271–293.

Acknowledgments

I am grateful to my academic supervisor Prof. U. Ströth for the providing me the opportunity to perform my Ph.D. on the ASDEX Upgrade tokamak in Garching.

I thank sincerely to Dr. T. Pütterich for the sharing of his wisdom and knowledge about the tungsten with me. Moreover, I greatly appreciate the help with the careful planning and programing of the discharges, it is a pity that only so few of them was at the end relevant for the thesis. Finally, I am very grateful for a patient correction of my manuscript.

I am particularly obligated to Dr. C. Angioni for the fruitful discussions about the impurity transport, and introduction to the NEO code. Moreover, I would like to express my sincere gratitude to Dr. Roberto Bilato for a many beneficial discussions about the ion cyclotron heating and the fast ions.

I am indebted to Dr. B. Geiger for his amazing discharges, because without them would be finishing of this thesis impossible.

All my lunch mates and friends from IPP and the most to Severin, for the interesting discussions about the most unbelievably ridiculous topic.

I would like to express my sincere thanks to my brother Michal for the careful proofreading of the manuscript, and for a many long discussions about the plasma tomography.

For the excellent running of the ASDEX tokamak I acknowledge the ASDEX Upgrade team, for the great effort and assistance in each of mine experimental session.

I would like to thank to my fiancée Lucie. I have not idea how would I survive the writing of this thesis without her encouragement. Her smile fills my heart with happiness.

A particular regard goes to my parent for their patience and support during this long stay abroad.